

March 2018

Three Dimensional Direct Print Additively Manufactured High-Q Microwave Filters and Embedded Antennas

Derar Fayez Hawatmeh

University of South Florida, derar@mail.usf.edu

Follow this and additional works at: <http://scholarcommons.usf.edu/etd>

 Part of the [Electromagnetics and Photonics Commons](#)

Scholar Commons Citation

Hawatmeh, Derar Fayez, "Three Dimensional Direct Print Additively Manufactured High-Q Microwave Filters and Embedded Antennas" (2018). *Graduate Theses and Dissertations*.

<http://scholarcommons.usf.edu/etd/7165>

This Dissertation is brought to you for free and open access by the Graduate School at Scholar Commons. It has been accepted for inclusion in Graduate Theses and Dissertations by an authorized administrator of Scholar Commons. For more information, please contact scholarcommons@usf.edu.

Three Dimensional Direct Print Additively Manufactured High-Q Microwave Filters and
Embedded Antennas

by

Derar Fayeze Hawatmeh

A dissertation submitted in partial fulfillment
of the requirements for the degree of
Doctor of Philosophy in Electrical Engineering
Department of Electrical Engineering
College of Engineering
University of South Florida

Major Professor: Thomas Weller, Ph.D.
Kenneth Church, Ph.D.
Nathan Crane, Ph.D.
Gokhan Mumcu, Ph.D.
Jing Wang, Ph.D.

Date of Approval:
March 21, 2018

Keywords: 3D-printing, Dipole, Picosecond laser machining, Quality factor, Array, Non-planar,
Capacitively-loaded cavity, Evanescent-mode, Stacked structure, Vertically coupled

Copyright © 2018, Derar Fayeze Hawatmeh

DEDICATION

To my father, Fayez, and my mother, Khawla, for being perfect role models and being my first teachers, for their constant support, encouragement, and prayers of day and night. Without their inspiration, drive, trust, and support, I might not be the person I am today. To my beloved wife, Farah, for her endless love, support, understanding, inspiration, and taking care of our family during my PhD journey. I'll be always thankful and grateful to have such a faithful wife next to me and sharing my moments of success. To my daughter and son, Omaira and Hamza, for always making me smile and lighthearted after each long working day. To my amazing siblings, Belal, Hala, Heba, and Ammar for their huge amount of love and support. They all are the secret behind my success.

ACKNOWLEDGMENTS

No word can express my gratitude and appreciation to have Professor Thomas Weller as my PhD advisor. He has always amazed me with his high degree of professionalism, expertise, humbleness, management skills, patience, molarity, and great kindness. Dr. Weller's endless guidance and his generous ocean of microwave and RF knowledge will be always highly appreciated. His unique character will always continue to be a role model for me.

I'm sincerely thankful to my committee members, Dr. Kenneth Church, Dr. Nathan Crane, Dr. Gokhan Mumcu, and Dr. Jing Wang for reviewing my dissertation, for the candidacy presentation feedback, and the dissertation defense. I also would like to thank Dr. Venkat Bhethanabotla for accepting my invitation to chair my dissertation defense. Their time and valuable efforts are appreciated. I am also grateful to the University of South Florida administration, faculty and staff of the college of engineering, the electrical engineering department, the nanotechnology research and education center, and the WAMI center for providing international student employment opportunities, and offering the facilities and the environment for research and studying.

Special thanks to my uncle, Dr. Kadry Allaboun, who serves as a neurologist in NC, for his unmeasurable support and continuous calls through my PhD mission. As well, big thanks to his wife, Dr. Nadia for her amazing support and the delicious food she prepared during our existence in NC. Also, I sincerely thank my father-in-law, Dr. Mohammad and mother-in-law, Heyam for their support, trust, encouragements, and prayers. I would also like to thank WAMI

group members and 412 colleagues includes: Ahmad Gheethan, Eduardo Rojas, Maria Erazo, , Abdullah Qaroot, Ramiro Ramirez, Ibrahim Nassar, Mohamed Abdin, Arya Menon, Michael Grady, Abhishek Dey, Denise Lugo, Anthony Ross, Enrique Gonzalez, Seth York, Charles Curtiss, Patrick Nesbitt, Di Lan, Ismail Uluer, Omer Firat, Xu Han, and Jon Obrien. Also, I would like to thank Dr. Paul Deffenbaugh for his support in using the 3D printer and the laser. Thanks to all my Jordan University of Science and Technology (JUST) friends, especially who moved to the US and kept in contact. I would like to specify the master's degree colleagues Majdi Ababneh and Faeik Alrabee, who joined the EE department at USF to pursue their PhD program too.

Thanks to Arya Menon for proof-reading my dissertation. Arya's valuable time and efforts are highly appreciated. Also, thanks to E. Rojas for sharing his additive manufacturing knowledge, for the training on the 3D printing machine, and for his effort in accomplishing the laser article. Thanks to A. Gheetan for his nice reception and help to settle down when we came to Tampa in 2014. Gheetan continues to help and will be always appreciated. Thanks to Qorvo, for offering me two summer internships, which provided me a decent amount of RF knowledge and design experience. Qorvo is a leading semiconductor company that added unique values to my resume.

Thanks to everyone who taught me, regardless the amount of knowledge, since I was a kid until now. I would like to specify our beloved Professor Nihad Dib, who I chose to end with, as he was the reason of my current path. Dr. Nihad was my undergrad supervisor, and my master's thesis advisor at JUST. Whatever I say will be too little to describe his endless efforts, unmeasurable support, and faithfulness. Such professor will be always a role model for me.

Most importantly, I'm thankful to Allah for his blessing that helped me in my achievements.

TABLE OF CONTENTS

LIST OF TABLES	iii
LIST OF FIGURES	iv
ABSTRACT.....	viii
CHAPTER 1: INTRODUCTION.....	1
1.1 Motivation.....	1
1.2 Contributions.....	4
1.3 Dissertation Organization	5
CHAPTER 2: LITERATURE REVIEW AND BACKGROUND	7
2.1 Introduction.....	7
2.2 Non-Planar Antenna and Antenna Array	7
2.3 Capacitively-loaded Cavity Resonator and Filter	11
CHAPTER 3: EMBEDDED 3D-PRINTED AND CONFORMAL HALF-WAVE DIPOLE ANTENNA, AND ANTENNA ARRAY	14
3.1 Introduction.....	14
3.2 Embedded 6 GHz 3D-Printed Half-Wave Dipole Antenna.....	14
3.2.1 Antenna Design.....	14
3.2.2 Experimental Results	17
3.2.3 Analysis of Surface Roughness Effects	20
3.3 A Multi-Material 3D Printing Approach for Conformal Microwave Antennas	24
3.3.1 Design Digest.....	24
3.3.2 Fabrication Approach.....	24
3.3.3 Design Example	26
3.4 Embedded 6 GHz 3D-Printed Half-Wave Dipole Antenna Array.....	29
3.4.1 Contribution	29
3.4.2 Array Design, Fabrication and Performance	31
3.5 Conclusion	34
CHAPTER 4: HIGH-Q EVANESCENT-MODE CAVITY RESONATOR AND FILTER	35
4.1 Introduction.....	35
4.2 High-Q Capacitively-Loaded Evanescent-Mode Cavity Resonator	35
4.2.1 Direct Print Additively Manufactured S/C-Band High-Q Resonator	36

4.2.2 Enhanced Performance Capacitively-loaded Cavity Resonator	42
4.3 Direct Print Additively Manufactured Capacitively-Loaded Band-Pass Filter	50
4.3.1 Introduction.....	50
4.3.2 Synthesis of Coupled Resonator Filter	51
4.3.3 Direct Print Additively Manufactured Laterally-Coupled Band-Pass Filter	54
4.3.4 Direct Print Additively Manufactured Vertically-Coupled Band-Pass Filter	59
4.4 Conclusion	65
 CHAPTER 5: SUMMARY AND RECOMMENDATIONS FOR FUTURE WORK.....	66
5.1 Summary	66
5.2 Recommendation for Future Work	69
5.3 Perspective on Additive Manufacturing	70
 REFERENCES	72
 APPENDICES	81
Appendix A: Copyright Permissions	82
A.1 Permissions for Chapter 3	82
A.2 Permissions for Chapter 4	85
Appendix B: nScript Tabletop 3Dn Printer.....	87
 ABOUT THE AUTHOR	End Page

LIST OF TABLES

Table 3.1	Dimensions of the 3D antenna in mm.	16
Table 4.1	Cavity conductive parts and conductive materials vs. the unloaded quality factor at 2.3 GHz.	49

LIST OF FIGURES

Figure 1.1	3D printer technologies.....	2
Figure 2.1	Non-planar antenna designs using several fabrication technique.....	8
Figure 2.2	Non-planar antenna array designs.....	10
Figure 2.3	Evanescent mode capacitively-loaded resonator and filter.....	12
Figure 2.4	Additively manufactured high-Q resonators and filters.....	13
Figure 2.5	Antenna feed system built using selective laser melting fabrication process.....	13
Figure 3.1	3D 6 GHz antenna design	16
Figure 3.2	The embedded 3D antenna (a) and planar version (b).....	16
Figure 3.3	S_{11} of the 3D antenna	18
Figure 3.4	6 GHz antenna patterns.....	19
Figure 3.5	S_{11} of the planar antenna.....	19
Figure 3.6	Surrounding environment changes effect	19
Figure 3.7	Smooth and corrugated $\lambda/4$ transformers	21
Figure 3.8	Simulated propagation constant (β) of the corrugated $\lambda/4$ transformer normalized to β_s for the smooth substrates.....	22
Figure 3.9	Simulated attenuation constant (α) of corrugated and smooth transmission lines for various corrugation profiles (r_c)	23
Figure 3.10	Fused deposition modeling process (a) printing of thin ABS substrate (b) Flexible ABS substrate (150 microns thick)	25
Figure 3.11	Steps involved in the fabrication process.....	26

Figure 3.12	3D 6 GHz antenna design	27
Figure 3.13	Dipole and feed network on the flexible ABS substrate.....	27
Figure 3.14	Profilometer scan	28
Figure 3.15	Measured and simulated S_{11}	28
Figure 3.16	Measured and simulated normalized radiation pattern (10 dB/division).....	29
Figure 3.17	Manufactured 6.0 GHz antenna with superstrate removed to show the conformal circuitry	29
Figure 3.18	Array structure (a) Total structure (b) Feeding network.....	30
Figure 3.19	Simulated S_{11} for different rotation angles	32
Figure 3.20	Array realized gain.....	33
Figure 3.21	Fabricated array	33
Figure 3.22	Simulated and measured S_{11}	34
Figure 3.23	Simulated and measured realized gain ($\phi=0^\circ$)	34
Figure 4.1	Evanescent-mode cavity resonator	37
Figure 4.2	Evanescent-mode resonator structure	38
Figure 4.3	Evanescent-mode cavity resonator fabrication process	39
Figure 4.4	Single resonator simulated vs. measured S_{21}	40
Figure 4.5	Device under test.....	41
Figure 4.6	Measured S_{21} for different gap settings	41
Figure 4.7	Gap changes vs. resonance frequency and corresponding unloaded quality factor	41
Figure 4.8	Side-view of the capacitively-loaded cavity resonator	42
Figure 4.9	3D view of the single capacitively-loaded cavity resonator	43
Figure 4.10	Enhanced resonator measured S_{21} for different gap settings (LCP gap material).....	44

Figure 4.11	Gap variation vs. resonance frequency and corresponding unloaded quality factor (LCP gap material)	45
Figure 4.12	Single resonator with Parylene coated post	46
Figure 4.13	Enhanced resonator measured S_{21} for different gap settings (Parylene gap material)	46
Figure 4.14	Fabricated capacitively-loaded cavity resonator.....	47
Figure 4.15	Single resonator under test.....	47
Figure 4.16	Gap variation vs. resonance frequency and corresponding unloaded quality factor (Parylene gap material).....	48
Figure 4.17	Unloaded quality factor of the single capacitively-loaded cavity resonator for different gap material, and different gap settings.....	49
Figure 4.18	The effect of changing the cavity height relative to the baseline design parameter (4.5 mm) at gap size of 60 μm	50
Figure 4.19	Equivalent circuit of n-coupled resonators	51
Figure 4.20	S_{21} of two coupled resonators	54
Figure 4.21	Laterally coupled evanescent-mode cavity filter (all dimensions are in mm)	55
Figure 4.22	Post-to-post spacing (px) and opening (y) vs. internal coupling (k)	56
Figure 4.23	Fabrication and assembly steps of the laterally coupled filter	57
Figure 4.24	Measured S-parameters of the laterally coupled filter	58
Figure 4.25	S-parameters of the 2% (red line), and 2.4% (black line) filter.....	59
Figure 4.26	Vertically-stacked capacitively-loaded cavity filter (all dimensions are in mm)	61
Figure 4.27	Coupling opening (r) vs. coupling coefficient (k)	61
Figure 4.28	Fabrication and assembly steps of the vertically-stacked filter	62
Figure 4.29	Fabricated vertically-stacked filter	62
Figure 4.30	Vertically-stacked capacitively-loaded cavity filter	63

Figure 4.31	Simulated and measured S-parameters of the vertically stacked filter	63
Figure 4.32	Multi-layer structure and Feedlines orientation	64
Figure 4.33	Filter simulated S-parameters for different rotation angles	65
Figure B.1	nScript Tabletop 3Dn printer	87
Figure B.2	FDM and micro-dispenser heads	87

ABSTRACT

The need for miniaturized, and high performance microwave devices has focused significant attention onto new fabrication technologies that can simultaneously achieve high performance and low manufacturing complexity. Additive manufacturing (AM) has proven its capability in fabricating high performance, compact and light weight microwave circuits and antennas, as well as the ability to achieve designs that are complicated to fabricate using other manufacturing approaches. Direct print additive manufacturing (DPAM) is an emerging AM process that combines the fused deposition modeling (FDM) of thermoplastics with micro-dispensing of conductive and insulating pastes. DPAM has the potential to jointly combine high performance and low manufacturing complexity, along with the possibility of real-time tuning.

This dissertation aims to leverage the powerful capabilities of DPAM to come-up with new designs and solutions that meet the requirements of rapidly evolving wireless systems and applications. Furthermore, the work in this dissertation provides new techniques and approaches to alleviate the drawbacks and limitations of DPAM fabrication technology. Firstly, the development of 3D packaged antenna, and antenna array are presented along with an analysis of the inherent roughness of 3D printed structures to provide a deeper understanding of the antenna RF performance. The single element presents a new volumetric approach to realizing a 3D half-wave dipole in a packaged format, where it provides the ability to keep a signal distribution network in close proximity to the ground plane, facilitating the implementation of ground connections (e.g. for an active device), mitigating potential surface wave losses, as well as

achieving a modest (10.6%) length reduction. In addition, a new approach of implementing conformal antennas using DPAM is presented by printing thin and flexible substrate that can be adhered to 3D structures to facilitate the fabrication and reduce the surface roughness. The array design leverages direct digital manufacturing (DDM) technology to realize a shaped substrate structure that is used to control the array beamwidth. The non-planar substrate allows the element spacing to be changed without affecting the length of the feed network or the distance to the underlying ground plane.

The second part describes the first high-Q capacitively-loaded cavity resonator and filter that is compatible with direct print additive manufacturing. The presented design is a compromise between quality factor, cost and manufacturing complexity and to the best of our knowledge is the highest Q-factor resonator demonstrated to date using DPAM compatible materials and processes. The final version of the single resonator achieves a measured unloaded quality factor of 200-325 over the frequency range from 2.0 to 6.5 GHz. The two pole filter is designed using a coupled-resonator approach to operate at 2.44 GHz with 1.9% fractional bandwidth. The presented design approach simplifies evanescent-mode filter fabrication, eliminating the need for micromachining and vias, and achieving a total weight of 1.97 g. The design is fabricated to provide a proof-of-principle for the high-Q resonator and filter that compromises between performance, cost, size, and complexity. A stacked version of the two-pole filter is presented to provide a novel design for multi-layer embedded applications.

The fabrication is performed using an nScript Tabletop 3Dn printer. Acrylonitrile Butadiene Styrene (ABS) (relative permittivity of 2.7 and loss tangent of 0.008) is deposited using fused deposition modeling to form the antenna, array, resonator, and filter structures, and Dupont CB028 silver paste is used to form the conductive traces conductive regions (the paste is dried at

90 °C for 60 minutes, achieving a bulk DC conductivity of 1.5×10^6 S/m.). A 1064 nm pulsed picosecond Nd:YAG laser is used to laser machine the resonator and filter input and output feedlines.

CHAPTER 1: INTRODUCTION

1.1 Motivation

Additive manufacturing (AM) is an evolving technology that is rapidly expanding as well as finding its place across a broad array of industrial applications as it is a cost-efficient solution for low scale prototype and mass customizable production. This technology comprises of a category of digital manufacturing technologies that is enabling multi-material manufacturing and post-processing. The outstanding capability of AM to print lightweight structures to provide required mechanical support as a fixture, package, or structural member and also put up system devices and interconnects, all in an adjacent fashion is a very promising feature that can lead to an evolution in shaping future's manufacturing technologies, products, and applications [1]. According to [2] the 3D printing market had a compound annual growth rate of 66% during the period 2013 to 2014, and it is expected to have the same growth rate for many years. Furthermore, studies expect AM to have, on average, 50% less running cost, and 400% faster production from 2013 to 2018 [3].

AM processes that combines micro-dispensing and fused filament fabrication (FFF)/ fused deposition modeling (FDM), most likely dominate current applications due to their low process temperatures, dimensional flexibility/versatility, and wide range of readily available compatible materials. Fused deposition modeling (FDM) is based on the selective deposition of extruded material, which, while popular, is not the only 3D printing technology. A brief comparison between FDM, and other available 3D printing technologies is shown in Fig. 1.

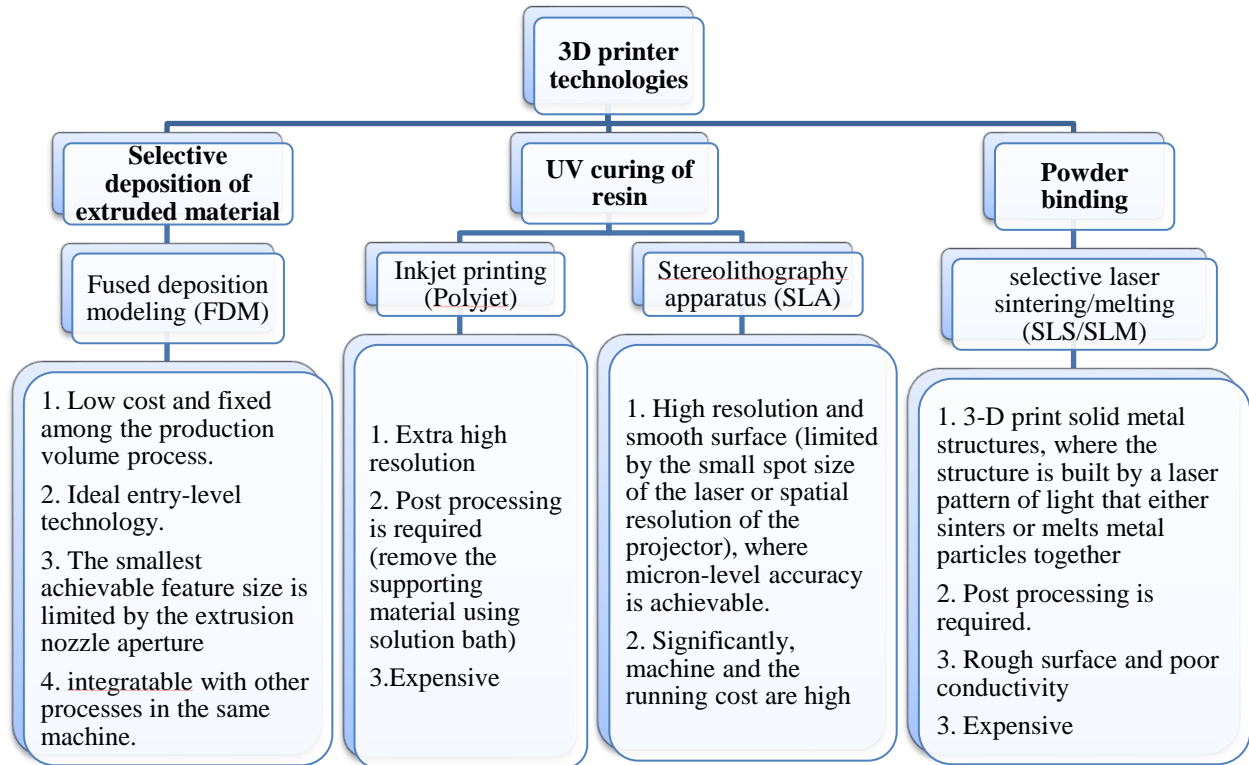


Figure 1.1: 3D printer technologies.

Besides micro-dispensing and fused filament fabrication, post processing compatibility proven to enhance the additivity manufactured circuits performance. An example of such post processing was presented in [4] where laser machining of micro-dispensed silver pastes traces boosted the conductivity of silver paste in coplanar waveguide (CPW) traces. The laser solidified an approximately 2- μm -wide region at the edges of the CPW slots, thus significantly increasing the effective conductivity of the film and improving the attenuation constant of the line. Furthermore, the performance and upper frequency range of CPW lines is limited by the cross-sectional shape and electrical conductivity of the printed paste, as well as the achievable minimum feature size which is typically around 100 μm and can be treated using laser machining. A Nd:YAG laser (Lumera Laser's SUPER RAPID-HE Picosecond laser) integrated with a 3D printer, such as nScript 3D printer, allows machining narrow slots into a layer of micro-dispensed silver paste

(Dupont CB028). Use of the laser solved the issue of minimum feature size. Due to the emission of very short pulses, the conductor is exposed to sudden high energy infrared (wavelength of 1064 nm) irradiation producing a cold ablation. This process completely decomposes thin layers of material at a controllable removal rate.

Moreover, rapid advancement in multi-material, direct digital manufacturing (DDM) technology is opening up new opportunities for innovative designs for printed electronics and antenna systems. Recent demonstrations show the potential for size miniaturization, performance improvement, increased reliability, and reduced complexity [5-10]. Also, literature reports that the material of 3D printing technology, especially thermoplastic, presents excellent electrical properties with relative dielectric constants in the range of 2-3 and dielectric loss tangent between 0.006-0.02 up to 10 GHz [11, 12]. Furthermore, Micro-dispensed conductive traces, such as Dupont CB028 silver paste, has proven to be operable for high frequency interconnects, despite the relatively low conductivity at microwave frequencies (1.5×10^6 S/m on average) [13]. These favorable electrical properties have resulted in several prototype microwave circuit designs including conductive traces [14, 15], 3D antennas [16-18], and structural electronics [19]. Other examples include a MMIC chip integrated on an additively manufactured substrate with decent performance up to 170 GHz [20] and an RF MEMS switch based on a 3D printed ohmic contact cantilever [21].

All the aforementioned AM capabilities and examples represent a solid base for a promising fabrication technique to develop and enhanced microwave circuits, antenna, and antenna arrays to meet the requirements of today's telecommunication systems. Also, it provides the ability to integrate and embed RF components through building a full system. AM reduces the materials waste, fabrication complexity and cost, as well as achieves miniaturized volume.

1.2 Contributions

The main contributions presented in the dissertation are summarized as follows:

- (a) Development of three dimensional, embedded, multi-layer, multi-material half-wave dipole: A new volumetric approach to realizing the 3D half-wave dipole in a packaged format is presented. This approach provides the ability to keep a signal distribution network in close proximity to the ground plane, facilitating the implementation of ground connections (e.g. for an active device), mitigating potential surface wave losses, as well as achieving a modest length reduction.
- (b) Development of new approach for implementing conformal antennas using DPAM: This new approach is based on fused deposition printing of a 150 micron-thick thermoplastic layer on top of Kapton tape forming a smooth, thin and flexible substrate. The antenna metallization is then printed on the smooth face of the flexible substrate using micro-dispensing, and the substrate is subsequently adhered to a 3D form. The approach is useful for accomplishing 3D conformal designs, allows conductors to be printed on relatively smooth surfaces of FDM-printed substrates, and allows for faster conductor printing with excellent dimensional control. This method also eliminates the challenges of silver paste dispensing on structures with sharp edges or inclined planes.
- (c) Development of an arrangement of 3D designed half-wave dipole antenna elements in a three dimensional fashion to form a 2×2 array: The design improves the overall array performance by exploiting the single element advantages, and the advantages of having them in a non-planar configuration, such as controlling the array beamwidth. Furthermore, it provides the ability to reduce the array footprint by using the 3rd dimension.

- (d) Development of S/C-band evanescent-mode cavity resonator that can be manufactured using DPAM: The design approach simplifies the evanescent-mode resonator fabrication, avoiding any need for micromachining or vias. To the best of the authors' knowledge is the highest Q-factor resonator demonstrated to date using DPAM compatible materials and processes.
- (e) Development of first capacitively-loaded cavity band pass filter (BPF) that is compatible with direct print additive manufacturing: Two proposed designs are described; laterally coupled and vertically coupled filters. The presented design approach simplifies the evanescent-mode filter fabrication, eliminating the need for micromachining and vias, and achieving a total weight of 1.97 g, and 1.91 g for the laterally coupled, and vertically coupled respectively. Both designs present 40.12% and 35.43% volume reduction.

1.3 Dissertation Organization

This dissertation is comprised of five chapters, including the current chapter, which introduces the dissertation topics, motivations, background, and contributions. The rest of the dissertation chapters are organized as follow:

- (a) Chapter 2 introduces the additive manufacturing fabrication process, and briefly describes why additive manufacturing is suitable technology for radio frequency applications. It provides a literature review for the main two topics in this dissertation; (a) non-planar antenna, and antenna array, and (b) capacitively-loaded cavity resonators and filters. Besides, the advantages and the drawbacks of the fabrication technologies used are described.

- (b) Chapter 3 presents detailed design approaches, fabrication techniques, and measurements of the embedded 3D-printed and conformal half-wave dipole antenna, and antenna array, which represents the first main topic in this dissertation. The proposed single antenna design is presented first along with the fabrication approach and the analysis of roughness effects on the antenna performance. This done by analyzing the roughness of additively manufactured transmission lines. The second topic in chapter discusses a new process for implementing 3D microwave devices using flexible substrates, where the assembly steps of this process are defined. The single element antenna is fabricated using the proposed approach to provide proof-of-principle on the approach. The last topic in this chapter discusses the non-planar antenna array, where four elements of the three-dimensional antenna element are integrated together to form a 2x2 non-planar array.
- (c) Chapter 4 discusses the topic of high-Q evanescent-mode cavity resonator and filter. This chapter is divided into three sections: the first part presents the DPAM capacitively-loaded cavity resonator, its fabrication process, challenges, and tunability. The second section presents an enhanced version of the capacitively-loaded cavity resonator, and two-pole laterally coupled capacitively-loaded cavity band pass filter. The fabrication process, the assembly steps, and tunability are presented as well. Finally, a novel vertically stacked design of the capacitively-loaded cavity band pass filter is presented. The design analysis, fabrication process, assembly steps, and measurement are described.
- (d) Chapter 5 summarizes this dissertation and presents the recommendations for future work.

CHAPTER 2: LITERATURE REVIEW AND BACKGROUND

2.1 Introduction

Additive manufacturing has been synonymous with rapid prototyping since its invention in the early 1980s. The American Society of Testing and Material (ASTM) defined the additive manufacturing as “the process of joining materials to make objects from 3D model data, usually layer upon layer, as opposed to subtractive manufacturing methodologies” [22]. AM had its tipping point in the radio frequency (RF) field in the last few years, as the fabrication resolution/accuracy, and the RF properties of the printing material have been dramatically enhanced. According to literature, additively manufactured RF devices are reported to operate over a wide range frequencies, starting from a few megahertz up to millimeter-wave and terahertz frequencies [23-27]. The wide spectrum of high performance 3D microwave circuits and antennas, along with the AM capabilities to achieve complicated structures, and reduce the materials waste are defining the next generation of RF components and systems.

2.2 Non-Planar Antenna and Antenna Array

3-D antenna design is one of the promising techniques, where having miniaturized, high efficiency and large bandwidth antennas is possible [28-32]. In [28] the design of an electrically small 3-D cube antenna is presented (Figure 2.1 (a)), where the antenna consists of a balun and a half-wave dipole with meander-line portions, all of which are patterned on the surface of a cube. Adopting this 3-D structure allowed the author to achieve a compact and highly efficient antenna

at the same time for a passive wireless sensor node application. Similar designs of cube-shaped dipole antennas are described in [29, 30, and 31], as shown in figure 2.1(b)-2.1(d). In [29], the author used liquid crystal polymer (LCP) material (ULTRALAM 3908) to achieve compact and cube antenna with omnidirectional-pattern. The cube interior is suggested to be used to embed the electronics for a wireless sensor node application. Similarly, in [30], a 3-D antenna is ink-jet printed on a paper substrate to achieve compact design with isotropic radiation pattern. The author exploited the cube interior to embed the required electronics inside. A spherical helix, a meander line and a hybrid antenna fabricated on the top of glass hemispheres using a conformal printing technique are presented in [32], figure 2.1(e).

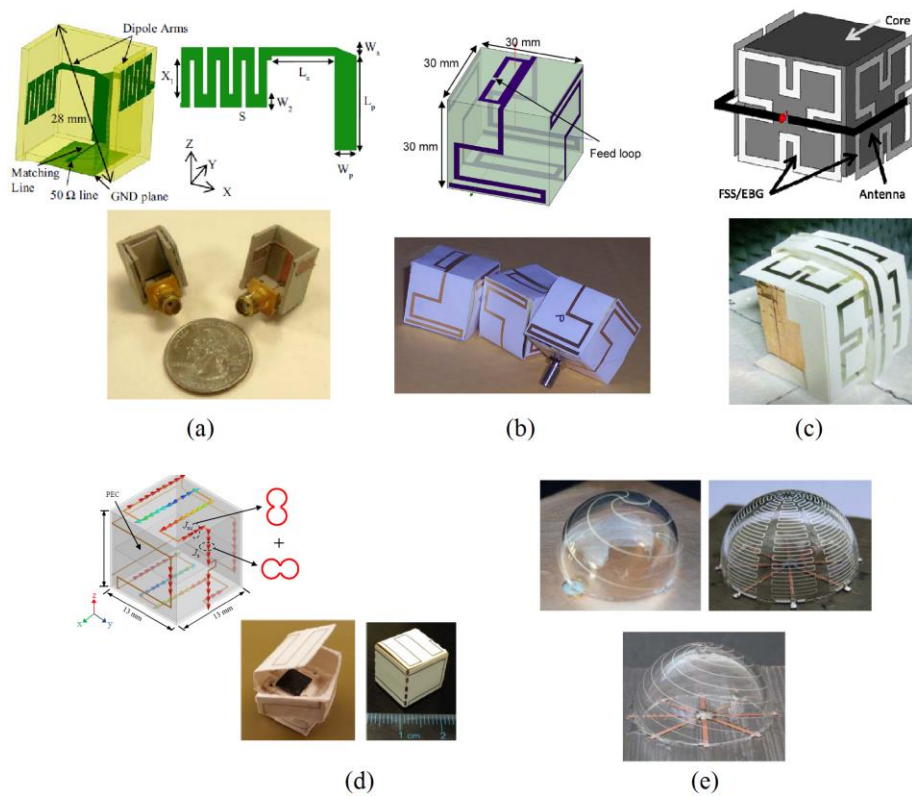


Figure 2.1: Non-planar antenna designs using several fabrication technique. (a) meander-line dipole cube-shape antenna [28] 2013 © IEEE (b) omnidirectional-pattern cube antenna [29] 2009 © IEEE (c) Ink-jet printed antenna [30] 2014 ©IEEE (d) cube antenna with embedded electronics [31] 2012 © IEEE (e) Hemisphere-shape antenna [32] 2011 ©IEEE.

The arrangement of antenna elements in a non-planar fashion (i.e., 3-D configuration) also is found to be attractive as it combines many advantages and adds additional capabilities to the array such as beamforming control, reconfigurability, improved functionality and performance, polarization control, and adding anti-jamming capability [33-40]. Figure 2.2 shows four examples of non-planar arrangement of several antenna types, such as dipole, Yagi-Uda, and dielectric rod antennas. A log-periodic dipole array (LPDA), with dual polarization and large operational bandwidth, has been achieved in [34] by setting the dipole elements in a 3-D structure as shown in Figure 2.2(a). In [35], a reconfigurable Yagi antenna is realized by adopting a tridimensional structure, achieving asymmetric and reconfigurable radiation pattern. Having such structure, which is carried by rotating the directors around the driver gradually (Figure 2.2(b)), results a high rejection between sectors in a plane. In addition, an array of three elements of dielectric rod antennas is configured on top of curved structure to realize a switched-beam transmitter is presented in [37], where the array increases the scanning range, but maintain the same performance for different scanning angles (Figure 2.2(c)). In [38], an endfire array of dipole antennas are arranged a 3-D fashion to enhance the array's gain and efficiency. As shown in Figure 2.2(d), adopting the 3-D structure enabled the design to have high gain without the need for additional structures such as reflectors or directors in Yagi antenna. Furthermore, anti-jamming capability is achieved for GPS receiver by adopting a non-planar antenna array, with a large curvature, and convex surface, where the more the elements the better the performance [39]. A comparison between having the elements in planar and non-planar arrangement is carried out in [40], where the pros and cons of each arrangement is described. Finally, an analytical solution for shaped-beam non-planar array is described in [41], where the phasing is generated by shaping the substrate, not the feeding network.

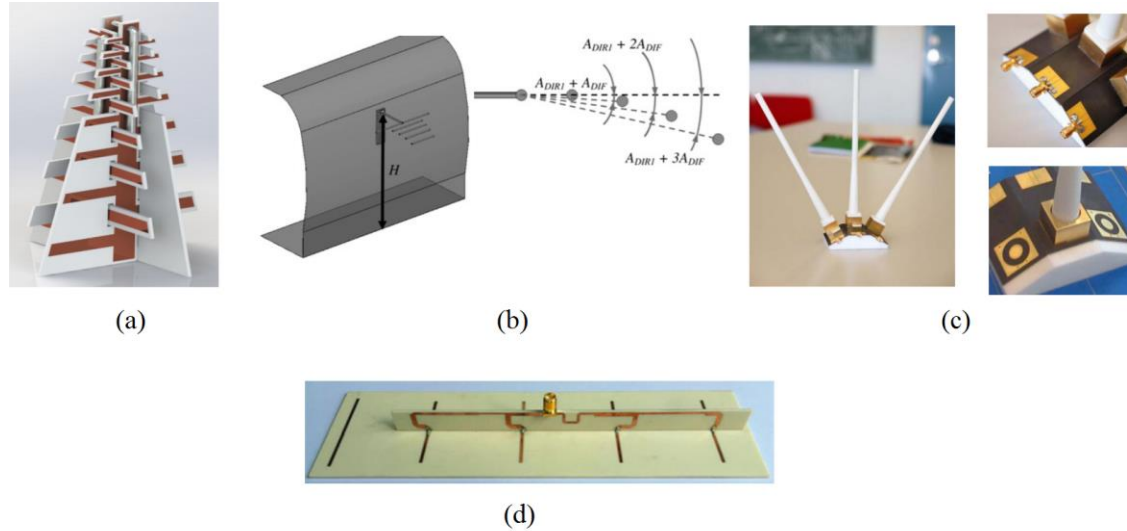


Figure 2.2: Non-planar antenna array designs. (a) non-planar dipole antenna array [34] 2017 ©IET (b) tridimensional Yagi antenna [35] 2010 ©IET (c) non-planar dielectric rod antenna array [37] 2014 ©IEEE (d) non-planar printed dipole antenna array [38] 2017 ©IEEE.

All of the aforementioned designs, except the spherical antenna, Yagi antenna, and the dielectric rod antenna, are fabricated in a planar manner and then folded to form a 3D cubic shape with the antennas located on one or more sides of the cube. Post-fabrication assembly steps would be a complex manufacturing approach, compared to multi-layer printed circuit boards (PCBs) for example. Furthermore, the printing of circuitry (matching networks, feed lines, etc.) is possible only on the sides of the cube and not within its volume.

Another way to achieve non-planar antennas is to use flexible substrate, and conform it into a non-planar surface. In general, flexible antennas are gaining in popularity with the growth of wearable electronic devices and the overall utility of conformal integration. Many designs are available in the literature for various antenna types and different applications [42-47]. In [42] and [43] a bow-tie antenna on top of heat stabilized polyethylene naphthalate (PEN) flexible substrate is presented, where the authors conformed the proposed antenna on top of a curved surface and

analyzed the effects of curvature on the pattern and resonance frequency. Another fabrication technology is presented in [44], where a UHF antenna and solar cell array are printed on top of a thin Kapton sheet. The antenna is formed by depositing an Al layer using a shadow mask and e-beam evaporation. In [45], a flexible PCB is used for the design of a flexible ultra-wide band antenna for mobile devices applications. An investigation on the radiation pattern of 5.8 GHz flexible patch antenna is presented in [46], where the change in pattern and resonance frequency versus changes in the bending angle are described. A similar investigation of flexible antennas is described in [47], which uses copper-etched antennas on flexible polyimide substrates.

2.3 Capacitively-loaded Cavity Resonator and Filter

Highly selective filters are key components to enable efficient usage of the crowded electromagnetic spectrum. Among the available filter architectures, evanescent mode capacitively-loaded approaches have received significant attention since they offer high quality factors, a large spurious-free region, compact volume, and can be made tunable. There are several papers that present the use of microelectromechanical systems (MEMS) to design evanescent mode cavity resonators and filters [48-57]. Figure 2.3 presents an example on high-Q evanescent-mode tunable MEMS resonator and filter that is tuned using electrostatic actuations. High-quality factor resonators and filters can be realized along with tunability using other fabrication technologies such as Yttrium iron garnet (YIG) [58-61], which can provide wide tuning range, and handle high power. The disadvantages of YIGs include the large volume and high power consumption, while for the MEMS filters, manufacturing complexity and cost are the main disadvantages. The unloaded quality factor (Q_u) of YIGs can reach 10,000 at 10 GHz [60], while MEMS resonators reported to have measured unloaded quality factor of 460–530 in the range 3.4 – 6.2 GHz [55].

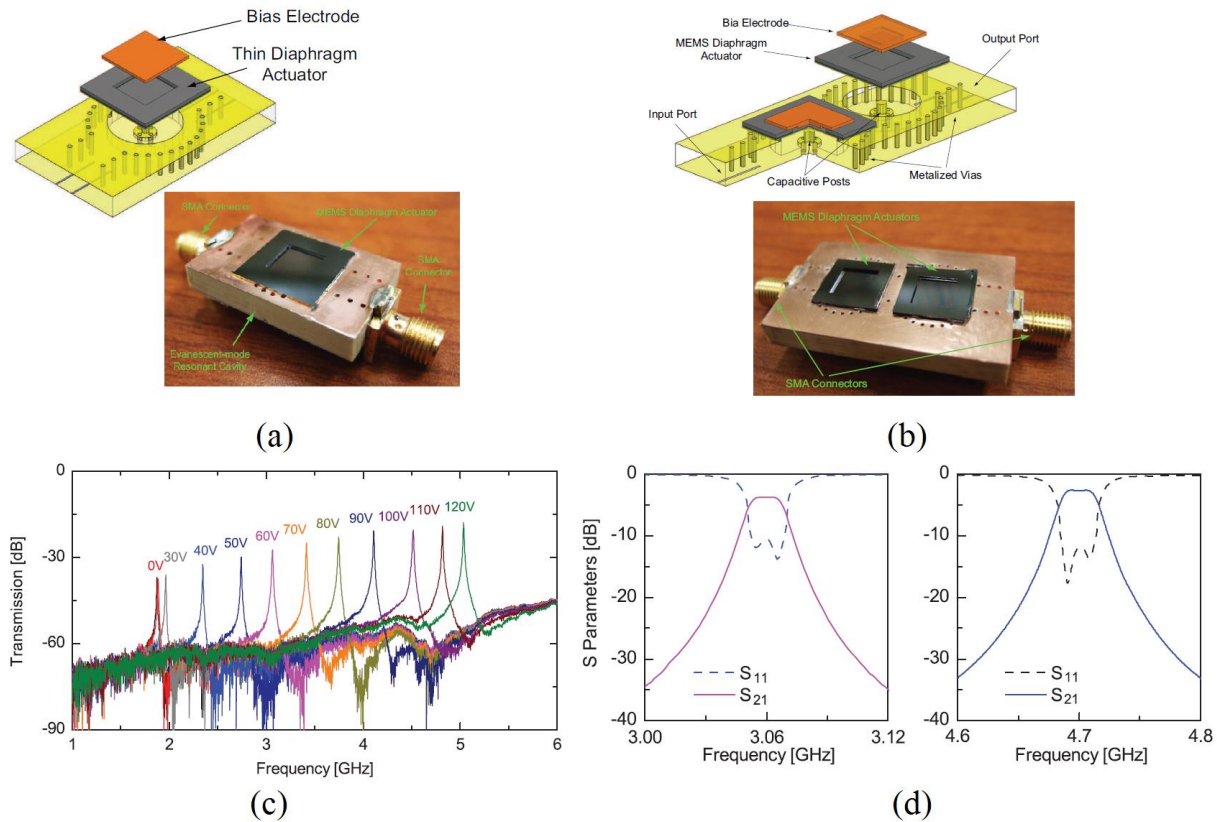


Figure 2.3: Evanescent mode capacitively-loaded resonator and filter. (a) Resonator structure (b) Filter structure (c) Resonator transmission (S_{21}) (d) Filter s-parameters. [73] 2010 ©IEEE.

On par, additively manufactured high-Q resonators and filters are reported in literature achieving a high unloaded quality factor and low insertion loss performance [62-65]. A Stereolithography based, 3-D printed resonator and filter is presented in [63] as shown in Figure 2.4(a), where the resonator achieved unloaded quality factor between 11039 and 14450 at 10 GHz. As well, in [64] a cavity resonator is fabricated using stereolithography process and presents a measured unloaded quality factor of 3005 at 19.87 GHz. Finally, a Ku/K band filters are fabricated using Selective Laser Melting Manufacturing (SLM) AM technology is presented in [65] as shown in Figure 2.5(b). Selective Laser Melting as AM fabrication technology require no machining to build the whole metal parts, which reduces the cost and time, and provide design flexibility. Figure

2.5 presents antenna feed network, working at the same band (i.e., a Ku/K band), for satellite application. Although these filters achieve a very low insertion loss (~ 0.1 dB), but they may require post processing steps such as plating.

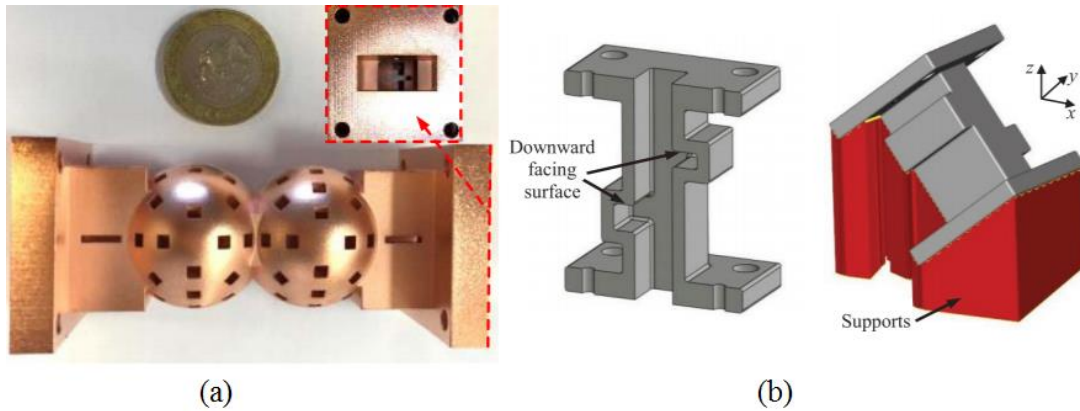


Figure 2.4: Additively manufactured high-Q resonators and filters. (a) X-band stereolithography based filter [63] 2016 ©IEEE (b) Selective Laser Melting Manufacturing (SLM) based Ku band filter [65] 2017 ©IEEE.

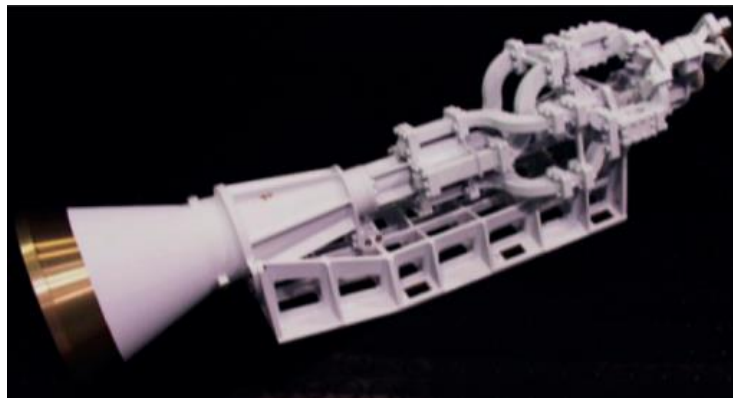


Figure 2.5: Antenna feed system built using selective laser melting fabrication process. [65] 2017 ©IEEE.

CHAPTER 3: EMBEDDED 3D-PRINTED AND CONFORMAL HALF-WAVE DIPOLE ANTENNA, AND ANTENNA ARRAY¹

3.1 Introduction

The need for compact and efficient antennas has focused significant attention onto design approaches that compromise between physical size and performance. 3-D antenna design is one of the promising techniques, where having miniaturized, high efficiency and large bandwidth antennas is possible. Volumetric designs that are compatible with 3D printing provide flexibility in forming the substrate shape and printing the conducting traces and antenna elements. For example, a true volumetric design would offer the benefits of multi-layer PCB design but with the added capability of running controlled impedance transmission lines in arbitrary directions through the substrate.

3.2 Embedded 6 GHz 3D-Printed Half-Wave Dipole Antenna

3.2.1 Antenna Design

In this work, a new volumetric approach to realizing a 3D half-wave dipole in a packaged format is introduced. Direct digital manufacturing (DDM) with an nScript Tabletop 3Dn printer is used to fabricate a non-planar 3D substrate on which the 6 GHz antenna and its feed network are printed in a conformal manner. The presented design provides the ability to keep a signal distribution network in close proximity to the ground plane, facilitating the implementation of

¹ The content of this chapter has been published in [6], [89], and [90], and it is included in this dissertation with permission from the IEEE. Permission is included in Appendix A.

ground connections (e.g. for an active device), mitigating potential surface wave losses, as well as achieving a modest (10.6%) length reduction. An analysis of the substrate surface roughness is included to explain its effect on the antenna performance.

The antenna consists of a 3-D implementation of a half-wave dipole printed on the top layer of a substrate and fed through an inclined grounded coplanar waveguide (GCPW) balun that is matched to the 50 ohm feed line using a GCPW quarter-wave transformer, as shown in Figure 3.1. The antenna is shielded using a ground plane that is located $\sim\lambda/4$ away from the dipole at the design frequency. Since the transmission line characteristic impedance is a function of distance from the lower ground to the GCPW, the balun presented in [66] has been modified to optimize the GCPW characteristic impedance along the inclined plane. The antenna is designed to operate at 6 GHz using acrylonitrile butadiene styrene (ABS) substrate material ($\epsilon_r \sim 2.7$ and $\tan\delta \sim 0.008$), with a total size of $24 \times 22 \times 6.25$ mm³; the antenna dimensions are presented in Table 3.1. Four vias connecting the upper and lower grounds of the GCPW line are incorporated to avoid undesired resonances around the design frequency. Simulation data also show that these vias reduce the antenna sensitivity to the surrounding environment. As a final step the antenna is embedded in ABS to produce the packaged version shown in Figure 3. 2 (a) Fused deposition modeling (FDM) is used to print the ABS layers, while micro-dispensing of Dupont CB028 silver thick film paste (bulk DC conductivity of 1.5×10^6 S/m) is used for the conductor deposition.

A planar version of the antenna is analyzed to evaluate the advantages of the 3D design approach. The planar design is fabricated using a conventional copper etching process on a 0.508 mm-thick Rogers 4003C substrate ($\epsilon_r \sim 3.38$ and $\tan\delta \sim 0.0027$). The substrate is attached to a 4.18 mm-thick grounded ABS layer (Figure 3.2 (b)) in order to provide the required separation between the antenna and the ground plane.

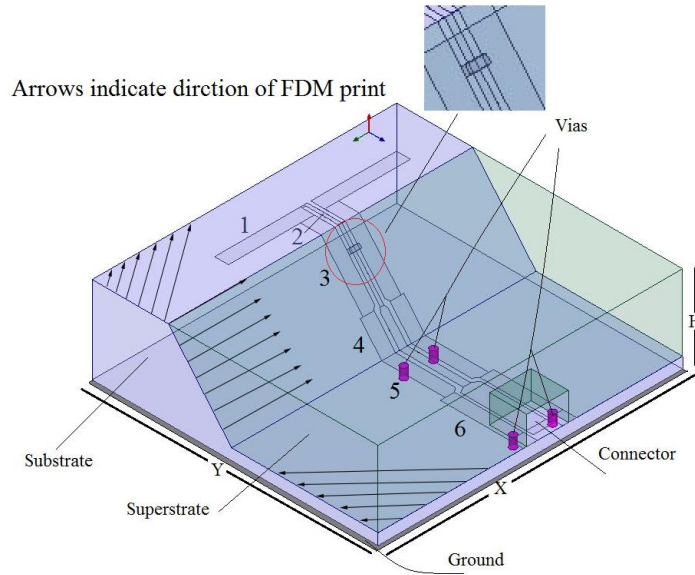


Figure 3.1: 3D 6 GHz antenna design. The arrows in the figure show the direction of the fused deposition modeling (FDM) head during the substrate printing process.

Table 3.1: Dimensions of the 3D antenna in mm.

TL	Length	Signal Width	Gap Width	Top Ground Width
1	6.2	1.0	0.25	1.0
2	2.5	0.25	0.25	1.0
3	4.7	0.25	0.25	1.0
4	2.41	0.55	0.30	1.0
5	4.58	0.55	0.30	1.0
6	5	1.44	0.20	1.0

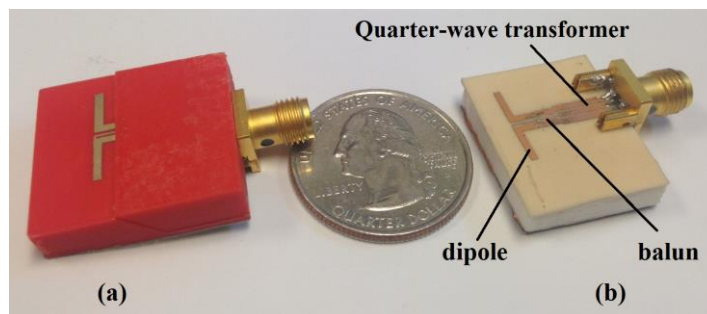


Figure 3.2: The embedded 3D antenna (a) and planar version (b).

3.2.2 Experimental Results

The measured data for the two antenna designs are in good agreement with simulation results obtained using Ansys HFSS. The S_{11} of the 3-D antenna, shown in Figure 3.3, shows a 220 MHz frequency shift and a difference in the return loss bandwidth between the simulated and measured data, due to roughness of the ABS substrate (see Section 3.2.3). The maximum measured gain is 4.7 dBi as shown Figure 3.4(a), which is 0.18 dB less than the simulated gain. The difference in gain values is also due to the substrate surface roughness, which decreases the effective RF conductivity of the printed silver traces [13].

The electromagnetic characteristics of the planar structure are similar to the 3D design. The measured 6 GHz E-plane gain patterns for both antennas are nearly identical as shown in Figure 3.4 (b). The measured (5.62 dBi) and simulated (5.89 dBi) peak gains of the planar antenna are higher than those of the 3D design because of the lower loss tangent of the substrate material, and the higher conductivity of the conductors. There is excellent agreement between the measured and simulated S_{11} for the planar antenna, with a return loss greater than 20 dB at the design frequency (Figure 3.5). As opposed to the 3D antenna, however, the resonances above and below the center frequency are unstable and very sensitive to the test setup.

To this point, one of the important advantages of the 3D design over the planar design is that the CPW feed line is kept in close proximity to the ground plane, thereby reducing surface wave effects. For example, it was found through simulation that the planar antenna S_{11} response is much more sensitive to lateral displacements of the feed and antenna toward the edge of the substrate, than is the 3D design. As shown in Figure 3.6 (a), resonances near 4.8 GHz and 7.8 GHz and the center frequency response are strongly affected as the planar antenna approaches the edge of the substrate. Conversely, there is no impact on the resonances and 50% less shift in the center

frequency for the 3D antenna (Figure 3.6 (b)). The resonances at 4.8 and 7.8 GHz correspond approximately to the frequencies when the substrate width is a multiple of $0.5\lambda_g$ ($\lambda_g = \frac{c}{f\sqrt{\epsilon_r}}$). It was also observed through simulation that additional resonances around the center frequency, and a reduction in gain, appear only with the planar design when a $50\ \Omega$ transmission line is added between the quarter-wave transformer and the connector; this additional length of line increased the total substrate length to $>\lambda_g/2$ at band center. These simulation results suggest that the feed network of the planar design leaks more energy into the TM_0 surface wave mode than does the 3D design, and the resulting resonances are dependent on the dimensions of the substrate and the path of the feed network. These are effects that would complicate the use of the planar antenna in a more complex configuration such as an array. The use of ~ 6.0 mm-long vias to connect the CPW to the lower ground in the planar antenna is difficult in practice and ineffective at equalizing ground plane potential.

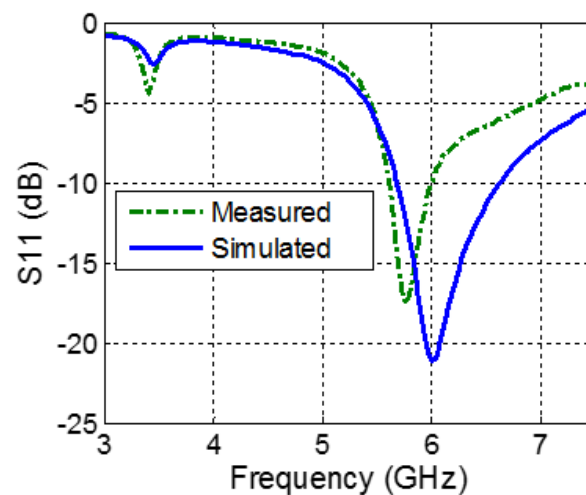


Figure 3.3: S_{11} of the 3D antenna.

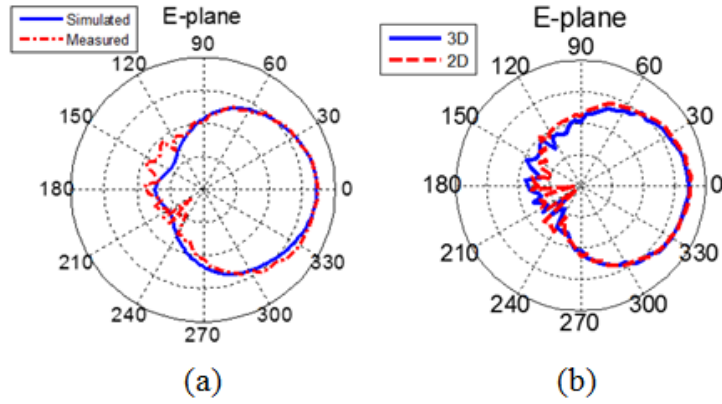


Figure 3.4: 6 GHz antenna patterns. (a) simulated and measured realized E-plane gain pattern of the 3D antenna, and (b) comparison of measured 3D and planar (2D) antenna patterns. Both graphs are 10 dB/division.

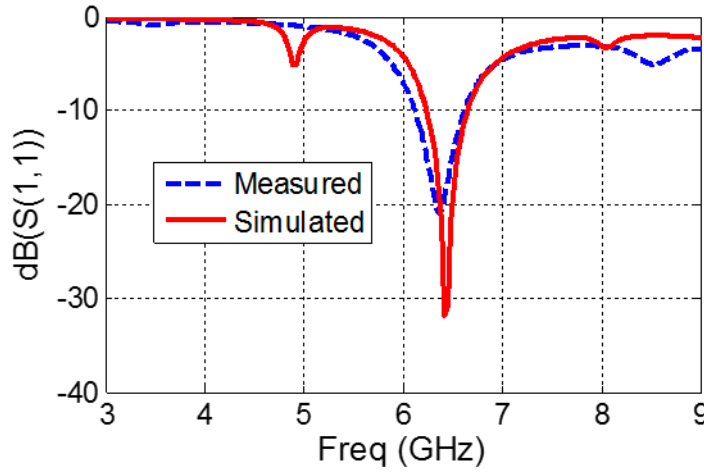


Figure 3.5: S_{11} of the planar antenna.

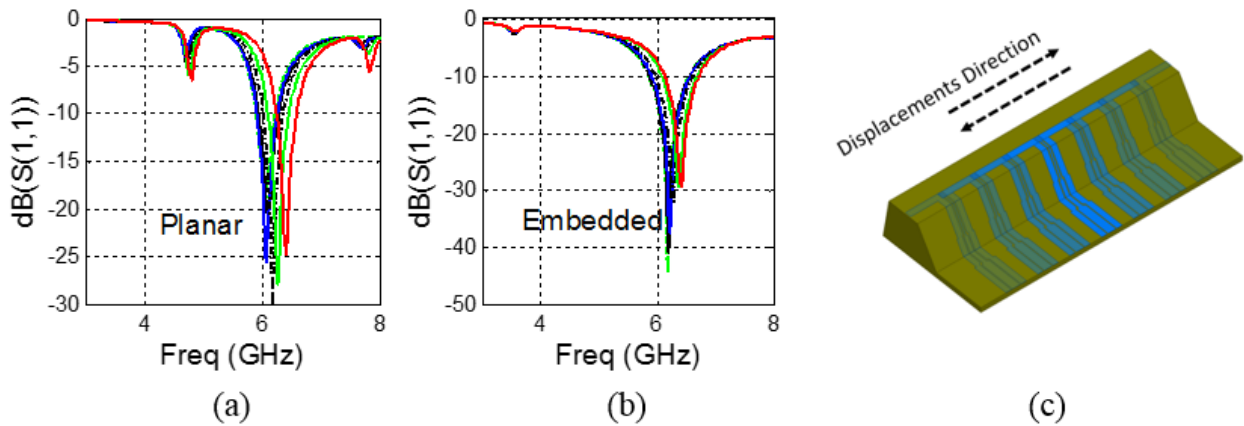


Figure 3.6: Surrounding environment changes effect.

3.2.3 Analysis of Surface Roughness Effects

The effect of surface roughness on eddy current losses of transmission lines at microwave frequencies was examined as early as 1949 [67]. Studies of square and triangular surface grooves and scratches reveal that the effective conductor length and resistance increase with frequency, as the skin depth becomes comparable to the groove size. Models such as those of Groiss [68] and Huray [69-71] capture this physical phenomenon and provide empirical formulas that describe the surface roughness effect; the surface roughness is assumed to be much smaller than the trace thickness and is described as a sinusoidal wave in the Groiss model and as spheres/nodules in the Huray model. Required model parameters are typically available from material vendors, and the Groiss and Huray models are built into some commercial full-wave simulators (e.g. Ansys HFSS). The roughness size and skin depth are the main factors determining the increase in transmission line resistance, $fact_R$

$$Z_{rough} = Z_{smooth} \times fact_R \quad (3.1)$$

where Z_{rough} is the rough surface impedance and Z_{smooth} is the smooth surface impedance. The factor $fact_R$ is described by Groiss and Huray in (3.2) and (3.3), respectively:

$$fact_R = 1 + e^{-\left(\frac{\delta}{2 \times S}\right)^{1.6}} \quad (3.2)$$

$$fact_R = 1 + \frac{1.5 \times S_r}{1 + \frac{\delta}{a} + \frac{\delta^2}{2a^2}} \quad (3.3)$$

where δ is the skin depth, S is the surface roughness, S_r is the ratio of the surfaces of all spheres/nodules in a cut and the cut surface, and a is the radius of spheres/nodules. These parameters are typically available from material vendors.

In the 3D printing process, the roughness could be represented with a combination of the aforementioned models, since the substrate resembles a sinusoidal surface and the silver paste is better represented by spheres due to its particle-like nature [13]. However, while these models may emulate the increase in loss due to roughness, the potential change in phase constant is not addressed. Also, as described below, the surface roughness of 3D printed substrates can be comparable to or greater than the trace thickness. Recently, the effect of roughness on the loss of a filter printed using the Polyjet technology has been investigated using the Huray model in numerical electromagnetic simulations [72].

In this work the effects of the surface topology are studied using simulations of physical models that are representative of the surface produced by the FDM process. The simulation models are of the type shown in Figure 3.7, which shows a CPW transmission line on a smooth substrate and one on a corrugated surface of the type resulting from an FDM print; the ground planes are removed for clarity. For the simulated models the signal line width is 600 μm , the signal to ground spacing is 200 μm and the ground plane width is 1000 μm ; these dimensions match those of the quarter-wave transformer in Figure 3.1.

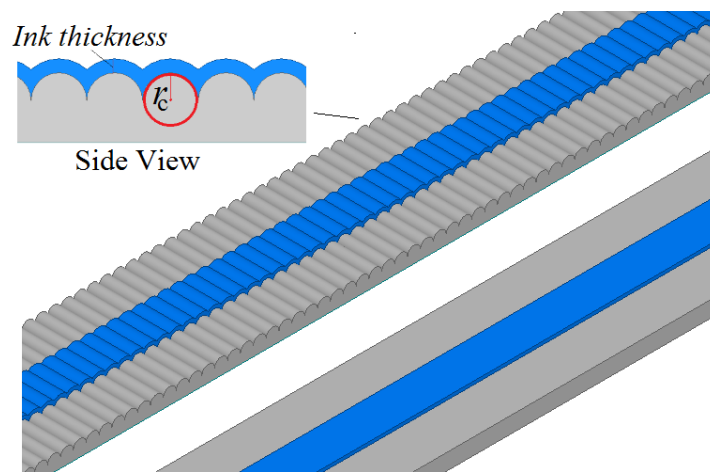


Figure 3.7: Smooth and corrugated $\lambda/4$ transformers. The length is 8 mm and the signal line width is 600 microns. The CPW ground is not shown for clarity.

The lines are 8 mm in length. Corrugation profiles (refer to the inset in Figure 3.7) from $r_c=12.5 \mu\text{m}$ to $r_c=100 \mu\text{m}$ are analyzed, as these represent the typical range of printer settings used for the FDM prints and have been validated with profilometer measurements on fabricated samples. For all simulations a silver paste thickness of $20 \mu\text{m}$ is used. The paste roughness is not taken into consideration as it is difficult to control, being a function of factors that include paste thickness, printing speed, temperature and humidity. The propagation constant β has been extracted from the full-wave simulation results by fitting the data to an ideal transmission line model using Keysight Technologies Advanced Design System software. The propagation constant β normalized to the value for the smooth substrate is shown versus corrugation parameter r_c in Figure 3.8. The corrugated line exhibits up to 6% change in β for $r_c=100 \mu\text{m}$ compared to the smooth substrate. The corrugated design also has a significantly larger attenuation constant (Figure 3.9) which is consistent with previously stated conclusions in the literature [68-71]. The changes in the phase constant due to the rough surface also contribute to differences in the measured and predicted 10 dB return loss bandwidth, as confirmed by independent measurements of a printed antenna on a smooth ($r_c < 2 \mu\text{m}$) substrate.

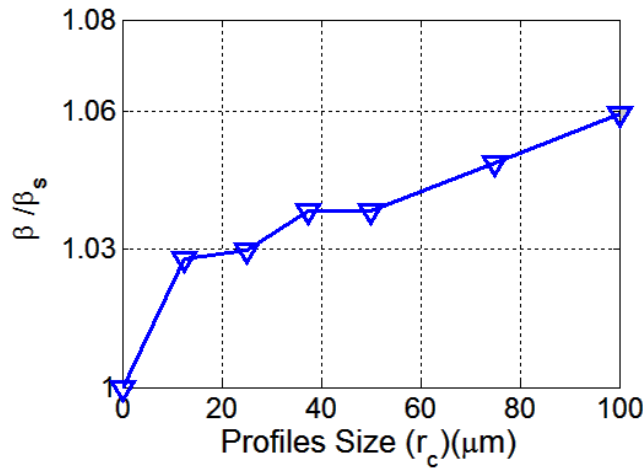


Figure 3.8: Simulated propagation constant (β) of the corrugated $\lambda/4$ transformer normalized to β_s for the smooth substrates.

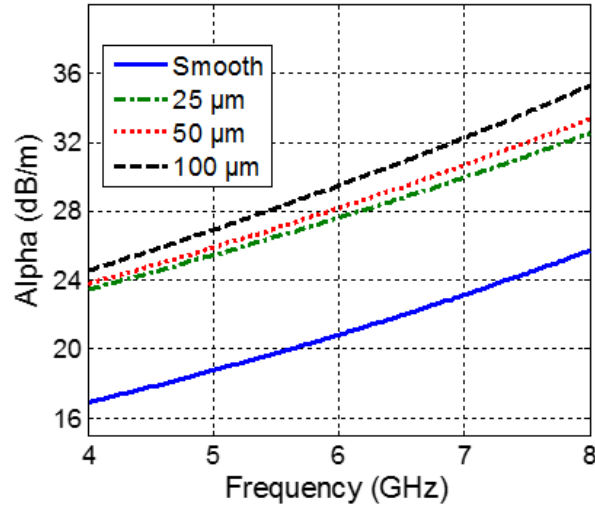


Figure 3.9: Simulated attenuation constant (α) of corrugated and smooth transmission lines for various corrugation profiles (r_c).

The results of this simulation study can be used to explain the discrepancies between the simulated and measured data of the 3D antenna presented in the previous section. A full-wave simulation of the entire 3D structure that includes the surface roughness profiles would be quite complex and computationally intensive given the varying alignment between the FDM print head direction and the conductive traces, and the variations in roughness profile over the full surface area. Instead, the quarter wave transformer serves as a representative section to demonstrate the roughness effects; as shown in Figure 3.1 it is aligned orthogonal to the roughness contour as assumed in Figure 3.7, and for the fabricated 3D antenna it has a measured corrugation profile of $r_c=25 \mu\text{m}$. Per Figure 3.8 the relative increase in β is $\sim 3.0\%$ which is consistent with the 3.7% frequency shift (220 MHz) shown in Figure 3.3. As well, based on Figure 3.9, the expected loss along the 19.7 mm distance from the input port to the dipole for the smooth substrate is 0.41 dB, while for the corrugated line it is 0.55 dB. Hence, the expected additional loss due to roughness is ~ 0.14 dB which is nearly equal to the difference between the measured and simulated antenna

gain. Finally, it is found that, at low frequencies, there is <10% change in S_{21} when changing the orientation of the FDM print (see Figure 3.1) with respect to the paste direction (e.g., 45° or 0°).

3.3 A Multi-Material 3D Printing Approach for Conformal Microwave Antennas

3.3.1 Design Digest

Herein, a new approach for implementing 3D microwave devices using flexible substrates is presented, using a combination of micro-dispensing and fused deposition modeling (FDM) for fabrication. Dupont CB028 silver thick film paste is a popular material used with micro-dispensing for conductor deposition, given its relatively low curing temperature (90 – 150 °C), its viscosity (15,000 to 30,000 cP), and its ability to flex after curing. However, tight dimensional control when micro-dispensing CB028 over conformal structures can be difficult to achieve, especially over objects with sharp angles or inclined planes. The approach used here is to print a thin layer of thermoplastic substrate using fused deposition modeling, deposit the CB028 patterns, and then leverage the flexibility of the CB028 by forming the thin and flexible substrate to the desired 3D surface. As an example of the proposed approach, a 6 GHz 3D half-wave dipole is presented, where the antenna and circuitry are placed along a 3D acrylonitrile butadiene styrene (ABS) structure in a conformal manner. An additional advantage of this approach is that the thin substrates on which the conductors are printed can be more than 3x smoother than when printing directly on 3D structures fabricated using the fused deposition modeling process, thereby increasing the effective RF conductivity of the printed lines.

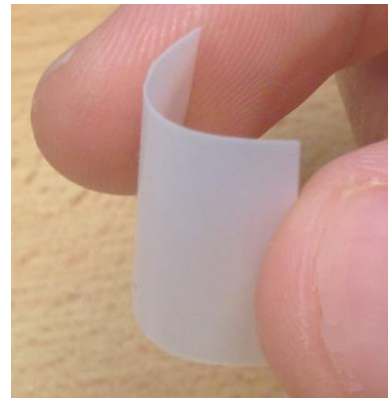
3.3.2 Fabrication Approach

This work uses an nScript 3Dn Tabletop printer that combines fused deposition modeling and micro-dispensing on a common gantry capable of 2 micron position accuracy. The advanced

capabilities of the FDM printer provide the ability of printing thin thermoplastic layers down to 50 ~ 75 μm , and these layers can act as a base for the conductor deposition as shown in Figure 3.10 (a). The flexible ABS substrate (Figure 3.10 (b)) is printed on top of Kapton tape to provide a smooth face and then this face is turned over to be used for the silver paste deposition. Once the conductor is deposited on the thin layer, the flexible substrate is affixed to a 3D ABS structure produced via FDM in a conformal manner. A diagram that describes the steps involved in the proposed approach is shown in Figure 3.11.



(a)



(b)

Figure 3.10: Fused deposition modeling process (a) printing of thin ABS substrate (b) Flexible ABS substrate (150 microns thick).

There are several important advantages gained by having a smooth surface on which the silver paste is deposited. As shown in [5], a reduction in surface roughness also reduces the attenuation constant of the printed lines. From a fabrication standpoint, the print speed during the micro-dispensing process can be increased and the line width control is enhanced when printing on smoother surfaces. Finally, the smooth surface improves the adhesion of the flexible substrate to the 3D structure and minimizes air gaps which can alter the propagation constant along the transmission lines.

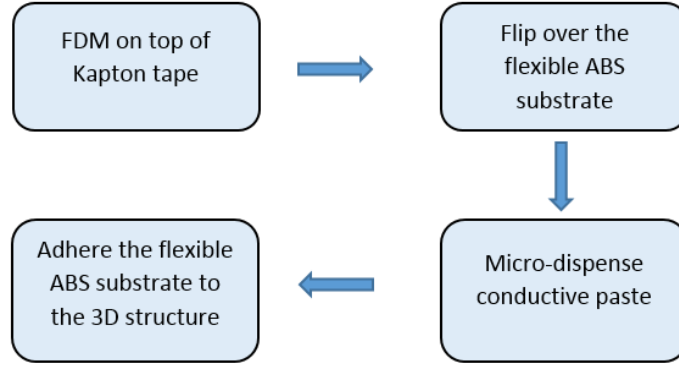


Figure 3.11: Steps involved in the fabrication process.

3.3.3 Design Example

The described fabrication process is applied to a new volumetric approach to realizing a 3-D half-wave dipole, where the presented design enhances antenna gain and minimizes surface-wave loss. The 3D antenna structure consists of a half-wave dipole located on the top layer of a 3D substrate, $\sim\lambda/4$ from the bottom ground plane at the design frequency, and the feeding is achieved via an inclined grounded coplanar waveguide (GCPW) balun. A GCPW quarter-wave transformer is incorporated to match the balun to the 50 ohm feed line, as illustrated in Figure 3.12. The ground plane is deposited on the bottom of the 3D structure for shielding purposes. Due to the variation of the transmission line characteristic impedance as the distance from the lower ground to the GCPW increases along the inclined plane, the balun presented in [66] has been adopted and modified to optimize the GCPW characteristic impedance along the inclined plane. The antenna design frequency is 6.0 GHz and acrylonitrile butadiene styrene (ABS) substrate material ($\epsilon_r \sim 2.7$ and $\tan\delta \sim 0.008$) is used, with a total size of $21 \times 22 \times 6.25$ mm³. The flexible substrate (150 μ m thick) is fabricated by printing two 75 μ m layers, and then the conductive layer (including the dipole, balun, matching network and feeding line) are deposited on the smooth face of the flexible

substrate as shown in Figure 3.13. A profilometer scan for the smooth (bottom (Kapton) side) and rough (top side during FDM print) surfaces of the flexible ABS substrate is shown in Figure 3.14. The measured surface roughness (R_a) is $9.14 \mu\text{m}$ and $2.8 \mu\text{m}$ for the rough and smooth faces, respectively. The conductivity used to model the CB028 silver paste is $0.6\text{e}6 \text{ S/m}$.

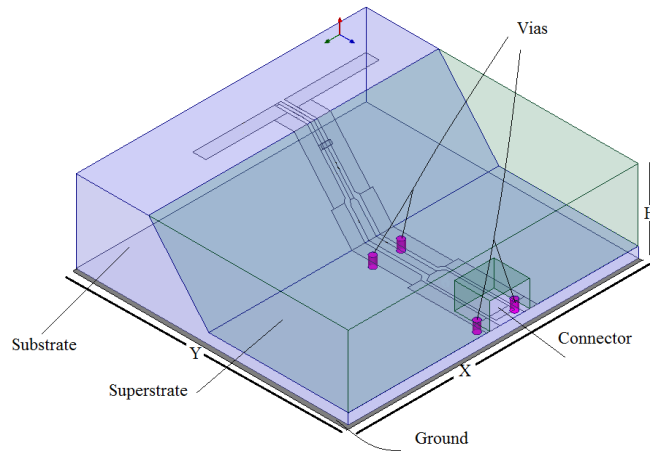


Figure 3.12: 3D 6 GHz antenna design.

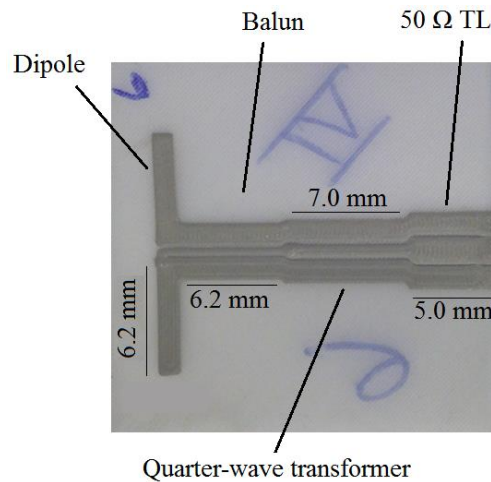


Figure 3.13: Dipole and feed network on the flexible ABS substrate.

Experimental results show excellent agreement between the measurement and the simulation, where the simulated and the measured S_{11} are less than -20 dB at the resonance frequency as shown in Figure 3.15. The antenna radiation pattern is shown in Figure 3.16, where

the maximum simulated and measured gains are 3.99 dBi and 3.95 dBi, respectively. The gain is reduced by ~ 1 dB due to the lower RF conductivity of the CB028 compared to its measured DC value of $\sim 1.5 \times 10^6$ S/m [13]. The manufactured antenna is shown in Figure 3.17.

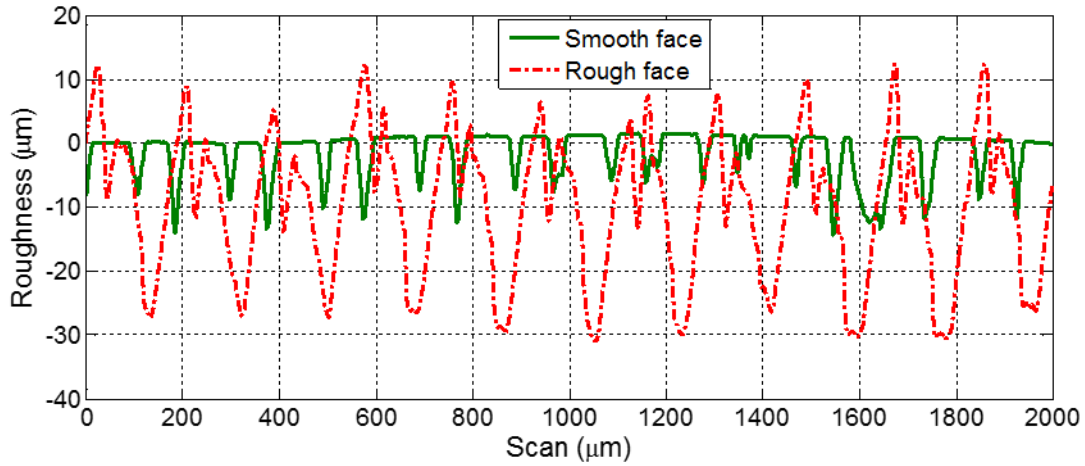


Figure 3.14: Profilometer scan.

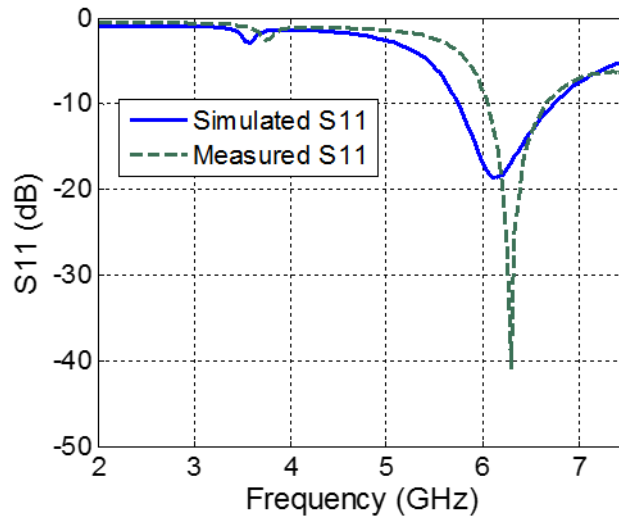


Figure 3.15: Measured and simulated S_{11} .

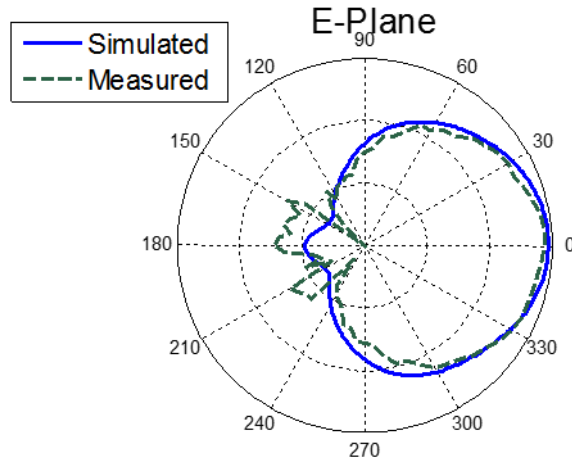


Figure 3.16: Measured and simulated normalized radiation pattern (10 dB/division).

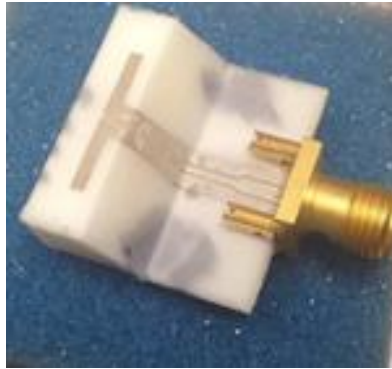


Figure 3.17: Manufactured 6.0 GHz antenna with superstrate removed to show the conformal circuitry.

3.4 Embedded 6 GHz 3D-Printed Half-Wave Dipole Antenna Array

3.4.1 Contribution

In this section, three-dimensional antenna elements are integrated into a non-planar 2x2 array configuration that is enabled by DDM. The 3D antenna elements, described in section 3.2 offer compact size and reduced surface wave loss compared to similar 2D ground-backed dipole antennas. The reason for this improved performance is that a thin substrate can be used for most of the signal distribution network to keep the (grounded) coplanar waveguide feedlines in close

proximity to the ground plane, until the feedlines are turned up a 45 degree, \sim quarter-wavelength long slope to connect to the dipole elements. The fabrication of this non-planar, 3D element is made possible by the use of DDM. The 2x2 array design expands on the 3D integration approach by orienting the elements along opposing, out-of-plane surfaces (Figure 3.18).

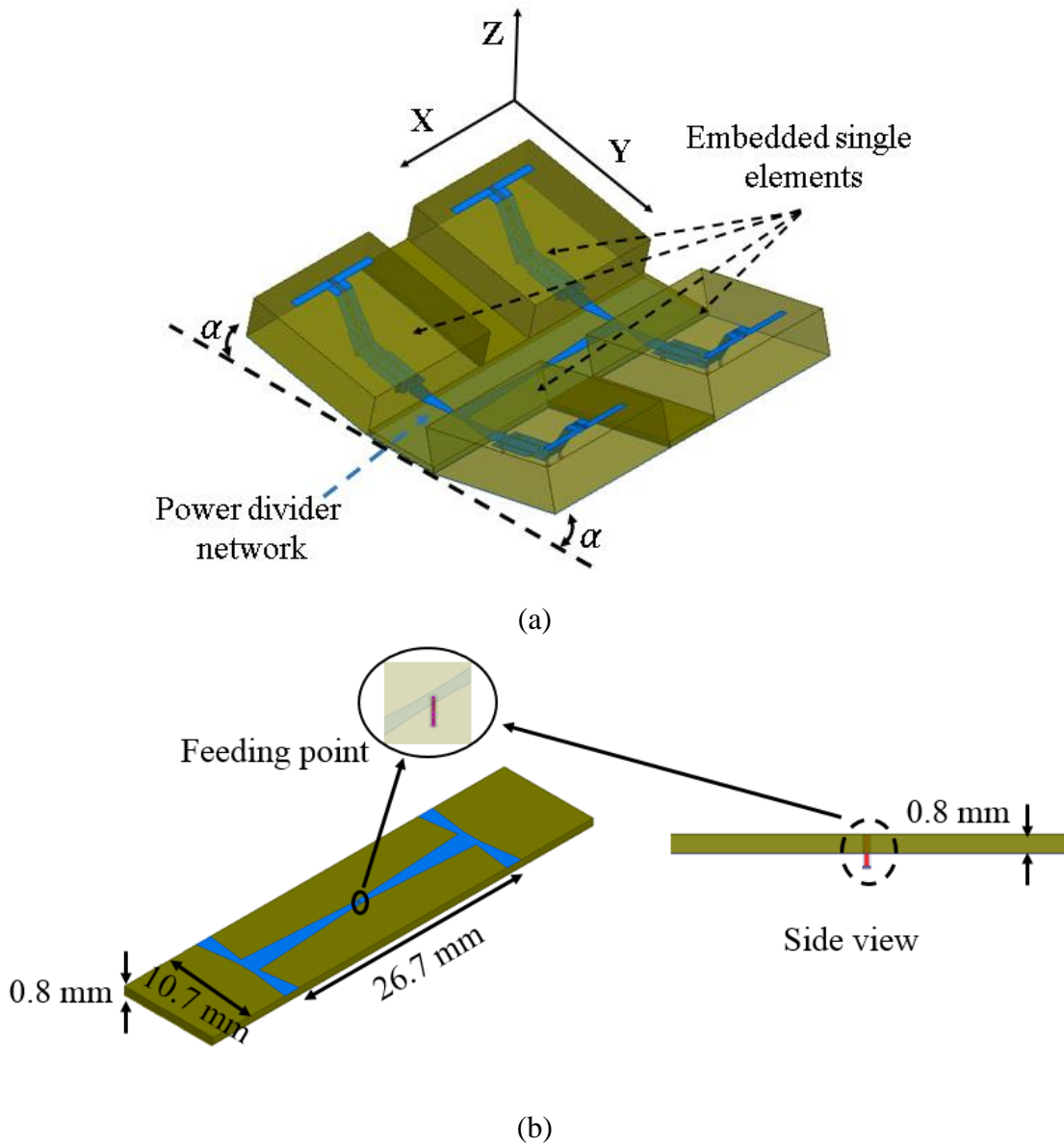


Figure 3.18: Array structure (a) Total structure (b) Feeding network.

The power splitters for the distribution network are located on a thin substrate in order to simplify ground connections, e.g. for a possible phase shifter or other electronics. More importantly, it is shown that the out-of-plane rotation of the antenna elements provides a convenient way to vary the element spacing – and thus the peak gain and beamwidth, without altering the signal distribution network. The gain varies from 8.5 dBi to 7 dBi as the rotation angle increases from 0 to 45 degrees. Changes in the array return loss occur with rotation, however the 10 dB return loss bandwidth is effectively maintained from 6-7 GHz.

3.4.2 Array Design, Fabrication and Performance

The 3D antenna element consists of a feedline, balun and half-wave dipole that are patterned on an Acrylonitrile Butadiene Styrene (ABS) substrate (relative permittivity of 2.7 and loss tangent of 0.008). The ABS is printed using fused deposition modeling (FDM) while the conductors consist of Dupont CB028 conductive paste that is deposited using micro-dispensing; the FDM and micro-dispensing processes are both done using an nScript 3Dn Tabletop printer. The dipole is fed through an inclined grounded coplanar waveguide (GCPW) balun that is matched to the 50 Ω feed line using a GCPW quarter-wave transformer as described in section 3.2. The single element is readily integrated into the 2x2 array configuration with out-of-plane panels as illustrated in Figure 3.18 (a). The input power is distributed to the elements via a tapered line power divider fed through a coaxial connector from the bottom (Figure 3.18 (b)). The feeding network ABS substrate is 0.8 mm thick, and both of the ground planes and power distribution transmission lines (TL) consist of micro-dispensed CB028 silver paste, with a minimum TL width of 0.6 mm. Finally, the microstrip feeding network is directly connected to the CPW-based antenna network.

The traditional approach for controlling the array radiation pattern is to change the element spacing along the y-axis. However for the array presented herein the minimum spacing is limited by the width of the power divider network (Figure 3.18 (b)). This limit is overcome by rotating the dipoles out-of-plane through an angle α to control the element-to-element spacing. In so doing the patterns of the ground-backed elements are no longer normal to the XY plane.

Figure 3.19 shows the simulated reflection coefficient (S_{11}) for different angles α . As well, Fig. 3 shows the simulated elevation plane ($\phi=0^\circ$) and azimuth plane ($\phi=90^\circ$) radiation patterns for different rotation angles (α). Simulations show that the array is well matched at the design frequency for the different angle arrangements. The beamwidth changes by changing the angle α , where the maximum 3 dB beamwidth for $\alpha=0$ degrees is 50° , and for $\alpha=45$ degrees is 70° (Figure 3.20). Furthermore, the design approach offers the ability to reduce the array footprint in the XY plane by exploiting the z-axis, where the array occupies $46 \times 52 \times 6.25 \text{ mm}^3$ and $46 \times 41 \times 19 \text{ mm}^3$ for $\alpha=0$ and 45 degrees, respectively, with a length reduction of 21%. The array simulations are carried out using HFSS full wave simulator.

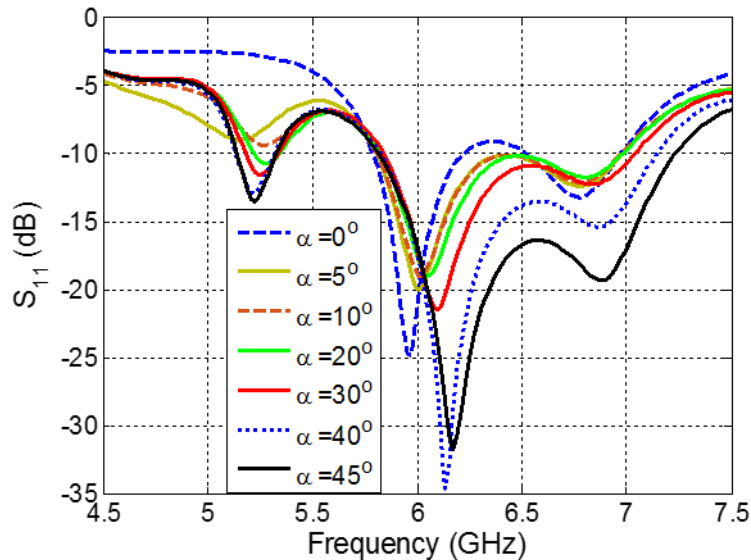


Figure 3.19: Simulated S_{11} for different rotation angles.

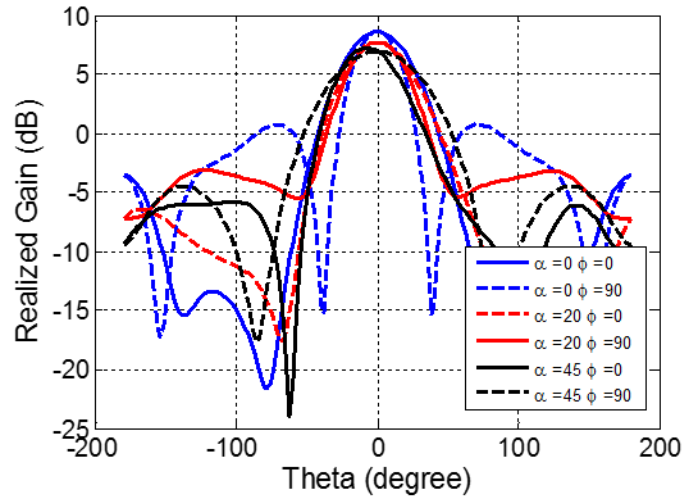


Figure 3.20: Array realized gain.

The 45° tilted array is fabricated to validate the design approach as shown in Figure 3.21, which presents the top view of the fabricated array, with and without the superstrate (the ABS part used to embed the elements). A 3D printed holder is used to carry the array structure. The simulated and measured S_{11} , as well as the simulated and measured realized gain are shown in Figure 3.22 and Figure 3.23, respectively. The S_{11} data are in excellent agreement at the design frequency (6.17 GHz) with a return loss greater than 30 dB. The measured S_{11} presents narrower bandwidth compared to the simulation, which could be due to the additional inductance that the connector pin adds at input. The simulated and measured patterns are in close agreement, where the maximum realized gain is 7 dBi.

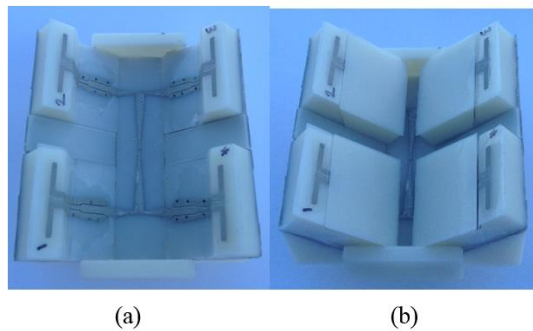


Figure 3.21: Fabricated array. (a) without the superstrate (b) embedded elements.

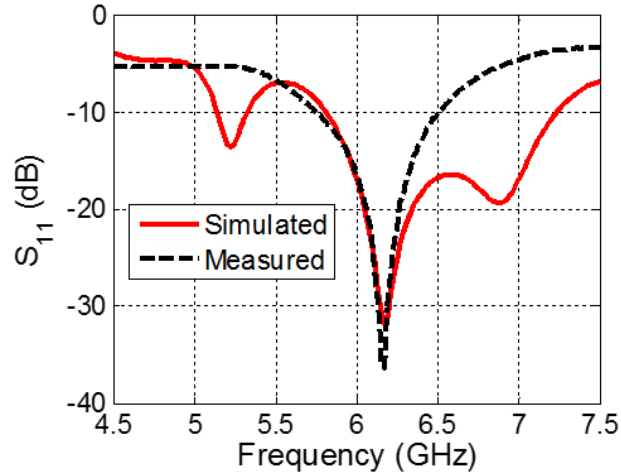


Figure 3.22: Simulated, and measured S_{11} .

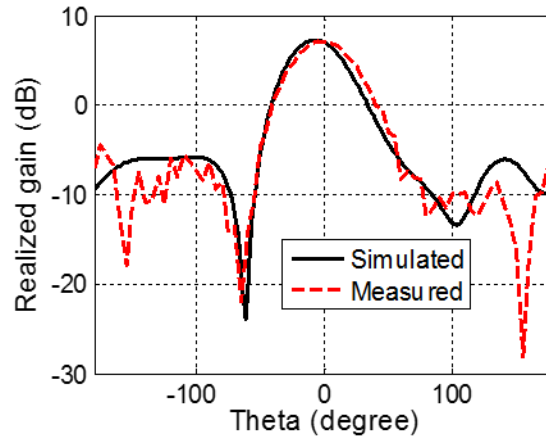


Figure 3.23: Simulated, and measured realized gain ($\phi=0^\circ$).

3.5 Conclusion

In this chapter, a three dimensional implementation of the half-wave dipole and an arrangement of 3D designed element in a 3D fashion to form a 2×2 array is introduced. The proposed 3D design improves performance on the single element level as well as the overall array performance by exploiting the single element advantages, and the advantages of placing them in a non-planar configuration. Additionally, the ability to reduce the footprint by using the 3rd dimension is demonstrated. Besides, a new process is proposed to facilitate the fabrication of three dimensional designs.

CHAPTER 4: HIGH-Q EVANESCENT-MODE CAVITY RESONATOR AND FILTER²

4.1 Introduction

The need for compact and highly selective filters for RF front-end applications has focused significant attention onto evanescent mode cavity resonators, since they are small in volume, offer high quality factor and have a large spurious-free region. These resonators are also excellent candidates for tunable filter designs, since the resonance frequency is extremely sensitive to the gap between the post and the cavity top wall, where a micrometer change in the gap has been shown to cause a frequency shift of 1.0 GHz or more. High quality factor tunable resonators can be achieved using various technologies such as Yttrium iron garnet (YIG), and microelectromechanical systems (MEMS). In this chapter, the first high-Q capacitively-loaded cavity resonators and filters that are compatible with direct print additive manufacturing as the combination of fused deposition modeling and micro-dispensing is presented.

4.2 High-Q Capacitively-Loaded Evanescent-Mode Cavity Resonator

In this section, the capacitively-loaded evanescent-mode cavity resonator is introduced, where the main resonator parameters are described. The single resonator is designed, fabricated and measured to investigate the performance of this type of resonators when DPAM is used as the fabrication process. The resonator preliminary performance is then enhanced by either modifying the resonator structure or by using lower loss material. As well, the effect of the low RF

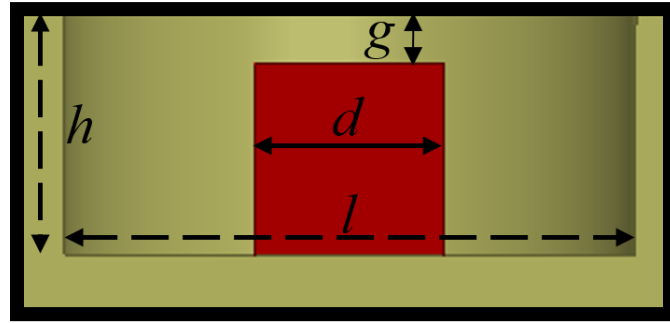
² The content of this chapter has been published in [91] and [92], and it is included in this dissertation with permission from the IEEE. Permission is included in Appendix A.

conductivity of the conductive paste that is used in the micro-dispensing process is also explored, which provides additional data that helps in enhancing the DPAM manufactured resonators.

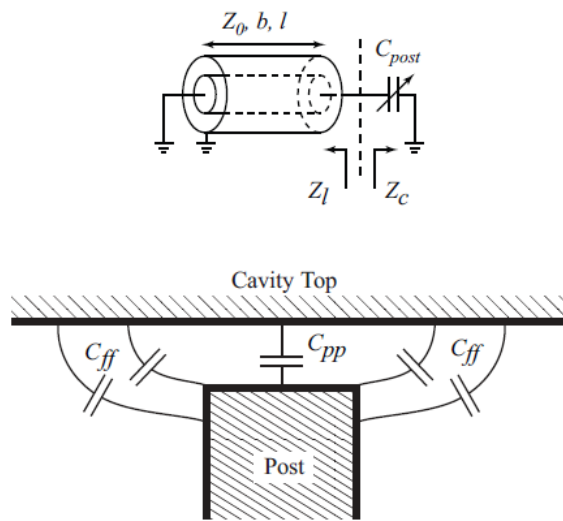
4.2.1 Direct Print Additively Manufactured S/C-Band High-Q Resonator

In this work, a capacitively-loaded evanescent-mode cavity resonator that is compatible with the DPAM 3D printing technique is described. The fabrication process is done using an nScript Tabletop 3Dn printer. The presented design is a compromise between quality factor, cost and manufacturing complexity and to the best of the authors' knowledge is the highest Q-factor resonator demonstrated to date using DPAM-compatible materials and processes. The topology is based on the resonator originally fabricated in printed circuit board form by Gong, et al. [53]. Micromachining is not required, and the need for vias to connect top and bottom cavity walls is eliminated by using instead a solid exterior wall that is coated with conductive paste. Finally, the proposed resonator is an excellent base for a tunable filter, where a thin cavity top wall can be easily printed to form a flexible membrane that can be moved up and down to tune the operating frequency.

The capacitively-loaded cavity structure is shown in Figure 4.1, where the cavity size (l and h), post diameter (d), and the gap (g) between the post and the cavity top wall are the main parameters controlling the resonance frequency. Based on the model developed in [73], the resonance results from the area above the post that can be modeled by a lumped capacitor, assuming a uniform electric field exists between the top of the post and the cavity, and the inductance derived from treating the cavity and post as a coaxial line that is shorted at its base.



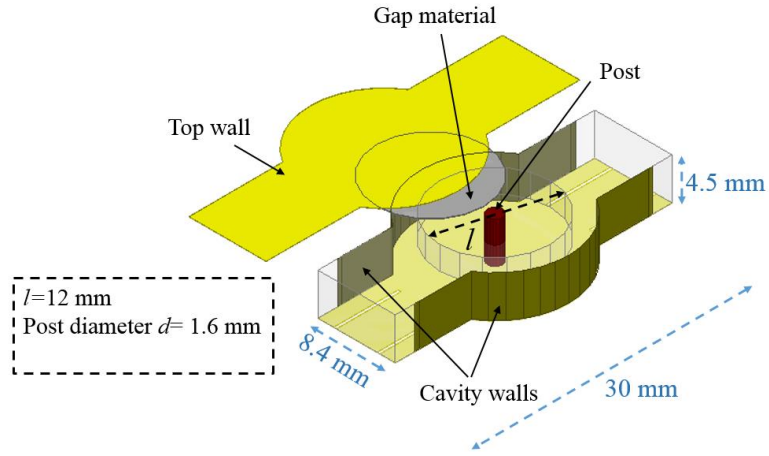
(a)



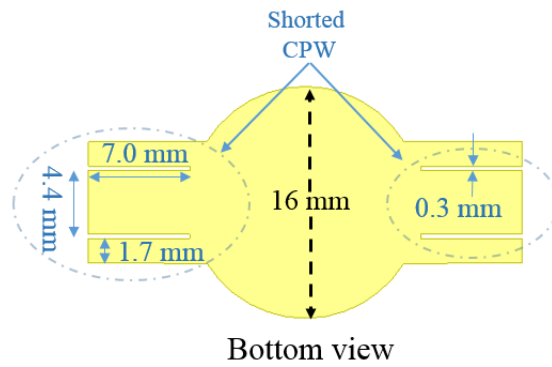
(b)

Figure 4.1: Evanescent-mode cavity resonator. (gap filling material is not shown here) (a) cavity resonator (b) model for the capacitively-loaded cavity resonator [73] 2010 ©IEEE.

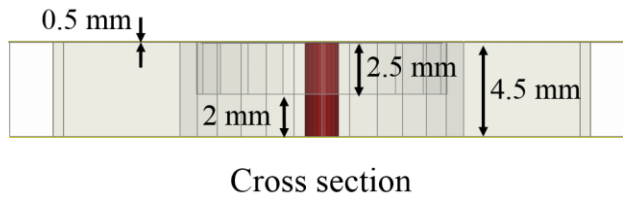
The resonance frequency can be found by equating the modeled capacitor and inductor impedances. The capacitance can be changed either by changing the post diameter or the gap size, which are key parameters in designing the evanescent-mode cavity resonator. The proposed evanescent-mode resonator (Figure 4. 2), consists of the 3D printed substrate (ABS), shorted input and output coplanar waveguide (CPW) feedlines, sidewalls, the post and the cavity top wall.



(a)



(b)



(c)

Figure 4.2: Evanescent-mode resonator structure.

The gap height and the post diameter are selected to be 30 μm and 1.6 mm such that the resonance frequency is 2.30 GHz . Furthermore, to improve the design reliability and stability, the gap is filled with a low loss, liquid crystal polymer (LCP) material (ULTRALAM 3908 with relative permittivity of 2.9 and loss tangent of 0.0025), since the gap size is very small. The fabrication

process, shown in Figure 4.3, starts with printing the cavity structure (i.e., the ABS) using fused deposition modeling (FDM), and then creating the cavity conductive walls by brushing Dupont CB028 silver paste and curing it at 90 C° for 60 minutes (bulk DC conductivity of 1.5×10^6 S/m), as well as including the post (a 1.6 mm diameter copper wire). In the next step, the shorted input and output CPW feed lines are implemented using a pulsed picosecond laser to cut slots in the CB028. Finally, the top wall (a 0.5 mm thick ABS brush-coated by CB028 paste) and the gap material are prepared. The assembly is carried out by adhering the top wall (Figure 4.3 (c)) with the CB028 coated ABS (Figure 4.3 (b)), and including the coaxial connectors. The assembled capacitively-loaded cavity resonator is shown in Figure 4.3 (d). The CB028 coating process is fully compatible with micro-dispensing, however manual brushing was used for expediency in the first prototypes.

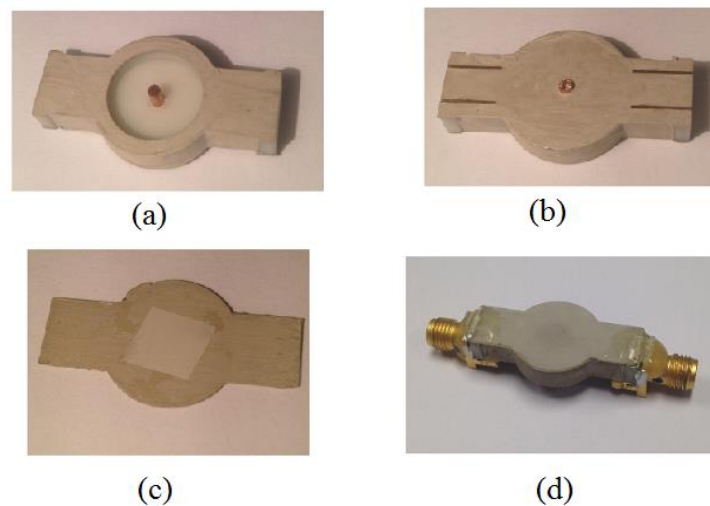


Figure 4.3: Evanescent-mode cavity resonator fabrication process. (a) print the cavity structure, coat the cavity walls with conductive paste, and include the post (b) form the input and output shorted CPW feedlines using laser milling of CB028 (c) prepare the top cavity wall along with the LCP insulator layer (d) final assembly.

The RF measurements of the fabricated resonator are taken with an Agilent Technologies PNA network analyzer N5227A. The simulated and measured unloaded quality factor are 170 and 107 respectively, where the simulated and measured S_{21} are in very good agreement as shown in Figure 4.4. The device under measurement is shown in Figure 4.5. The tunability of the resonator is examined by changing the gap g in a controllable manner by withdrawing the copper post to increase the gap height and reduce the capacitance. Figure 4.6 shows a set of measured responses for different gap heights, where the frequency can be changed from 2.3 GHz to 7 GHz. The corresponding gaps and unloaded quality factors are shown in Figure 4.7, where the quality factor variation versus gap height (right Y-axis) is consistent with the HFSS simulations. The gap heights are extracted from HFSS simulation by introducing an air gap between the post and LCP layer, and matching the simulation to measurements.

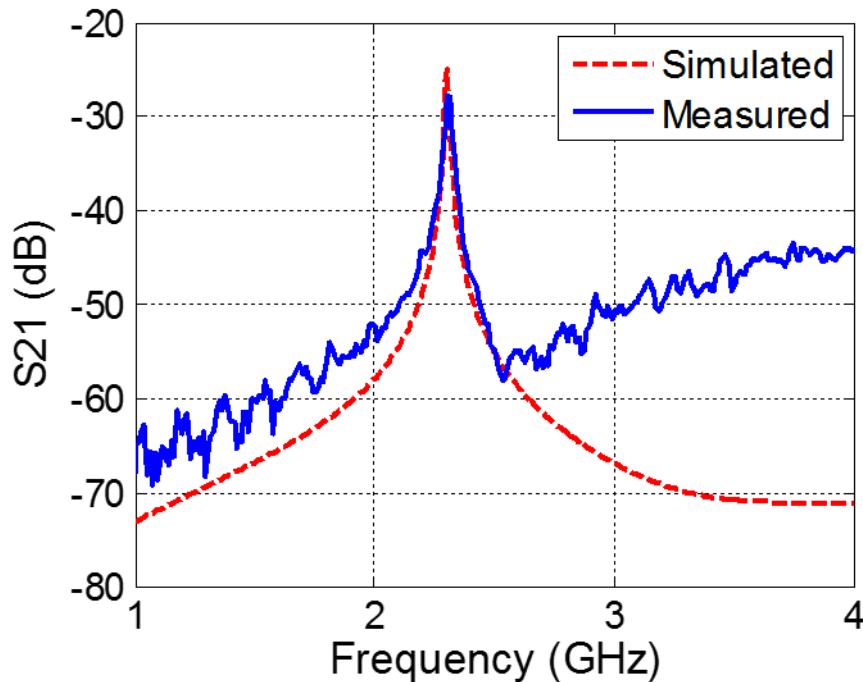


Figure 4.4: Single resonator simulated vs. measured S_{21} .

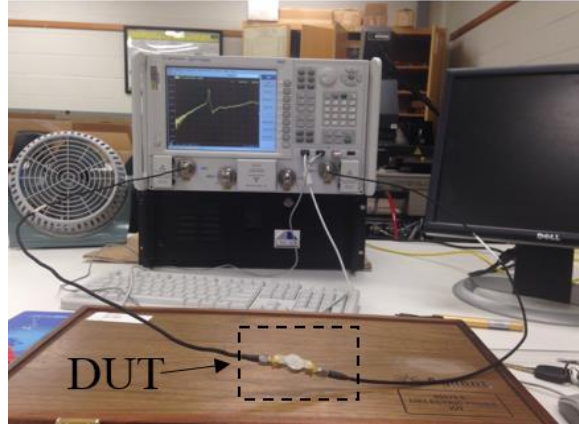


Figure 4.5: Device under test.

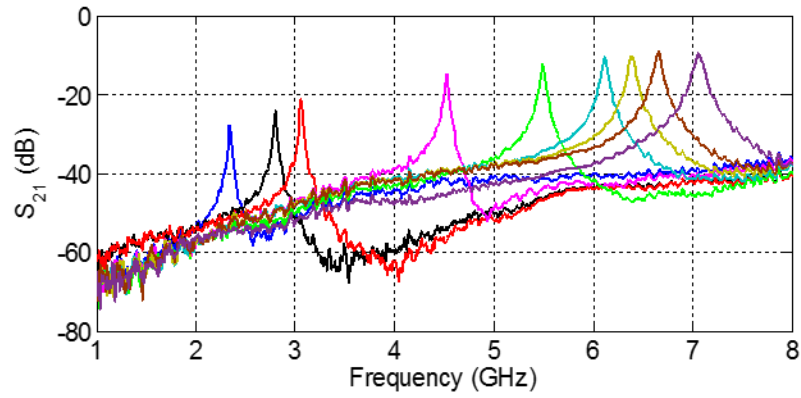


Figure 4.6: Measured S_{21} for different gap settings.

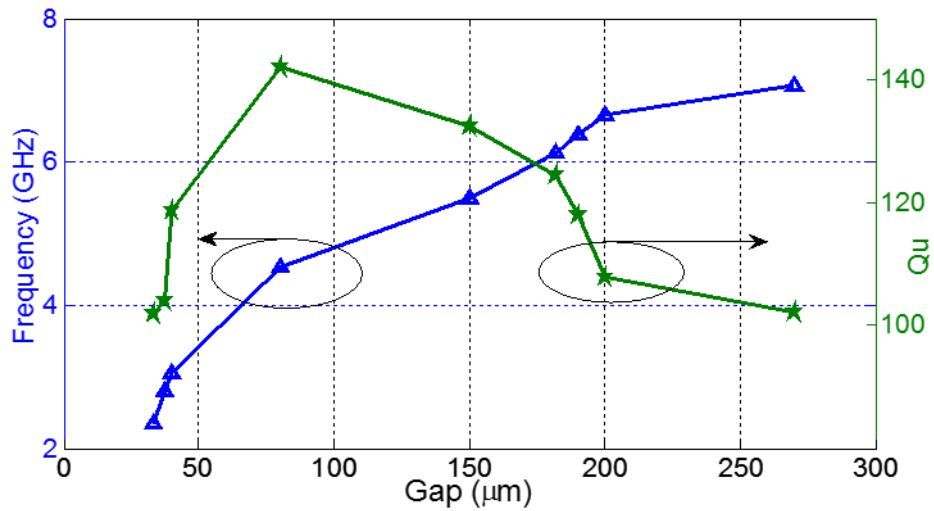


Figure 4.7: Gap changes vs. resonance frequency and corresponding unloaded quality factor.

4.2.2 Enhanced Performance Capacitively-loaded Cavity Resonator

As described in section 4.2.1, the cylindrical capacitively-loaded cavity structure is shown in Figure 4.8, where the cavity height ($h+d$), cavity radius (l), post radius (r), and the gap (g) between the top of the post and the cavity top wall are the main parameters defining the resonator performance. Tunability, as described in section 4.2, can be enabled once the structure dimensions are set by changing the gap, where differences of a few microns can change the frequency by a GHz. In this section, the resonator's unloaded quality factor has been enhanced adopting two approaches: (a) reducing the resonator opening near the feedlines (b) adopting a new approach and using lower loss material to control the resonator capacitance. Firstly, compared to the resonator design in section 4.2, the quality factor is increased by up to 2X by reducing the opening by 64.3% near the feedlines (see Figure 4.9). This improvement in the quality factor is critical in achieving the low insertion loss and steep cut-off observed with the two-pole filter.

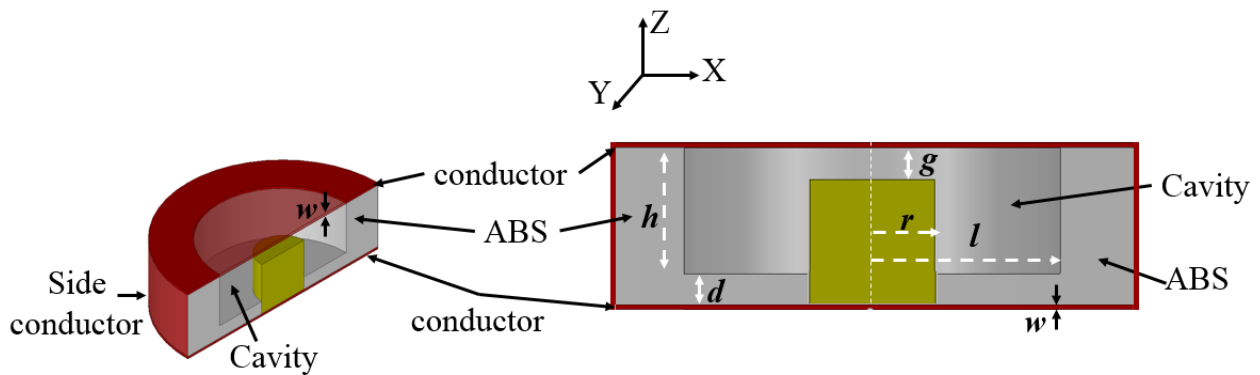


Figure 4.8: Side-view of the capacitively-loaded cavity resonator. (gap filling material is not shown here).

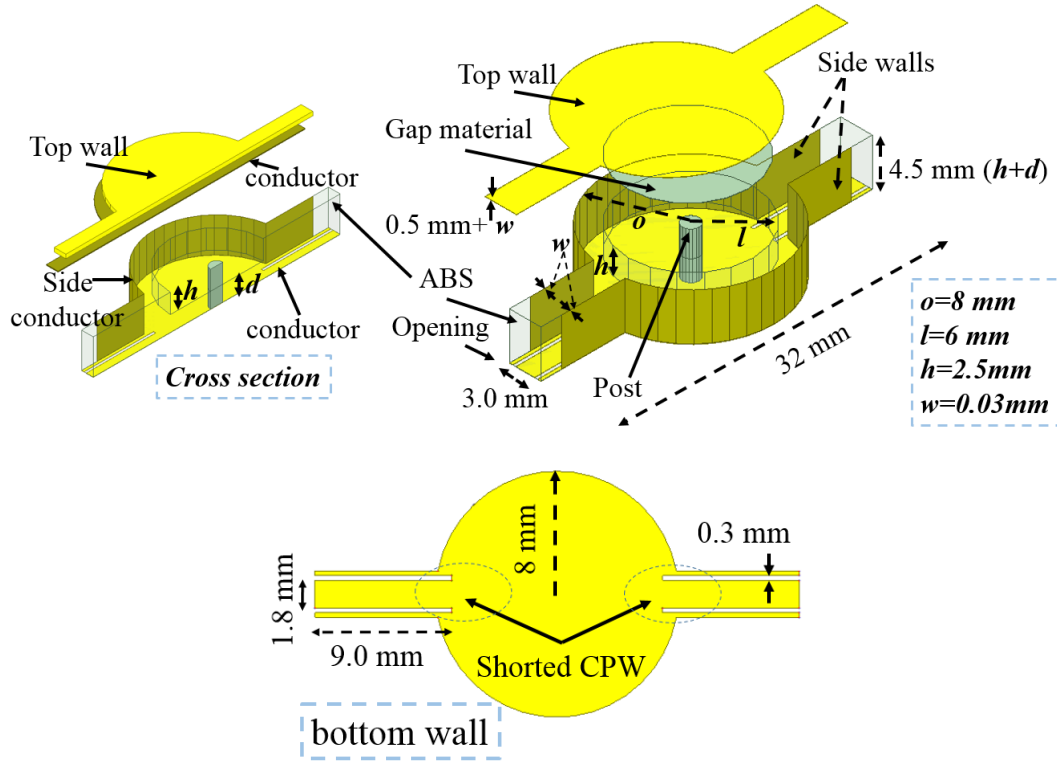


Figure 4.9: 3D view of the single capacitively-loaded cavity resonator.

The evanescent-mode resonator (Figure 4.9) consists of the FDM ABS substrate coated with Dupont CB028 silver paste. In this work the CB028 has been applied to the outer surfaces of the cavity bottom and side walls, the underside of the cavity top wall, and the feed section using a brush, although either the micro-dispensing or micro-spraying attachments available on the nScript printer could be used. The paste is dried at 90 °C for 60 minutes, achieving a bulk DC conductivity of 1.5×10^6 S/m. The shorted input and output coplanar waveguide (CPW) feedlines are laser machined using a 1064 nm pulsed picosecond laser, and a copper wire is used for the resonator post. Finally, the gap is filled with a low loss, liquid crystal polymer (LCP) material (ULTRALAM 3908 with relative permittivity of 2.9 and loss tangent of 0.0025). The measured thickness of the ULTRALAM gap material is 30 μ m, although the vendor-provided value is 25

μm ; the measured value is used in the design simulations. In the current process flow, the top piece of the cavity is made separately and coated with the CB028, the gap material is attached to the non-dried CB028, and the piece is then assembled to the lower portion of the cavity. The assembled unit is then dried as described above. The main challenge to making this a single, continuous printing process that does not require post-assembly is controlling the thickness of the gap material. Improvements in laser-thinning and micro-milling procedures should provide the required level of thickness control in the near future. Figure 4.10 shows the measured S_{21} for different gap settings, where LCP material is used to fill the gap. Figure 4.11 shows the measured unloaded quality factor and resonance frequency versus the gap dimension, within the frequency range from 2.4 to 6.8 GHz. The gap varies between $30\ \mu\text{m}$ at 2.4 GHz and $200\ \mu\text{m}$ at 6.8 GHz and is controlled using a micro-positioner stage. Gap heights are extracted from a full-wave simulation by introducing an air gap between the post and ULTALAM layer, and matching the measurement data to the simulation results.

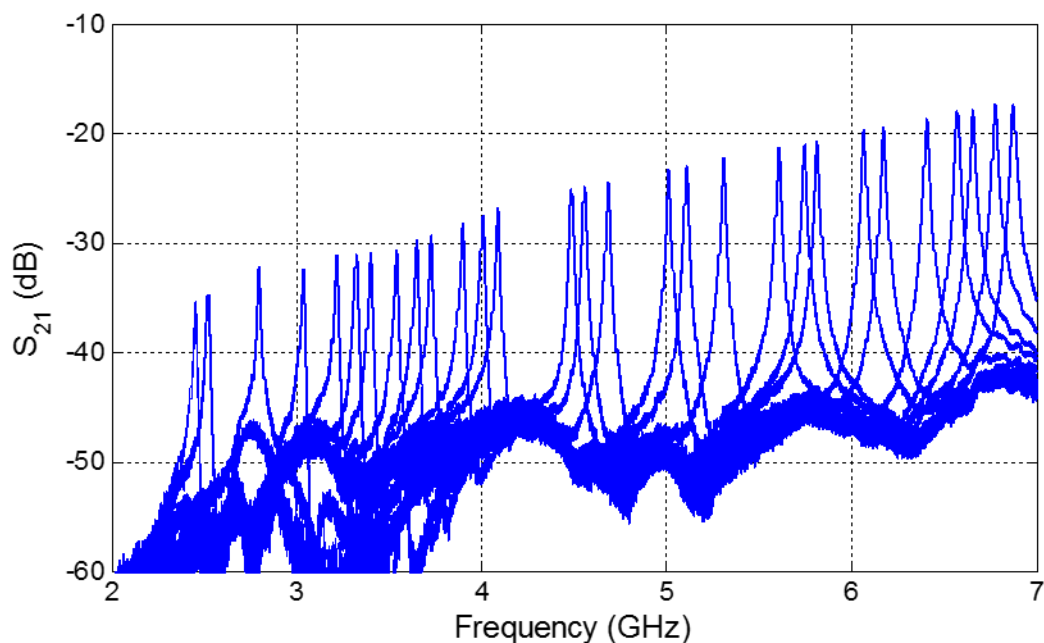


Figure 4.10: Enhanced resonator measured S_{21} for different gap settings (LCP gap material).

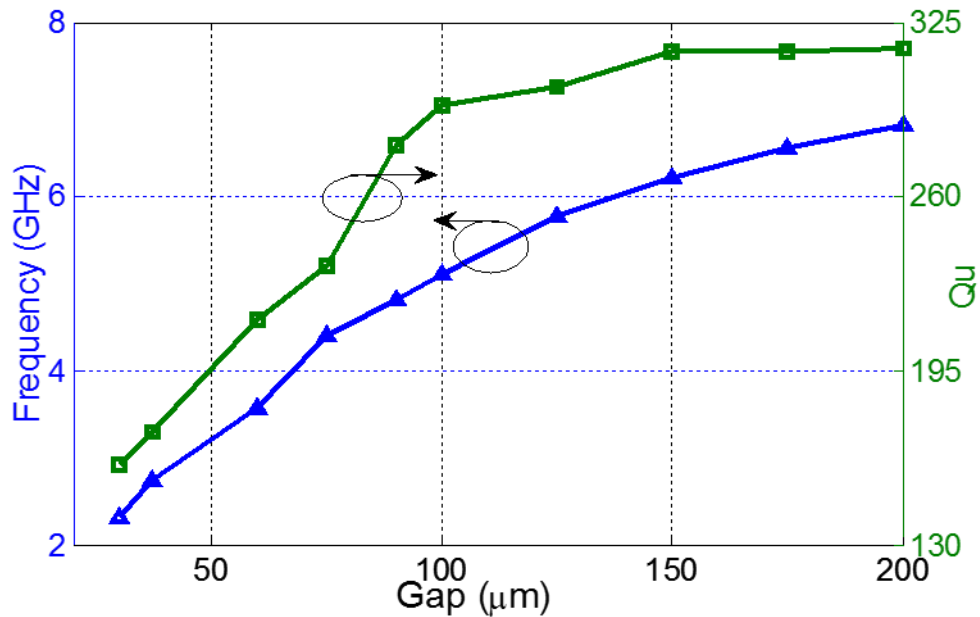


Figure 4.11: Gap variation vs. resonance frequency and corresponding unloaded quality factor (LCP gap material).

The second approach to enhance the quality factor is to replace the LCP (ULTRALAM 3908) material with lower loss material, where the gap filling step can be achieved by coating the post with a low loss Parylene type-N, as shown in Figure 4.12, (with relative permittivity of 2.4 and loss tangent of 0.0006) material [74]. Furthermore, using the Parylene provides the ability to go lower in frequency, where 1.0 μm layer is possible. Simulation shows that using a 3.0 μm Parylene layer for the same resonator shown in Figure 4.9, a resonance frequency of 0.63 GHz, and unloaded quality factor of 171 is possible. In this work, the measured thickness of the Parylene type-N material is 8 μm , and the measured value is used in the design simulations. Figure 4.13 shows the measured S_{21} vs. frequency of the single capacitively-loaded cavity resonator for different gap settings vary between 15 μm to 200 μm , where the gap is the 8.0 μm Parylene layer thickness plus the air gap results from moving the post toward the negative z-direction.

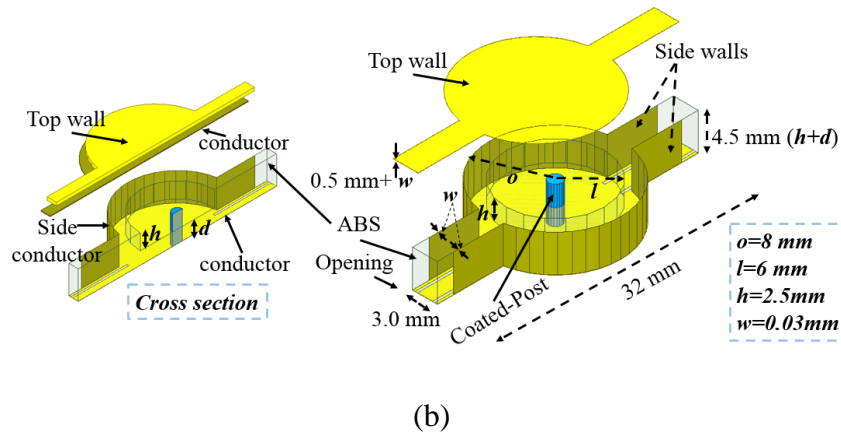
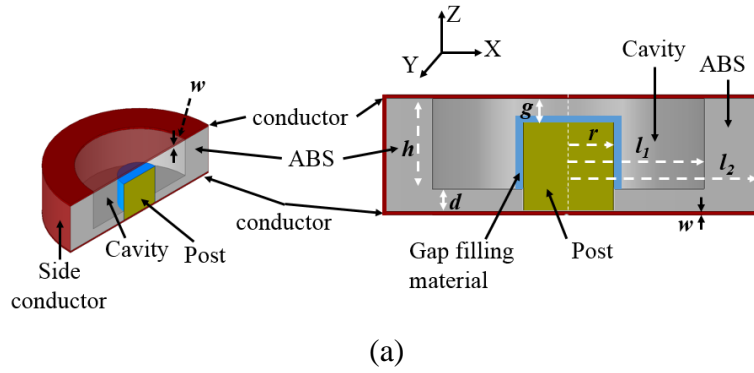


Figure 4.12: Single resonator with Parylene coated post. (a) Side-view of the capacitively-loaded cavity (b) 3D view of the single capacitively-loaded cavity resonator.

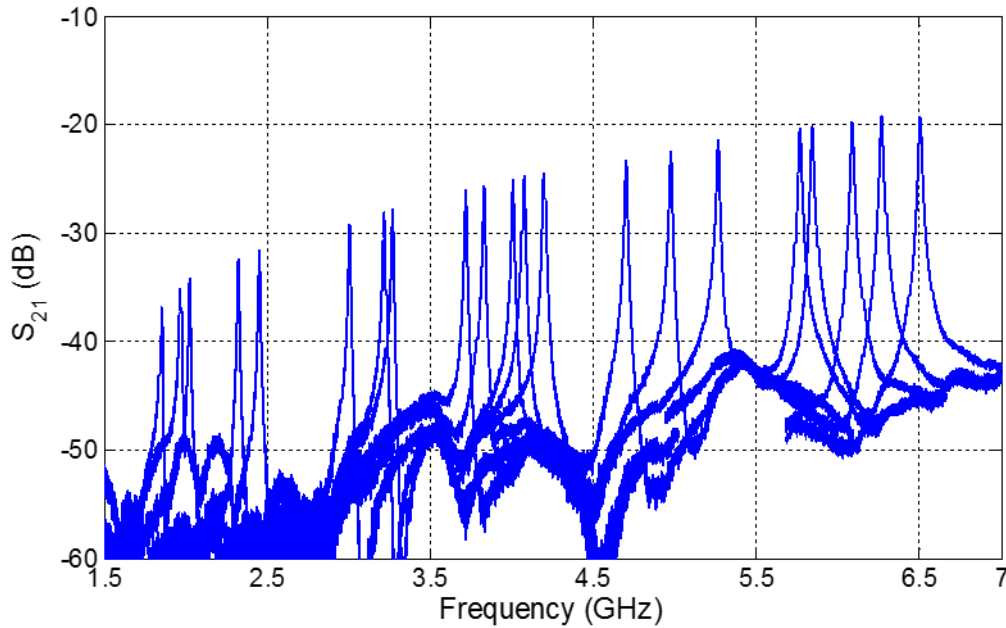


Figure 4.13: Enhanced resonator measured S_{21} for different gap settings (Parylene gap material).

The fabricated capacitively-loaded cavity resonator is shown in Figure 4.14, where the same resonator is used for both cases; LCP and Parylene gap filling material to have an accurate comparison and avoid discrepancies result from the fabrication process. The resonator under test is shown in Figure 4.15.

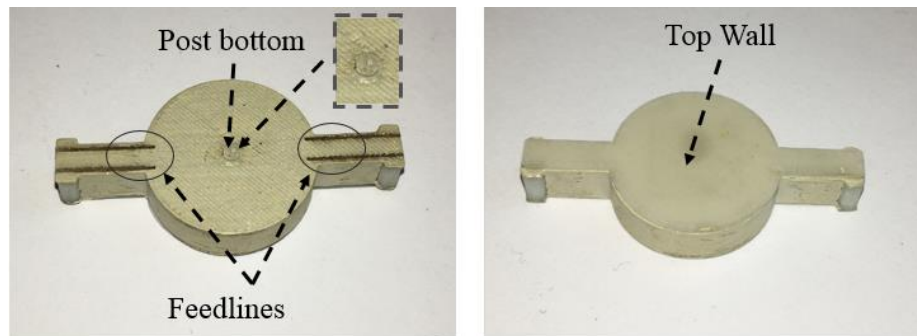


Figure 4.14: Fabricated capacitively-loaded cavity resonator.

Figure 4.16 shows the measured unloaded quality factor and resonance frequency versus the gap dimension, within the frequency range from 2.4 to 6.8 GHz. The gap varies between 30 μm at 2.4 GHz and 200 μm at 6.8 GHz and is controlled using a micro-positioner stage. Gap heights are extracted from a full-wave simulation by introducing an air gap between the post and ULTALAM layer, and matching the measurement data to the simulation results.

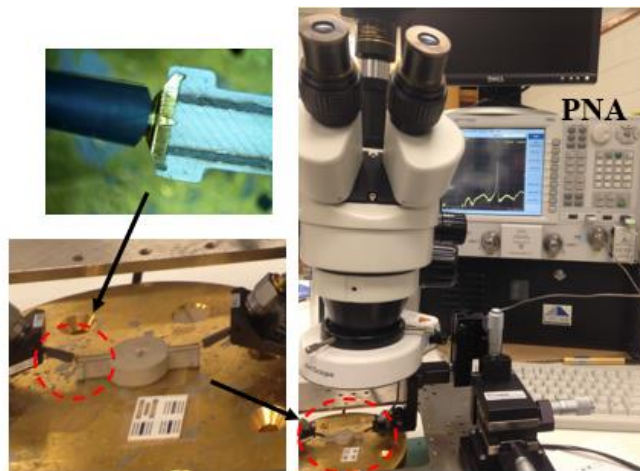


Figure 4.15: Single resonator under test.

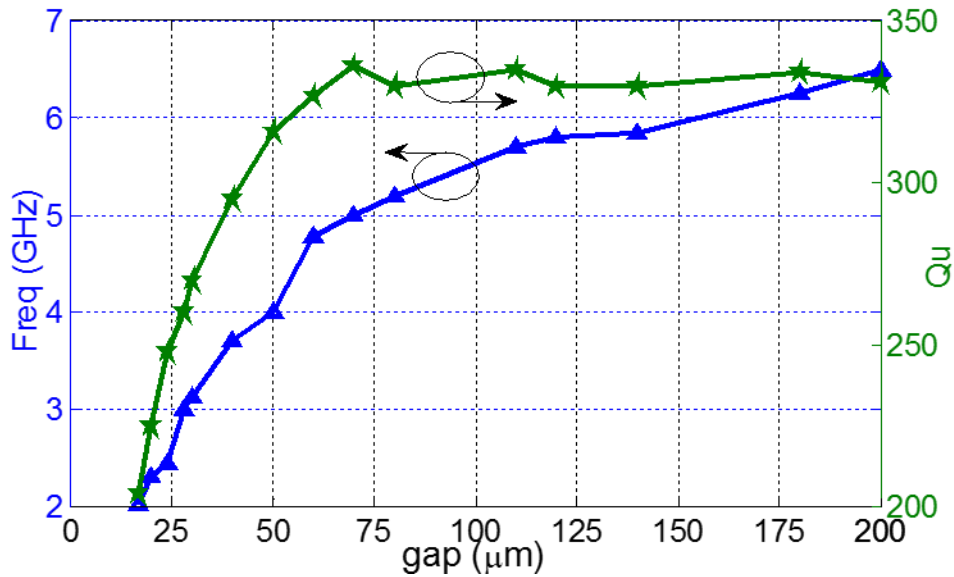


Figure 4.16: Gap variation vs. resonance frequency and corresponding unloaded quality factor (Parylene gap material).

By using the Parylene type-N, compared to the ULTRALAM, the unloaded quality factor (Q_u) is increased by up to 54% as shown in Figure 4.17. As mentioned previously, improvement in the quality factor is critical to achieving the low insertion loss and steep cut-off observed with the two-pole filter. To understand the conductivity effect on the DPAM cavity resonator's unloaded quality factor, the side, top, and bottom conductive parts of the resonator are replaced by copper (bulk DC conductivity of 5.8×10^7 S/m) and simulated using ANSYS Electronics Desktop full-wave simulator. This study provides an excellent way to understand the differences in the unloaded quality factor between the MEMS and DPAM resonators, as well as explains what parameters need to be changed/modified in order to enhance the DPAM resonator's quality factor; such as plating the resonator or using pastes with higher conductivity. Table 4.1 presents the DPAM resonator unloaded quality factor at 2.3 GHz when the CB028 is replaced by copper, for different gap filling materials. The effects of replacing each conductor (i.e., side, top, and bottom wall) by copper, as well as using the LCP and Parylene as gap filling materials are described. From

the analysis, increasing the conductivity of the top and bottom walls dominates the quality factor increment, compared to increasing the conductivity of the side walls. As well, it is illustrated that presence of the gap filling material has a big effect on the unloaded quality factor, specially for the LCP case. Finally, the dependence of the resonance frequency and Q_u on cavity height is illustrated in Figure 4.18.

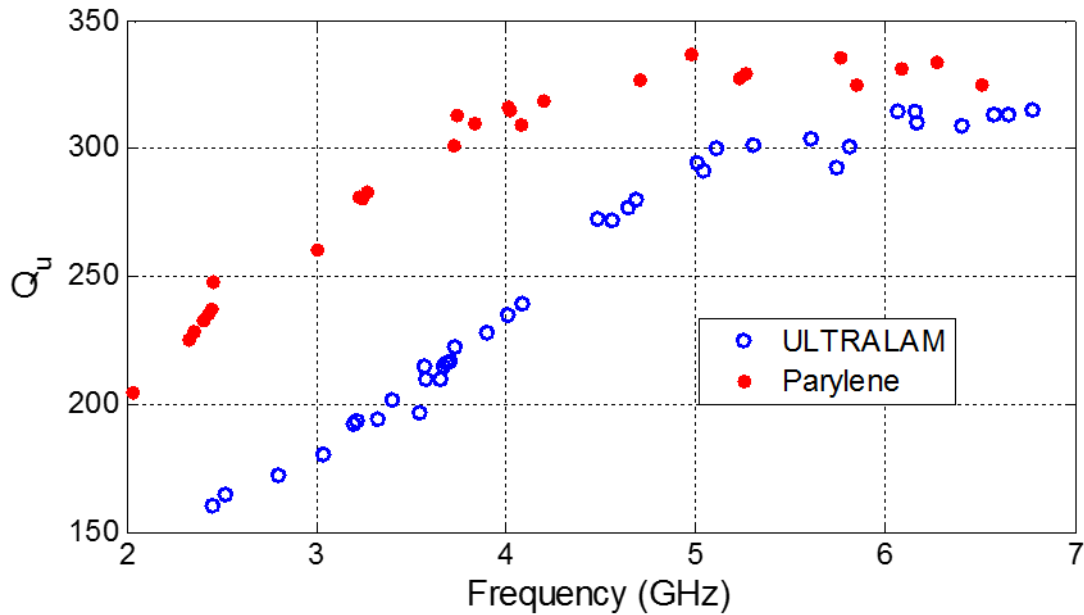


Figure 4.17: Unloaded quality factor of the single capacitively-loaded cavity resonator for different gap material, and different gap settings.

Table 4.1: Cavity conductive parts and conductive materials vs. the unloaded quality factor at 2.3 GHz.

Side wall	Bottom	Top	Q_u (LCP)	Q_u (Parylene)
CB028	CB028	CB028	225	365
<i>Copper</i>	CB028	CB028	245	403
CB028	CB028	<i>Copper</i>	274	500
CB028	<i>Copper</i>	CB028	280	510
<i>Copper</i>	CB028	<i>Copper</i>	295	561
<i>Copper</i>	<i>Copper</i>	CB028	299	575
CB028	<i>Copper</i>	<i>Copper</i>	347	793
<i>Copper</i>	<i>Copper</i>	<i>Copper</i>	375	900
<i>Copper</i>	<i>Copper</i>	<i>Copper</i>	1050*	1050*

* No gap material

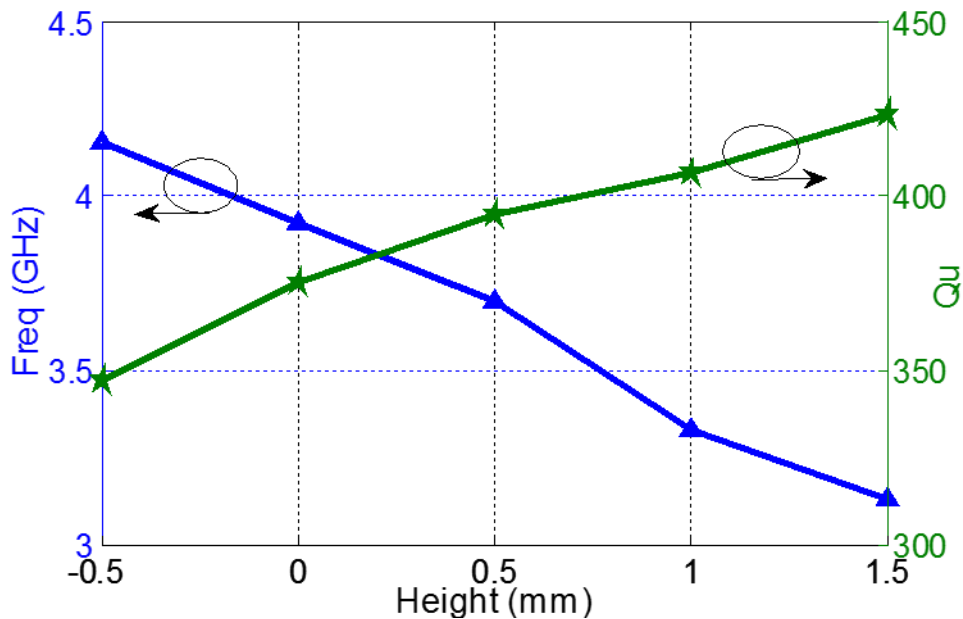


Figure 4.18: The effect of changing the cavity height relative to the baseline design parameter (4.5 mm) at gap size of $60 \mu\text{m}$.

4.3 Direct Print Additively Manufactured Capacitively-Loaded Band-Pass Filter

4.3.1 Introduction

Today's demanding technologies forces the filter community to keep developing and updating the existing highly selective filters as they are key components to enable efficient usage of the crowded electromagnetic spectrum. As emphasized in the chapter 1, among the available filter architectures, capacitively-loaded approaches have received significant attention since they offer high quality factors, a large spurious-free region, compact volume, and they can be made tunable. There are several papers that present the use of microelectromechanical systems (MEMS) to design capacitively-loaded cavity resonators and filters. As reported in [55], MEMS technology succeeded in achieving a measured unloaded quality factor (Q_u) of 460 – 530 in the frequency range extending from 3.4 – 6.2 GHz. As well, narrow band, tunable MEMS band-pass filters of 0.7% and 2% are reported in [56], and [73] to have an insertion loss of up to 3.55 dB and 1.65 dB

at 3.06 GHz and 2.4 GHz, respectively. In this section two proposed architectures that are compatible with DPAM are introduced; (a) Lateral-coupled filter and (b) Vertically stacked coupled filter.

4.3.2 Synthesis of Coupled Resonator Filter

Coupled-resonator theory represents a solid base in designing RF coupled-resonator filters, as it is based on the analysis of the equivalent circuit of coupled resonators, regardless the resonator structure as described in [75]. According to J.-S Hong et al. [75], it has been applied to a broad array of filter structures such as waveguide filters [76], and [77], microstrip filters [78-80], ceramic filters [81], dielectric resonator filters [82], MEMS filters [83], and superconducting filters [84]. Figure 4.19 shows the equivalent circuit of n -coupled resonators, where the e_s is the source, R is the resistance, as well as the L and C are the inductance and capacitance respectively. Adopting either the loop equation analysis, or the node equation analysis leads to the same results.

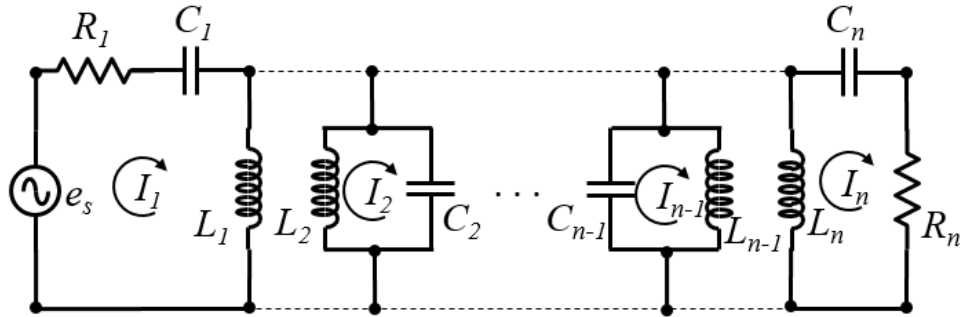


Figure 4.19: Equivalent circuit of n -coupled resonators.

The filter response depends on both the external quality factor (Q_e) and the coupling coefficient between the resonators (k). To derive a relationship between these parameters and the filter physical structure, the voltage-current relationship of the equivalent circuit of n -coupled resonator can be expressed using Kirchhoff's law as [75]:

$$[Z] \cdot [i] = [e] \quad (4.1)$$

$$\begin{bmatrix} R_1 + j\omega L_1 + \frac{1}{j\omega C_1} & j\omega L_{12} & \cdots & j\omega L_{1n} \\ j\omega L_{21} & j\omega L_2 + \frac{1}{j\omega C_2} & \cdots & j\omega L_{2n} \\ \vdots & \vdots & \ddots & \vdots \\ j\omega L_{n1} & j\omega L_{n2} & \cdots & R_n + j\omega L_n + \frac{1}{j\omega C_n} \end{bmatrix} \begin{bmatrix} i_1 \\ i_2 \\ \vdots \\ i_n \end{bmatrix} = \begin{bmatrix} e_s \\ 0 \\ \vdots \\ 0 \end{bmatrix} \quad (4.2)$$

where $L_{ij} = L_{ji}$ is the mutual inductance between the i^{th} and j^{th} resonators. The impedance matrix can be simplified for synchronous resonance case (i.e., $L = L_1 = \dots = L_n$ and $C = C_1 = \dots = C_n$) as follow:

$$[\bar{Z}] = \begin{bmatrix} p + \frac{1}{q_{e1}} & -jk_{12} & \cdots & -jk_{1n} \\ -jk_{21} & p & \cdots & -jk_{2n} \\ \vdots & \vdots & \ddots & \vdots \\ -jk_{n1} & -jk_{n2} & \cdots & p + \frac{1}{q_{en}} \end{bmatrix} \quad (4.3)$$

where p , k_{ij} , and q_e are the complex low-pass frequency variable, the normalized coupling coefficient between the i^{th} and j^{th} resonators, and scaled external quality factor respectively, which can be expressed as follows:

$$p = j \frac{1}{FBW} \left(\frac{\omega}{\omega_0} - \frac{\omega_0}{\omega} \right) \quad (4.4)$$

$$m_{21} = \frac{L_{ij}/L}{FBW} \quad (4.5)$$

$$\frac{FBW}{q_{ei}} = \frac{R_i}{\omega_0 L} \quad (4.6)$$

where $FBW(\Delta)$ is the fractional bandwidth which express as:

$$FBW = \frac{\Delta\omega}{\omega_0} \quad (4.7)$$

As mentioned above, either loop or node analysis gives the same results, which leads into a generalized solution as follow:

$$S_{21} = 2 \frac{1}{\sqrt{q_{e1}q_{en}}} [A]_{n1}^{-1} \quad (4.8)$$

$$S_{11} = \pm \left(1 - 2 \frac{1}{q_{e1}} [A]_{11}^{-1} \right) \quad (4.9)$$

The matrix [A] can be expressed as:

$$[A] = [q] + p[U] - j[k] \quad (4.10)$$

with [q] is an $n \times n$ matrix having $q_{11}=1/q_{e1}$ and $q_{nn}=1/q_{en}$ and all other entries of zeros, [U] is $n \times n$ identity matrix, and [k] is the general coupling matrix.

RF/microwave filters are commonly designed using the low- pass prototype network such as Butterworth, Chebyshev, elliptic, etc. The element values of these low-pass prototype network can be used as initial values in the design procedure. Hence, the filter can be synthesized by optimizing any objective function that represents the filter response by taking the theoretical values of the Q_e and k as its initial values. The external quality factor and internal coupling coefficient can be calculated from the low-pass prototype tabulated values as follow [75]:

$$Q_e = \frac{g_0 g_1}{\Delta} \quad (4.11)$$

$$k = \frac{\Delta}{\sqrt{g_1 g_2}} \quad (4.12)$$

As well, internal coupling (k) can be extracted from the simulated/measured s-parameters as follow:

$$k = \frac{f_{p2}^2 - f_{p1}^2}{f_{p2}^2 + f_{p1}^2} \quad (4.13)$$

where f_{p2} and f_{p1} refer to the resonance frequencies that result either from magnetic or electric coupling as shown in Figure. 4.20. S_{21}

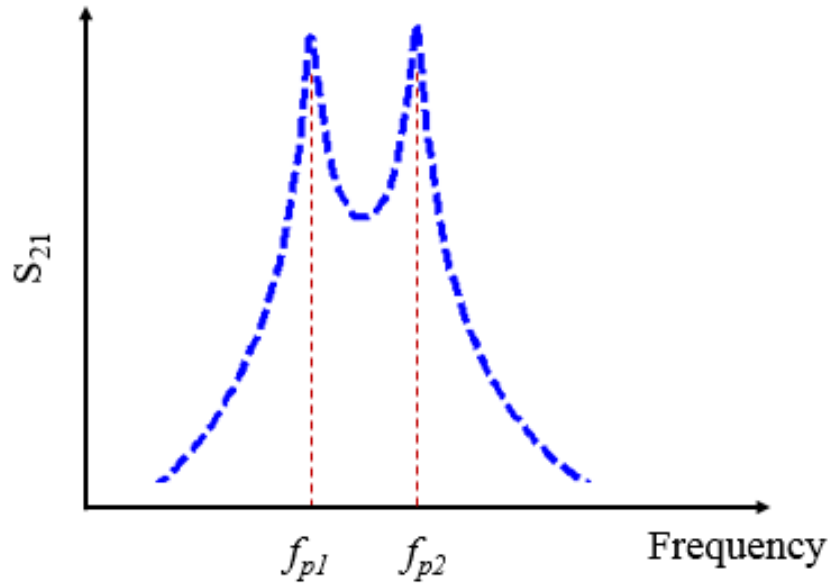


Figure 4.20: S_{21} of two coupled resonators.

4.3.3 Direct Print Additively Manufactured Laterally-Coupled Band-Pass Filter

In this section, a laterally-coupled 2.4 GHz band-pass filter is developed using DPAM fabrication process to represent the first capacitively-loaded cavity band pass filter that is compatible this hybrid technique that combines fused deposition modeling and micro-dispensing. Using the developed resonator in section 4.2.2, that uses the LCP material as the gap filling material and achieves a measured unloaded quality factor of 160-320 over the frequency range 2.4-6.8 GHz, a two-pole, 1.9% fractional bandwidth (Δ) Butterworth filter is synthesized at 2.44 GHz adopting the coupled-resonator design approach (Figure 4.21). The filter response depends on both the external quality factor (Q_e) and the coupling coefficient between the two resonators (k). The length (x) in Figure 4.21 controls the external quality factor, and the opening (y) and

spacing between the two posts (px) in Figure 4.21. (a) control the coupling between the resonators. These parameters can be found for a two-pole Butterworth filter ($g_0=1, g_1=g_2=1.414$) using equation (4.11) and equation (4.12) in the analysis in section 4.3.1:

$$Q_e = \frac{g_0 g_1}{\Delta} = 75.$$

$$k = \frac{\Delta}{\sqrt{g_1 g_2}} = 0.01344.$$

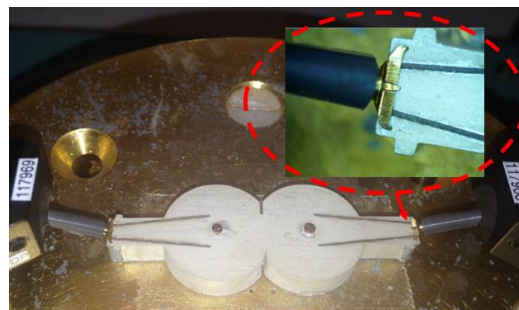
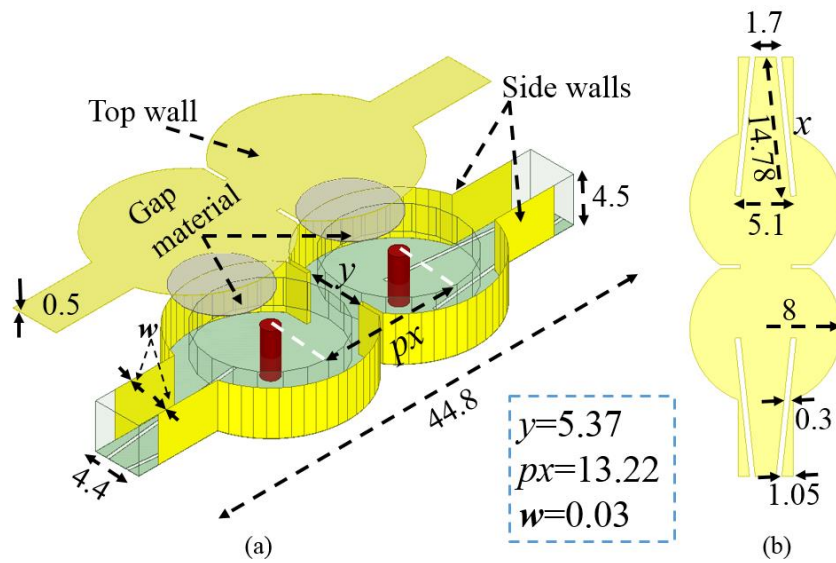


Figure 4.21: Laterally coupled evanescent-mode cavity filter (all dimensions are in mm). (a) filter structure (b) bottom wall and feedlines.

The post-to-post spacing and the feedline opening for a given internal coupling coefficient is plotted in Figure 4.22. The coupling coefficient can be calculated using the general formulation in equation (4.13):

$$k = \frac{f_{p2}^2 - f_{p1}^2}{f_{p2}^2 + f_{p1}^2}$$

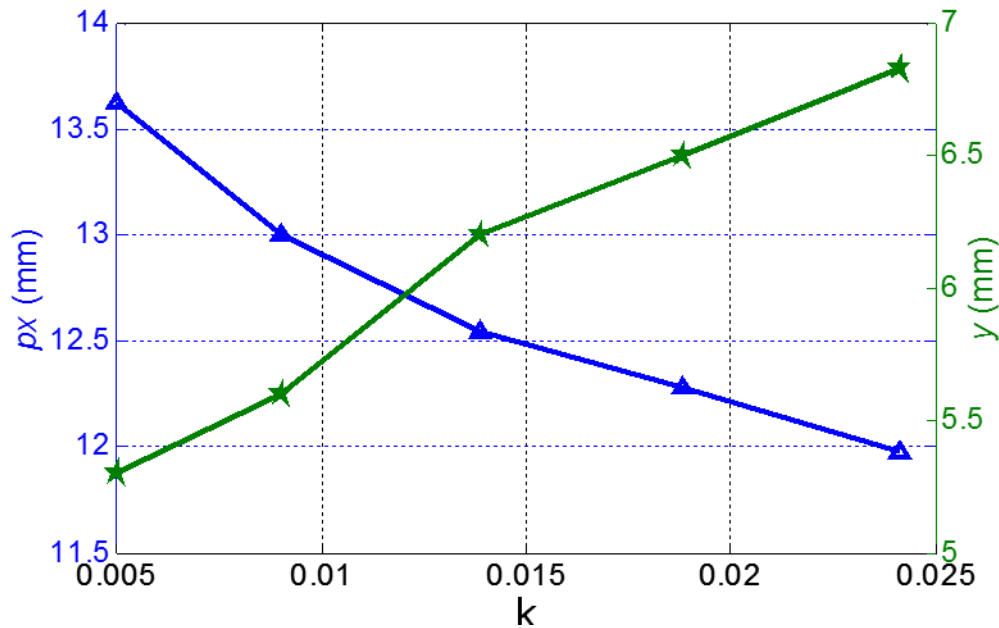


Figure 4.22: Post-to-post spacing (px) and opening (y) vs. internal coupling (k).

Tapered input and output shorted CPW laser-machined feed lines are used to provide the desired matching. ANSYS Electronics Desktop full-wave simulator is used to synthesize the filter design, and correct for the desired parameters. The filter fabrication process and assembly are shown in Figure 4.23, where the first step is to print the filter structure using FDM process and ABS material as shown in Figure 4.23 (a). Then, the cavity side walls and bottom side are coated with the conductive material (i.e., silver paste) to create the cavities, and then dried as described

previously at 90 C° for 60 minutes. Figure 4.23 (b) illustrates the coated structure after having it dried and laser machined to define the input and output feedlines. The next step is to prepare the top wall along with the gap filling material (the ULTALAM layer), where the ULTRALAM is attached to the non-dried CB028 that being used to coat the top wall, and then dried in the oven using the same temperature as shown in Figure 4.23 (c). Finally, after installing the two posts, the top wall is attached to the filter structure, where a small amount of the silver paste is used to glue the top wall and the filter structure together before drying the whole structure.

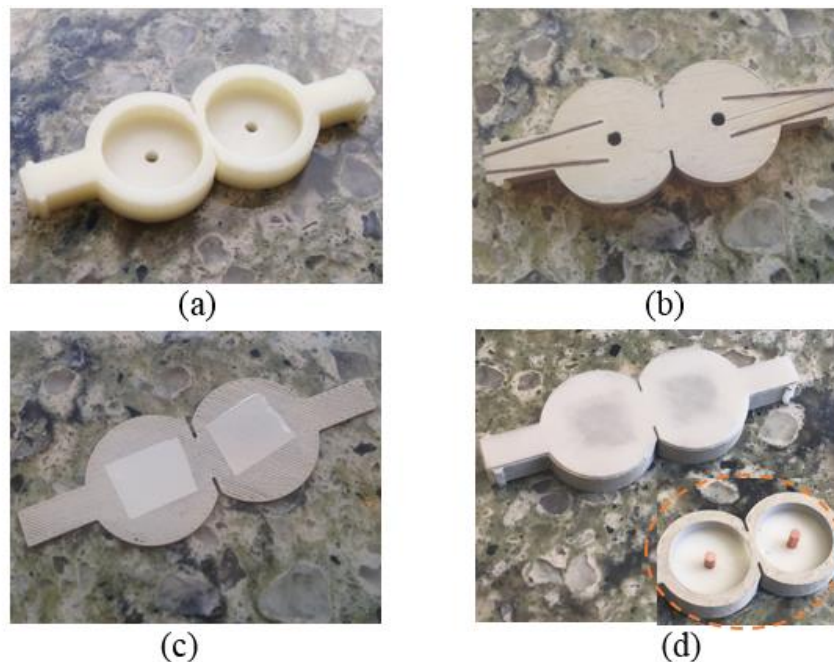
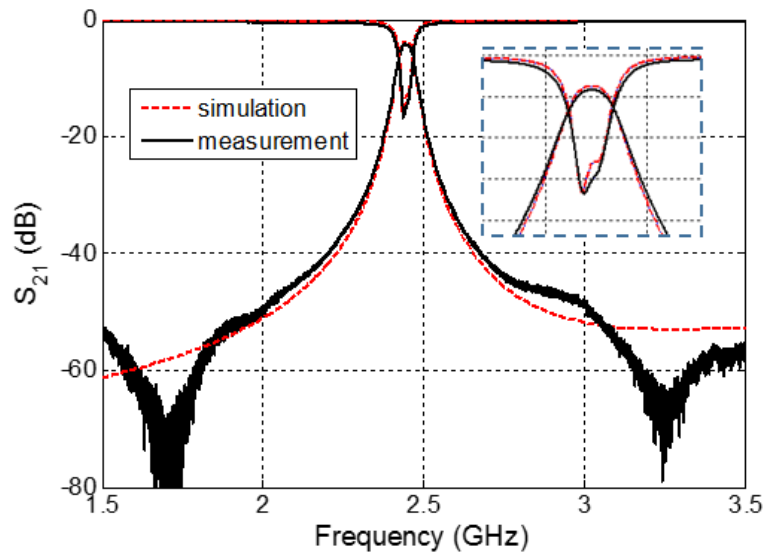


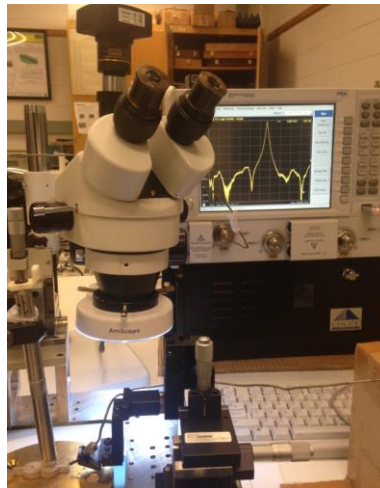
Figure 4.23: Fabrication and assembly steps of the laterally coupled filter.

The measurement is carried out using an Agilent Technologies PNA network analyzer N5227A and GGB 1850 micron-pitch microwave probes. The simulated and measured pass band insertion loss are 3.8 dB and 4.2 dB, and the simulated and measured return loss are 14 dB and 16 dB, respectively, as shown in Figure 4.24. The discrepancies between the simulation and measurement data are due to the fabrication process tolerances, e.g., the silver paste thickness

($\sim 30 \pm 10 \mu\text{m}$) and structural dimensions ($\sim \pm 100 \mu\text{m}$), and the surface roughness of 3-D printed structures [6]. The proposed filter can be tuned by changing the gap (g) for both coupled resonators to maintain the required coupling coefficient. Two measured examples are shown in Figure 4.25; the first one has 2% fractional bandwidth at 2.7 GHz with 3.85 dB IL, and the second one has 2.4% fractional bandwidth at 3.8 GHz with 3.55 dB IL. The gap has been controlled using a micro-positioner stage to illustrate the filter tuning capability.



(a)



(b)

Figure 4.24: Measured S-parameters of the laterally coupled filter. (a) Simulated and measured S-parameters (b) device under test

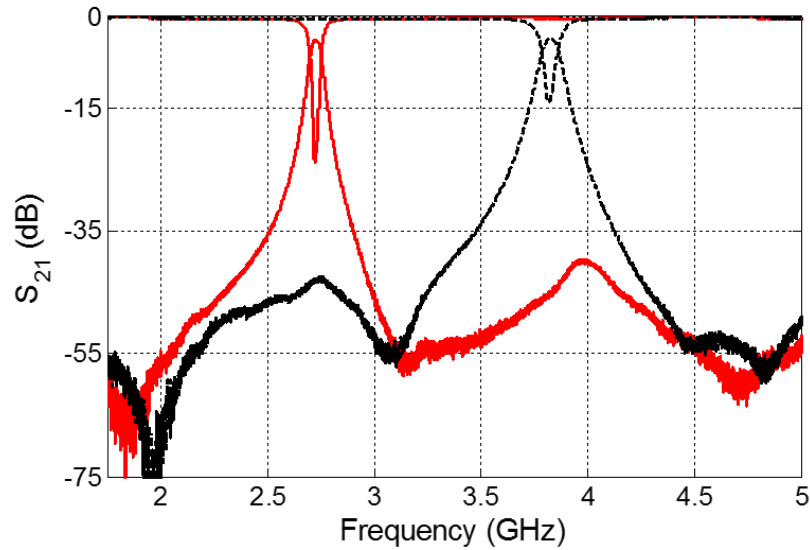


Figure 4.25: S-parameters of the 2% (red line), and 2.4% (black line) filter.

4.3.4 Direct Print Additively Manufactured Vertically-Coupled Band-Pass Filter

In this section, a new vertically-stacked structure of coupled, capacitively-loaded filter is described. Multi-layer vertically integrated filters are reported to improve performance, such as enhancing the filter selectivity, as well as contribute in achieving miniaturized filter volume [85-87]. In this regard, the proposed filter structure represents an excellent candidate for compact, highly-integrated multi-layer electronic systems. The design is especially attractive for situations where it is desirable to have the input and output ports on different levels, and with arbitrary orientations with respect to each other, e.g. parallel, anti-parallel and orthogonal orientations. This structure is an extension of the multi-layer DPAM approach described in [88], which is essentially a multi-layer printed circuit board (PCB), to a volumetric 3D form factor.

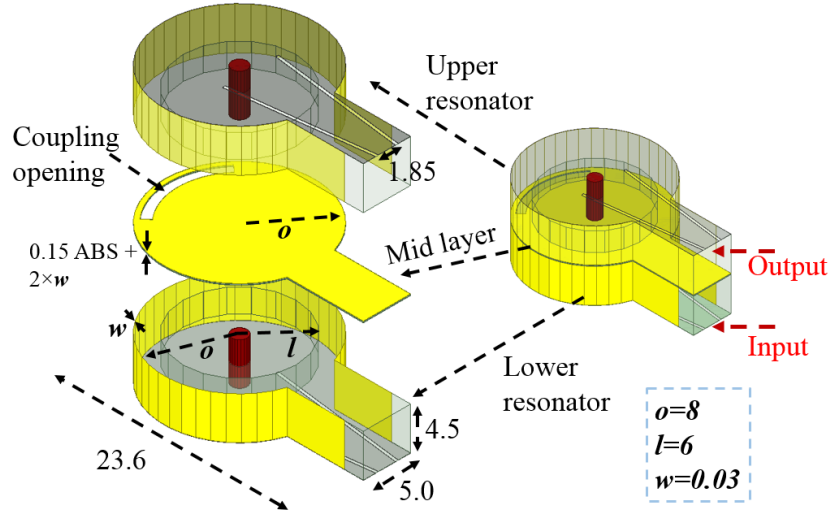
Using the Paralyene-coated resonator, a vertically-stacked two-pole, 1.9% fractional bandwidth (Δ) Butterworth filter is synthesized at 2.2 GHz adopting the coupled-resonator design approach (Figure 4.26). As previously described, the filter response depends on both the external quality factor (Q_e) and the coupling coefficient between the two resonators (k). The external quality

factor is controlled by the length (x) in Figure 4.26(b), while the coupling between resonators is controlled by the opening length (r) and width (rx) in Figure 4.26 (b). These parameters can be found for a two-pole Butterworth filter ($g_0=1, g_1=g_2=1.414$) using equation (4.11), and equation (4.12):

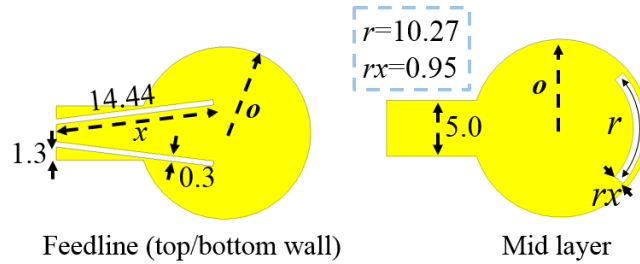
$$Q_e = \frac{g_0 g_1}{\Delta} = 75.$$

$$k = \frac{\Delta}{\sqrt{g_1 g_2}} = 0.01344.$$

The coupling opening length (r) for a given internal coupling coefficient is plotted in Figure 4.27. The coupling coefficient can be calculated using equation (4.13) as well. Tapered input and output shorted CPW feed lines are used to provide the desired matching as well. ANSYS Electronics Desktop full-wave simulator is used to synthesize the filter design, and correct for the desired parameters. The filter is fabricated using the same process that is used to fabricate the laterally coupled filter. The filter fabrication process and assembly sequence are shown in Figure 4.28. The first step is to print two of the single-resonators shown in Figure 4.28(a), using the FDM process and ABS material. Then, the conductive material (CB028 silver paste) is brushed onto the cavity sidewalls, and the bottom side and feedlines are created by micro-dispensing the silver paste as shown in Figure 4.28(b). These parts are dried as described previously at 90 C° for 60 minutes. The next step is to prepare the 150 μm -thick ABS mid-layer as shown in Figure 4.28(c) using the FDM process, and then brushing the two sides with the silver paste to act as the resonator top wall before drying it in the oven using the same temperature. The final step is to install the Parylene-coated posts, and then attach the two resonators and the mid-layer between them to create the stacked structure as described in Figure. 4.26, and shown in Figure 4.28(d). Silver paste is used to glue the three parts together before drying the whole structure.



(a)



(b)

Figure 4.26: Vertically-stacked capacitively-loaded cavity filter (all dimensions are in mm). (a) stacked structure (b) feedline and the mid-layer.

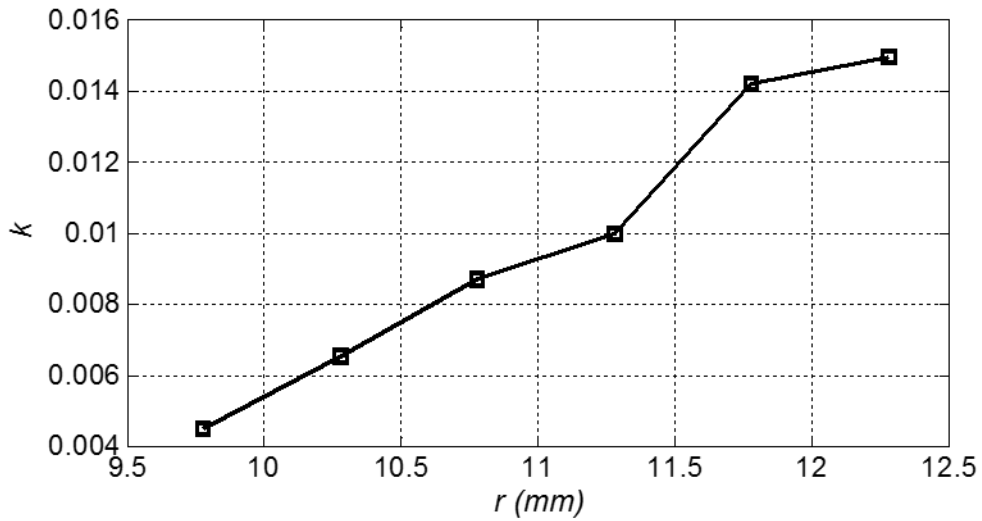


Figure 4.27: Coupling opening (r) vs. coupling coefficient (k).

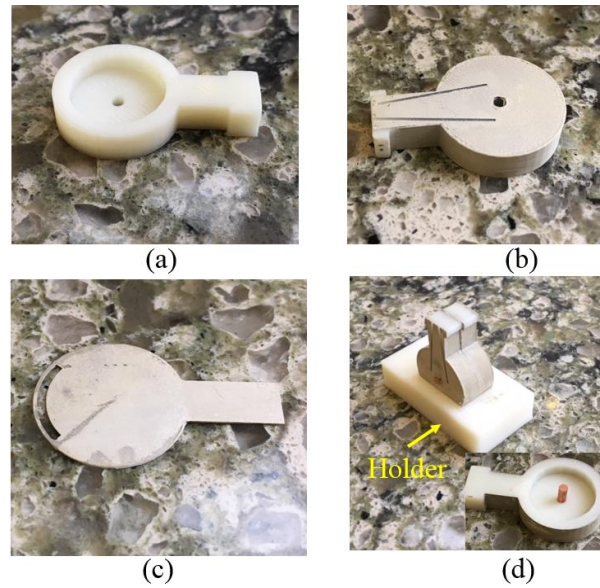


Figure 4.28: Fabrication and assembly steps of the vertically-stacked filter.

The measurement is carried out using an Agilent Technologies ENA E5063A and GGB 1850 micron-pitch microwave probes. Figure 4.29 shows the fabricated vertically-stacked filter. A fixture was printed to hold the filter such that the probes contact the feedline edges from the top as shown in Figure 4.30. The simulated and measured pass band insertion loss are 2.7 dB and 3.11 dB, and the simulated and measured return loss are 18 dB and 26 dB, respectively, as shown in Figure 4.31. The discrepancies between the simulation and measurement data are due to the fabrication process tolerances, e.g., the silver paste thickness ($\sim 30 \pm 10 \mu\text{m}$) and structural dimensions ($\sim \pm 100 \mu\text{m}$), and the surface roughness of 3-D printed structures [8].

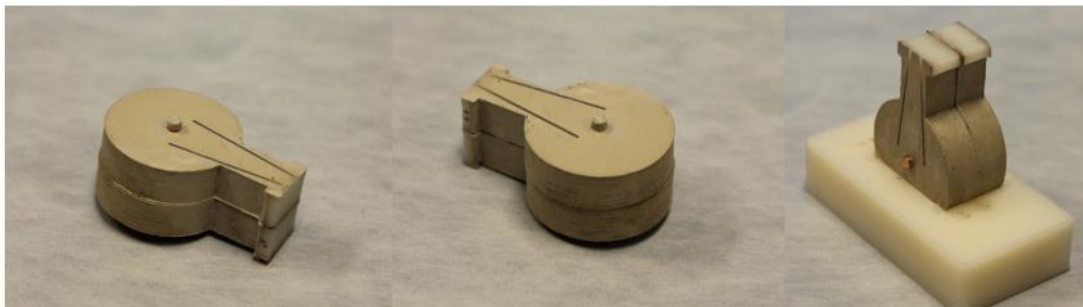
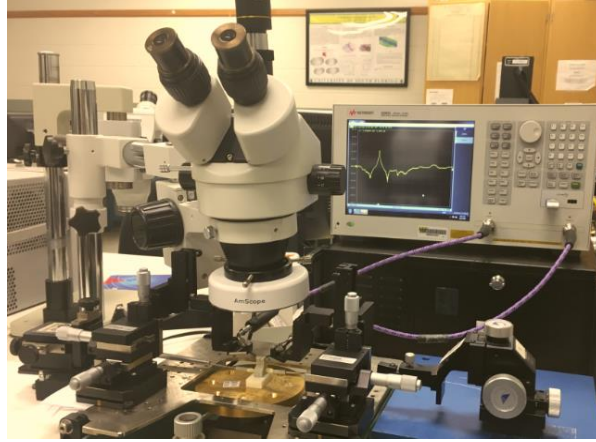
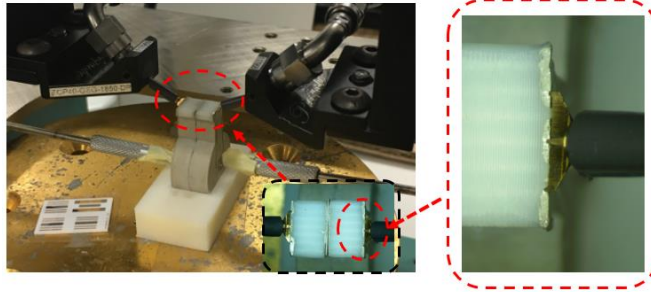


Figure 4.29: Fabricated vertically-stacked filter



(a)



(b)

Figure 4.30: Vertically-stacked capacitively-loaded cavity filter. (a) Device under test (b) Close-up image under the probe.

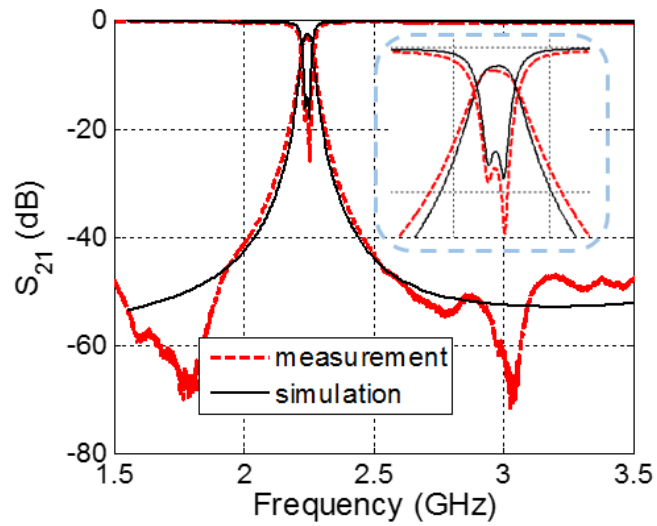


Figure 4.31: Simulated and measured S-parameters of the vertically stacked filter.

The architecture used for the proposed filter design allows for flexibility in the orientation of the feedlines. Because the input and output ports are on different levels, it would be possible to integrate the filter into a multi-layer configuration to transition between different functional levels of a front-end system as shown in Figure 4.32 (a). It is also possible to rotate the upper/lower resonators with respect to each other, as shown in in Figure 4.32 (b). The filter has a stable response when the upper resonator is rotated through different angles (45° , 90° , 135° , and 180°) as demonstrated by the simulation results in Figure 4.33. For the angles 135° and 180° , the coupling opening location is adjusted to maintain the same level of internal coupling, but without the need to change its dimensions.

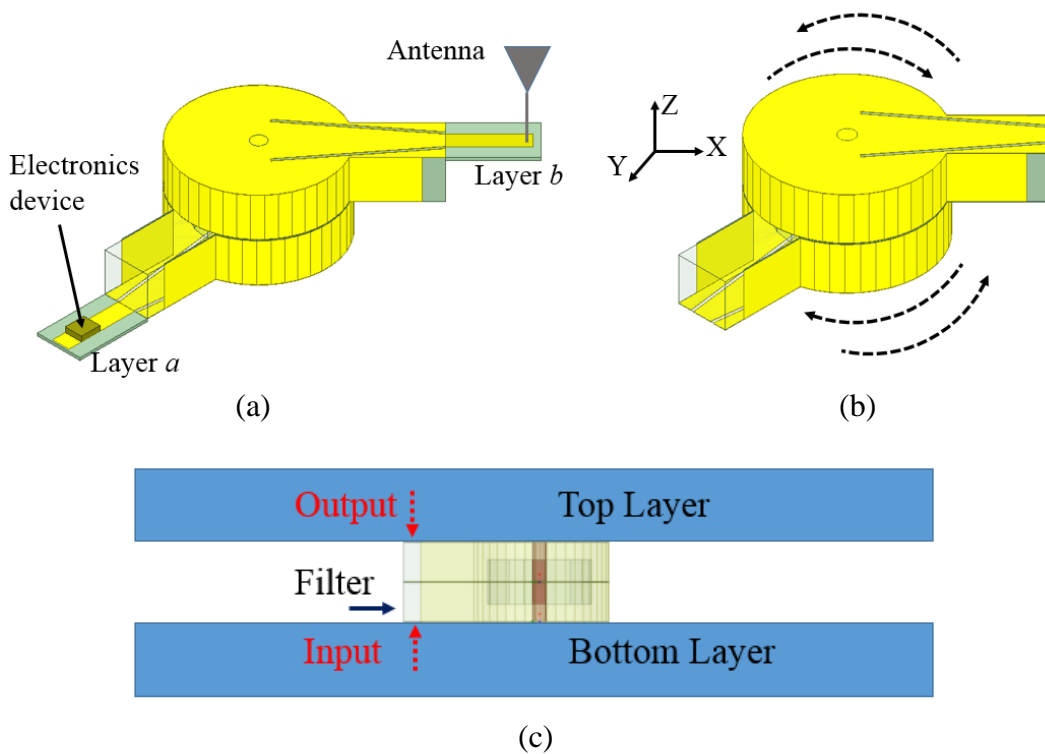


Figure 4.32: Multi-layer structure and Feedlines orientation.

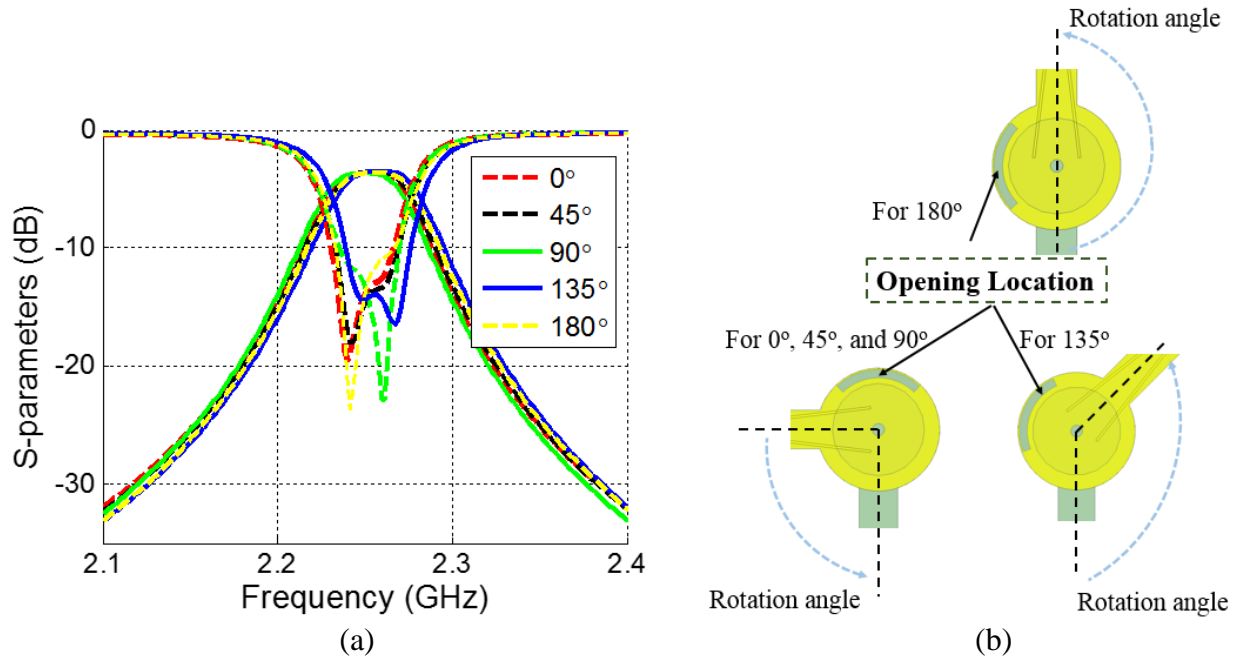


Figure 4.33: Filter simulated S-parameters for different rotation angles. (a) Simulated S-parameters (b) Coupling-opening location for different orientation angles.

4.4 Conclusion

This chapter presents the first 3D printed capacitively-loaded resonator and filter that are compatible with DPAM. The presented resonator, to the best of the authors' knowledge is the highest Q-factor resonator demonstrated to date using DPAM. The presented design approach simplifies the evanescent-mode resonator and filter fabrication, eliminating the need for micromachining and vias, and achieving a total weight of 1.12 g, 1.97 g, 1.91 for the single resonator, laterally-coupled filter, and vertically-coupled filter respectively. As well, the proposed laterally and vertically coupled filters present 40.12% and 35.43% smaller volume in par with [73]. The high performance, flexibility, as well as the low complexity and cost that DPAM combines outperform even high-Q planar/quasi-planar substrate integrated suspended lines (SISL) [93], [94]. According to [95], primary drawbacks of SISL designs are the high manufacturing complexity and cost.

CHAPTER 5: SUMMARY AND RECOMMENDATIONS FOR FUTURE WORK

5.1 Summary

This research focused on two main topics; (a) three dimensional direct print additively manufactured embedded antenna, and antenna array, and (b) three dimensional direct print additively manufactured high quality factor capacitively-loaded cavity resonator and filter. For the first part, the work was divided into three main sections; (i) new 3D implementation for the half-wave dipole and discussing the inherent roughness of 3D printed devices. This work presents the results on the 3D printed 6 GHz half-wave dipole antenna. The supporting ABS substrate is manufactured using fused deposition modeling and provides an inclined surface on which the antenna feed network and balun are deposited using micro-dispensing of thick-film Ag paste. Line dimensions down to 250 μm are held along the inclined plane, showing the potential for realizing high frequency 3D conformal designs using the digital printing technique. The simulations and measurements validate the antenna design procedure, where surface-wave loss reduction, and compact size have been achieved. Furthermore, any device prior to the antenna can be easily grounded, due to the close proximity of the feedline to the ground plane. The surface roughness study shows that it is important to consider the roughness effect, since it is considered as one of the main factors that explain the discrepancies between the simulation and measurement data (ii) new approach for implementing flexible antennas using micro-dispensing direct-print additive manufacturing (DPAM) and FDM processes is developed. The approach is useful for accomplishing 3D conformal designs, allows conductors to be printed on relatively smooth

surfaces of FDM-printed substrates, and allows for faster conductor printing with excellent dimensional control. This method also eliminates the challenges of silver paste dispensing on structures with sharp edges or inclined planes. The concept was proven with a 6 GHz 3D dipole antenna, and the measurements agree with the simulated performance (iii) an arrangement of the 3D designed half-wave dipole antenna elements in a 3D fashion to form a 2×2 array is proposed. The design improves the overall array performance by exploiting the single element advantages, and the advantages of having them in a non-planar configuration. Furthermore, the ability to reduce the array footprint by using the 3rd dimension is demonstrated. The excellent agreement between the simulated and measured data validates the design approach and analysis. The array is manufactured using direct digital manufacturing (DDM) technology. The supporting Acrylonitrile Butadiene Styrene (ABS) substrate is printed using fused deposition modeling and a thick-film Ag paste is used to form the dipole, balun, matching network, ground planes, and the 50Ω input feedlines.

The second part presents, to best of the author knowledge, the first DPAM resonator and filter, and it is divided into two main sections; (i) capacitively-loaded cavity resonator, where in this work evanescent-mode cavity resonator that can be manufactured using DPAM is presented. The supporting Acrylonitrile Butadiene Styrene (ABS) substrate is printed using fused deposition modeling (FDM), and a thick-film Ag paste is used to form the cavity walls and the input and output shorted CPW feedlines. For the prototype presented in this work, manual brushing versus micro-dispensing was used to deposit the conductive paste in the necessary areas. The design approach simplifies the evanescent-mode resonator fabrication, avoiding any need for micromachining or vias. The high degree of agreement between the simulation and measurement validates the design procedure, and provides a proof-of-principle for the DPAM microwave high-

Q resonator technology. The resonator performance was enhanced either by modifying the resonator structure, or by using lower loss material to act as the gap filling material (ii) capacitively-loaded cavity filter, where in this subsection a laterally-coupled and vertically-coupled filters are presented. The same fabrication process is used to accomplish both designs, where, the supporting ABS substrate is fabricated using fused deposition modeling (FDM), and silver paste (Dupont CB028) is used to metallize the top wall, side walls and the input and output shorted CPW feedlines. For the prototype purposes, manual brushing is used to form the conductive parts versus micro-dispensing for the lateral-coupled filter. For the vertically-coupled filter, the bottom wall and the feedlines are micro-dispensed, while manual brushing is used for the side walls, and mid-layer. However, new models of the nScrypt Tabletop 3Dn printers have the capability for conductive paste spraying, which fits the proposed design procedure. A DPAM-based post can replace the copper wire by controlling the surface roughness and the fabrication tolerance, as currently the post offers a smoother surface and better dimensional control. The presented design approach simplifies the evanescent-mode filter fabrication, eliminating the need for micromachining and vias, and achieving a total weight of 1.97 g and 1.91 g for the laterally-coupled and vertically-coupled filters respectively. The high degree of similarity between the simulation and measurement validates both the fabrication process and design procedure, and provides a proof-of-principle for high performance DPAM filter technology. At higher frequencies, the Q-factor improvement due to increased electrical size dominates over increasing skin effect loss, making the proposed structure a good candidate for higher microwave frequency designs as well.

5.2 Recommendation for Future Work

The capabilities the direct print additive manufacturing enables; either the high degree of freedom in shaping the structures or the capabilities to build multi-layer embedded systems, provide broad array of design ideas that could be taken into account in the future. For the work presented in this dissertation, below is a briefed list of research opportunities in future:

- (a) Develop an accurate model that captures the inherent properties of the direct printed additively manufactured devices, such as surface roughness. Such model will facilitate understanding and expecting the measurements, and save the time that might be spent on full-wave simulations to characterize these properties.
- (b) Integrating electronics in the antenna, and antenna array designs exploiting the ability to build the structure layer-by-layer. In the array structure, a phase shifter can be integrated to enable beam steering feature, which is one of the main factors to make the fifth generation of the wireless systems (5G) possible.
- (c) Develop an accurate model that represents the capacitively-loaded resonator, and able to capture the full behavior, such as the anti-resonance that current model doesn't support.
- (d) Investigate the behavior of the direct printed additively manufactured resonator and filter at very high frequencies.
- (e) Design robust tuning mechanism for the capacitively-loaded resonator and filter, such as using step motor to control the post displacement.
- (f) Study the roughness effect on the capacitively-loaded resonator quality factor. As well, investigate the effect of plating the resonator's walls with higher conductivity material such as copper-plating.

5.3 Perspective on Additive Manufacturing

The EM performance presented by the additively manufactured devices in this dissertation builds a strong case for introducing DPAM manufactured antennas and filters in the market. However, for any RF product, EM performance is just a part of the final product. This section will focus on other aspects that directly have an impact on those devices to make them real products:

- (a) Power handling is one of the main specs that plays a role in determining device usability and application. In this regard, the power handling capabilities of the presented DPAM antennas and filters need to be investigated in future work.
- (b) Thermal properties of the used materials are very important and must be considered in future work. For example, ABS has a coefficient of linear thermal expansion of $\sim 90 \times 10^{-5}/\text{K}$, which means that 4.0 cm piece of ABS will increase by 0.3 mm if its temperature is changed from 25 C° to 100 C°. These changes due to temperature will have an effect on the RF performance at the design frequency, which implies that addressing such an important factor is crucial before commercialization.
- (c) Device sensitivity toward fabrication tolerances should be described carefully by replacing each parameter of the device with its fabrication tolerance as a \pm value. The less the sensitivity, the better the device, and the datasheet specs in real products are set after running the sensitivity test as each fabrication process has its own tolerance.
- (d) The yield of any fabrication technology is a very important factor that determines the overall cost and the ability to provide large/massive production. For the DPAM devices presented in this dissertation, the goal was to provide a proof-of-principle on the RF capabilities. Large production capabilities need very careful testing, which should be considered in future work.

- (e) Device lifetime and reliability as well are important specs, where they indicate on how long this device will keep running and how well it behaves while running.
- (f) Automation and repeatability are key points to develop a process that is able to support a production line. The current fabrication process is user-dependent, which provides developers flexibility and freedom to effectively utilizes all capabilities of the DPAM fabrication technology, but for a production process automation is required.
- (g) Packaging is a big topic, which needs to be developed and characterized carefully as it impacts the EM performance directly. Good packaging results in a robust and immune product, where it is known to make a design outperform other designs that are manufactured using the same technology. DPAM process represents an excellent candidate as packaging technology, which gives it an advantage to fabricate the device and package it using the same tool.

To conclude, the direct print additive manufacturing is a very promising technology that requires a collaboration between engineering from different fields such as software engineers, material engineers, process engineers, mechanical engineers, and test engineers in order to extend it into the commercial market. Additionally, DPAM has a great opportunity to contribute in future communication systems and applications such as the fifth generation wireless systems (5G), unmanned aerial vehicles (UAV), and cubesat design as it offers high degree of design flexibility and performs very well at higher frequencies.

REFERENCES

- [1] K. H. Church et al., "Multimaterial and Multilayer Direct Digital Manufacturing of 3-D Structural Microwave Electronics," in *Proceedings of the IEEE*, vol. 105, no. 4, pp. 688-701, April 2017.
- [2] W. T., "Wohlers Report 2015: Global Reports.," Wohlers Associates, Belgium 2015.
- [3] S. Zistl, "3D Printing: Facts & Forecasts," Siemens, 2014.
- [4] E. A. Rojas-Nastrucci; H. Tsang; P. I. Deffenbaugh; R. A. Ramirez; D. Hawatmeh; A. Ross; K. Church; T. M. Weller, "Characterization and Modeling of K-Band Coplanar Waveguides Digitally Manufactured Using Pulsed Picosecond Laser Machining of Thick-Film Conductive Paste," in *IEEE Transactions on Microwave Theory and Techniques*, vol. PP, no. 99, pp. 1-8
- [5] N. Arnal et al., "3D multi-layer additive manufacturing of a 2.45 GHz RF front end," 2015 *IEEE MTT-S International Microwave Symposium*, Phoenix, AZ, 2015, pp. 1-4.
- [6] D. F. Hawatmeh, S. LeBlanc, P. I. Deffenbaugh and T. Weller, "Embedded 6-GHz 3-D Printed Half-Wave Dipole Antenna," in *IEEE Antennas and Wireless Propagation Letters*, vol. 16, pp. 145-148, 2017.
- [7] Nassar, I.T.; Wang, J.; Frolik, J.L.; Weller, T.M., "A High-Efficiency, Miniaturized Sensor Node With 3-D Machined-Substrate Antennas for Embedded Wireless Monitoring," *Sensors Journal*, IEEE, vol. 15, no. 9, pp. 5036, 5044, Sept. 2015.
- [8] Thomas Ketterl, Casey Perkowski, Paul Deffenbaugh, John Stratton, Joshua Stephenson, Kenneth Church, and Thomas Weller, "Direct Digital Manufacturing of a 2.45 GHz Phased Array," 2016 *URSI Conference – invited paper*, Boulder, Colorado, January 2016.
- [9] Kenneth Church, Xudong Chen, Paul Deffenbaugh, Casey Perkowski, Sam LeBlanc, Eduardo Rojas, Thomas Weller, "Turning Printed Circuit Boards into Printed Circuit Structures using 3D Printing," 2014 *SMTA Conference*, August 2014.
- [10] J. O'Brien et al., "Miniaturization of microwave components and antennas using 3D manufacturing," 2015 *9th European Conference on Antennas and Propagation (EuCAP)*, Lisbon, 2015, pp. 1-4.

- [11] A. Vera López, E. A. Rojas-Nastrucci, M. Córdoba-Erazo, T. Weller, and J. Papapolymerou, "Ka-Band Characterization and RF Design of Acrylonitrile Butadiene Styrene (ABS)," presented at the Microwave Symposium (IMS), 2014 IEEE MTT-S International, 2015.
- [12] P. I. Deffenbaugh, R. C. Rumpf, and K. H. Church, "Broadband Microwave Frequency Characterization of 3-D Printed Materials," *Components, Packaging and Manufacturing Technology*, IEEE Transactions on, vol. 3, pp. 2147-2155, 2013.
- [13] M. F. Cordoba-Erazo, E. A. Rojas-Nastrucci, and T. Weller, "Simultaneous RF electrical conductivity and topography mapping of smooth and rough conductive traces using microwave microscopy to identify localized variations," in *Wireless and Microwave Technology Conference (WAMICON)*, 2015 IEEE 16th Annual, 2015, pp. 1-4.
- [14] E. A. Rojas-Nastrucci, T. Weller, V. Lopez Aida, C. Fan, and J. Papapolymerou, "A study on 3D-printed coplanar waveguide with meshed and finite ground planes," in *Wireless and Microwave Technology Conference (WAMICON)*, 2014 IEEE 15th Annual, 2014, pp. 1-3.
- [15] C. Fan, C. Yung-hang, W. Kan, W. T. Khan, S. Pavlidis, and J. Papapolymerou, "High resolution aerosol jet printing of D- band printed transmission lines on flexible LCP substrate," in *2014 IEEE MTT-S International Microwave Symposium (IMS)*, 2014, pp. 1-3.
- [16] I. T. Nassar, T. M. Weller, and H. Tsang, "A 3-D printed miniaturized log-periodic dipole antenna," in *Antennas and Propagation Society International Symposium (APSURSI)*, 2014 IEEE, 2014, pp. 11-12.
- [17] I. Nassar, H. Tsang, and T. Weller, "3D printed wideband harmonic transceiver for embedded passive wireless monitoring," *Electronics Letters*, vol. 50, pp. 1609-1611, 2014.
- [18] M. Liang, C. Shemelya, E. MacDonald, R. Wicker, and H. Xin, "3-D Printed Microwave Patch Antenna via Fused Deposition Method and Ultrasonic Wire Mesh Embedding Technique," *Antennas and Wireless Propagation Letters*, IEEE, vol. 14, pp. 1346-1349, 2015.
- [19] E. MacDonald, R. Salas, D. Espalin, M. Perez, E. Aguilera, D. Muse, et al., "3D Printing for the Rapid Prototyping of Structural Electronics," *Access*, IEEE, vol. 2, pp. 234-242, 2014.
- [20] T. Merkle, R. Gotzen, C. Joo-Young, and S. Koch, "Polymer Multichip Module Process Using 3-D Printing Technologies for D-Band Applications," *Microwave Theory and Techniques*, IEEE Transactions on, vol. 63, pp. 481-493, 2015.

- [21] A. M. N. Al-Mobin, R. Shankar, W. Cross, J. Kellar, K. W. Whites, and D. E. Anagnostou, "Advances in direct-write printing of RF-MEMS using M3D," in *Microwave Symposium (IMS), 2014 IEEE MTT-S International*, 2014, pp. 1-4.
- [22] F. Calignano et al., "Overview on Additive Manufacturing Technologies," in *Proceedings of the IEEE*, vol. 105, no. 4, pp. 593-612, April 2017.
- [23] B. Sanz-Izquierdo and E. A. Parker, "3D printing technique for fabrication of frequency selective structures for built environment," *Electron. Lett.*, vol. 49, no. 18, pp. 1117–1118, Aug. 2013.
- [24] A. M. N. Ai-Mobin, R. Shankar, W. Cross, J. Kellar, K. W. Whites, and D. E. Anagnostou, "Advances in direct-write printing of RF-MEMS using M3D," in *IEEE MTT-S Int. Microw. Symp. Dig.*, Jun. 2014, pp. 1–6.
- [25] W. J. Otter and S. Lucyszyn, "Hybrid 3-D-Printing Technology for Tunable THz Applications," in *Proceedings of the IEEE*, vol. 105, no. 4, pp. 756-767, April 2017.
- [26] C. J. Kief et al., "Printing multi-functionality: Additive manufacturing for CubeSats," in *Proc. AIAA SPACE Conf. Expo.*, San Diego, CA, USA, 2014, pp. 1–9.
- [27] T. Merkle, R. Götzen, J. Y. Choi, and S. Koch, "Polymer multichip module process using 3-D printing technologies for D-band applications," *IEEE Trans. Microw. Theory Techn.*, vol. 63, no. 2, pp. 481–493, Feb. 2015.
- [28] I.T. Nassar, T.M. Weller, "An electrically-small, 3-D cube antenna fabricated with additive manufacturing", *IEEE Topical Conference on Wireless Sensors and Sensor Networks (WiSNet)*, pp. 58 – 60, 2013.
- [29] C. M. Kruesi, R. J. Vyas, and M. M. Tentzeris, "Design and development of a novel 3-D cubic antenna for wireless sensor networks (WSNs) and RFID applications," *IEEE Trans. Antennas Propag.*, vol. 57, no. 10, pp. 3293–3299, Oct. 2009.
- [30] M.F. Farooqui, and A. Shamim, "An inkjet printed near isotropic 3-D antenna with embedded electronics for wireless sensor applications", *IEEE antennas and propagation society international symposium*, pp. 326-327, 2014.
- [31] J.R. Cooper, M.M. Tentzeris, "Novel "smart cube" wireless sensors with embedded processing/communication/power core for "smart skins" applications", *IEEE sensors conference*, pp. 1-4, 2012.
- [32] J. Adams, S. Slimmer, T. Malkowski, E. Duoss, J. Lewis, and J. Bernhard, "Comparison of spherical antennas fabricated via conformal printing: Helix, Meanderline, and Hybrid Designs," *IEEE Antennas Wireless Propag. Lett.*, vol. 10, pp. 1425-1428, 2011.

- [33] A.J. Fenn, D. J. Pippin, D. Hogan, C.M. Lamb, F. G. Willwerth, H.M Aumann, J. P. Doane, 3D-Printed Conformal Microstrip Patch Array Antenna: Simulations and Measurements, 31st International Review of Progress in Applied Computational Electromagnetics, Williamsburg, VA, March 22-26, 2015.
- [34] H. Shirinabadi, M. Ahmadi-Boroujeni, E. Arbabi and K. Mohammadpour-Aghdam, "Design of a printed non-planar dual-polarised log-periodic dipole array," in *IET Microwaves, Antennas & Propagation*, vol. 11, no. 4, pp. 490-494, 3 18 2017.
- [35] J. R. Brianeze, A. C. Sodré and H. E. Hernández-Figueroa, "Tridimensional Yagi antenna: shaping radiation pattern with a non-planar array," in *IET Microwaves, Antennas & Propagation*, vol. 4, no. 9, pp. 1434-1441, September 2010.
- [36] M. J. Bentum, I. E. Lager, S. Bosma, W. P. Bruinsma and R. P. Hes, "Beamforming in sparse, random, 3D array antennas with fluctuating element locations," *2015 9th European Conference on Antennas and Propagation (EuCAP)*, Lisbon, 2015, pp. 1-5.
- [37] M. W. Rousstia, A. C. F. Reniers and M. H. A. J. Herben, "An 11-GHz multi-beam dielectric rod antenna using non-planar array approach," *The 8th European Conference on Antennas and Propagation (EuCAP 2014)*, The Hague, 2014, pp. 1697-1701.
- [38] X. Cai, W. Geyi and H. Sun, "A Printed Dipole Array With High Gain and Endfire Radiation," in *IEEE Antennas and Wireless Propagation Letters*, vol. 16, pp. 1512-1515, 2017.
- [39] I. J. Gupta *et al.*, "Non-Planar Adaptive Antenna Arrays for GPS Receivers," in *IEEE Antennas and Propagation Magazine*, vol. 52, no. 5, pp. 35-51, Oct. 2010.
- [40] A. Vesa, F. Alexa and H. Baltă, "Comparisons between 2D and 3D uniform array antennas," *2015 Federated Conference on Computer Science and Information Systems (FedCSIS)*, Lodz, 2015, pp. 1285-1290.
- [41] N. Herscovici, "Nonplanar microstrip arrays," in *IEEE Transactions on Antennas and Propagation*, vol. 44, no. 3, pp. 389-392, Mar 1996.
- [42] A. C. Durgun, M. S. Reese, C. A. Balanis, C. R. Birtcher, D. R. Allee, and S. Venugopal, "Flexible bow-tie antennas with reduced metallization," in *Radio and Wireless Symposium (RWS), 2011 IEEE*, 2011, pp. 50-53.
- [43] A. C. Durgun, C. A. Balanis, C. R. Birtcher, and D. R. Allee, "Design, Simulation, Fabrication and Testing of Flexible Bow-Tie Antennas," *Antennas and Propagation, IEEE Transactions on*, vol. 59, pp. 4425-4435, 2011.

- [44] O. Jungsuek, L. Kyusang, T. Hughes, S. Forrest, and K. Sarabandi, "Flexible Antenna Integrated With an Epitaxial Lift-Off Solar Cell Array for Flapping-Wing Robots," *Antennas and Propagation, IEEE Transactions on*, vol. 62, pp. 4356-4361, 2014.
- [45] K. Hiraguri, F. Koshiji, and K. Koshiji, "A flexible broadband antenna with fan-shaped and trapezoidal elements formed on printed circuit board for ultra-wideband radio," in *Electronics Packaging (ICEP), 2014 International Conference on*, 2014, pp. 807-810.
- [46] S. Shao-Rui, W. Yu-Ming, L. Pei-Pei, and W. Qun, "Investigation on the radiation features of the flexible antenna at 5.8GHz," in *Antennas and Propagation (APCAP), 2014 3rd Asia-Pacific Conference on*, 2014, pp. 1496-1500.
- [47] Q. Yijie, J. Yei Hwan, L. Subin, S. Ting-Yen, L. Juhwan, X. Yue Hang, *et al.*, "Compact parylene-c-coated flexible antenna for WLAN and upper-band UWB applications," *Electronics Letters*, vol. 50, pp. 1782-1784, 2014.
- [48] C.-Y. Chi and G. M. Rebeiz, "A low-loss 20 GHz micromachined bandpass filter," in *IEEE MTT-S Int. Microwave Symp. Dig.*, Orlando, FL, May 1995, pp. 1531–1534.
- [49] A. R. Brown and G. M. Rebeiz, "Micromachined micropackaged filter banks," *IEEE Microwave Guided Wave Lett.*, vol. 8, pp. 158–160, Apr. 1998.
- [50] P. Blondy, A. R. Brown, D. Cros, and G. M. Rebeiz, "Low-loss micromachined filters for millimeter-wave communication systems," *IEEE Trans. Microwave Theory Tech.*, vol. 46, pp. 2283–2288, Dec. 1998.
- [51] T. A. Schwarz, and L. P. B. Katehi, "A Micromachined Evanescent Mode Resonator", 1999 European Microwave Conference Dig., vol. 2, pp. 403- 406, October 1999.
- [52] K. Takahashi et al., "K-band receiver front-end IC integrating micromachined filter and flip-chip assembled active devices," in *IEEE MTT-S Int. Microwave Symp. Dig.*, Anaheim, CA, June 1999, pp. 229–232.
- [53] X. Gong, A. Margomenos, B. Liu, S. Hajela, L. P. B. Katehi and W. J. Chappell, "Precision Fabrication Techniques and Analysis on High Q Evanescent-Mode Resonators and Filters of Different Geometries," *IEEE Trans. Microwave Theory & Tech.*, vol. 52, no. 11, pp. 2557-2566, November 2004.
- [54] L. Harle and L. P. B. Katehi, "A vertically integrated micromachined filter," in *IEEE Transactions on Microwave Theory and Techniques*, vol. 50, no. 9, pp. 2063-2068, Sep 2002.

- [55] Xiaoguang Liu, L. P. B. Katehi, W. J. Chappell and D. Peroulis, "A 3.4 – 6.2 GHz Continuously tunable electrostatic MEMS resonator with quality factor of 460–530," 2009 IEEE MTT-S International Microwave Symposium Digest, Boston, MA, 2009, pp. 1149–1152.
- [56] X. Liu, L. P. B. Katehi, W. J. Chappell and D. Peroulis, "Power Handling of Electrostatic MEMS Evanescent-Mode (EVA) Tunable Bandpass Filters," in *IEEE Transactions on Microwave Theory and Techniques*, vol. 60, no. 2, pp. 270-283, Feb. 2012.
- [57] M. S. Arif and D. Peroulis, "A 6 to 24 GHz continuously tunable, microfabricated, high-Q cavity resonator with electrostatic MEMS actuation," *2012 IEEE/MTT-S International Microwave Symposium Digest*, Montreal, QC, Canada, 2012, pp. 1-3.
- [58] L. Young, and D. Weller, "A 500-to-1000 MHz magnetically tunable band-pass filter using two YIG-disk resonators," *Ieee Transactions on Microwave Theory and Thecniques*, vol. MTT-15, no. 2, pp. 72-86, February 1967
- [59] W. J. Keane, "Narrow-Band Yig Filters Aid Wide-Open Receivers," *Microwaves*, vol. 17, pp. 50-&, 1978
- [60] W. J. Keane, "YIG filters aid wide open receivers," *Microw. J.*, vol. 17, no. 8, pp. 295–308, Sep. 1980.
- [61] Y. Murakami, T. Ohgihara, and T. Okamoto, "A 0.5-4.0-GHz tunable bandpass filter using YIG film grown by LPE," *Ieee Transactions on Microwave Theory and Techniques*, vol. MTT-35, no. 12, pp. 1192-1198, December 1987.
- [62] C. Guo, X. Shang, M. J. Lancaster, and J. Xu, "A 3-D printed lightweight X-band waveguide filter based on spherical resonators," *IEEE Microw. Compon. Lett.*, vol. 25, no. 7, pp. 442–444, Jul. 2015.
- [63] C. Guo, X. Shang, J. Li, F. Zhang, M. J. Lancaster and J. Xu, "A Lightweight 3-D Printed X-Band Bandpass Filter Based on Spherical Dual-Mode Resonators," in *IEEE Microwave and Wireless Components Letters*, vol. 26, no. 8, pp. 568-570, Aug. 2016.
- [64] J. Maas, B. Liu, S. Hajela, Y. Huang, X. Gong and W. J. Chappell, "Laser-Based Layer-by-Layer Polymer Stereolithography for High-Frequency Applications," in *Proceedings of the IEEE*, vol. 105, no. 4, pp. 645-654, April 2017.
- [65] O. A. Peverini, M. Lumia, F. Calignano, G. Addamo, M. Lorusso, E. P. Ambrosio, et al., "Selective Laser Melting Manufacturing of Microwave Waveguide Devices," *Proc. IEEE*, vol. 105, pp. 620- 631, Apr. 2017.

- [66] A.M. Sánchez, M. Ribó, L. Pradell, J. Anguera and A. Andújar, "CPW balun for printed balanced antennas", *Electronics Letters*, vol. 50. No. 11, pp. 785-786, 2014.
- [67] S. P. Morgan, "Effect of surface roughness on eddy current losses at microwave frequencies," *J. Applied Physics*, p. 352, v. 20, 1949.
- [68] S. Groiss, I. Bardi, O. Biro, K. Preis, and K. R. Richter, "Parameters of lossy cavity resonators calculated by the finite element method", *IEEE Transactions on Magnetics*, Vol. 32, No.3, pp. 894-897, May 1996.
- [69] P.G. Huray, S.G. Pytel, S.H. Hall, F. Oluwafemi, R.I. Mellitz, D. Hua, and P. Ye, "Fundamentals of a 3-D "Snowball" model for surface roughness power losses", *11th Annual IEEE SPI Proceedings*, May 13 - 16, 2007.
- [70] S.H. Hall, S.G. Pytel, P.G. Huray, D. Hua, A. Moonshiram, G. Brist, and E. Sijercic, "Multi-GHz, causal transmission line modeling methodology with a hemispherical surface roughness approach", *IEEE Transactions on Microwave Theory and Techniques*, December 2007 pp 2614 - 2624.
- [71] S.G. Pytel, P.G. Huray, A. Moonshiram, S.H. Hall, R.I. Mellitz, G. Brist, F. Oluwafemi, H.M. Meyer, L. Walker, and M. Garland, "Analysis of copper treatments and the effects on signal propagation", *58th Annual IEEE ECTC*, May 26 - 30, 2008, pp 1144 – 1149.
- [72] F. Cai, W. Khan and J. Papapolymerou, "A Low Loss X-band Filter Using 3-D Polyjet Technology," *IEEE MTT-S Int. Microwave Symp.*, 2015.
- [73] X. Liu, L. P. B. Katehi, W. J. Chappell and D. Peroulis, "High- Q Tunable Microwave Cavity Resonators and Filters Using SOI-Based RF MEMS Tuners," in *Journal of Microelectromechanical Systems*, vol. 19, no. 4, pp. 774-784, Aug. 2010.
- [74] H. Sharifi, R. R. Lahiji, H. C. Lin, P. D. Ye, L. P. B. Katehi and S. Mohammadi, "Characterization of Parylene-N as Flexible Substrate and Passivation Layer for Microwave and Millimeter-Wave Integrated Circuits," in *IEEE Transactions on Advanced Packaging*, vol. 32, no. 1, pp. 84-92, Feb. 2009.
- [75] J.-S. Hong and M. J. Lancaster, in *Microstrip Filters for RF/Microwave Applications*, ed: John Wiley & Sons, Inc., 2001.
- [76] A. E. Atia and A. E. Williams, "Narrow-Bandpass Waveguide Filters," in *IEEE Transactions on Microwave Theory and Techniques*, vol. 20, no. 4, pp. 258-265, Apr 1972.
- [77] L. Accatino, G. Bertin and M. Mongiardo, "A four-pole dual mode elliptic filter realized in circular cavity without screws," in *IEEE Transactions on Microwave Theory and Techniques*, vol. 44, no. 12, pp. 2680-2687, Dec 1996.

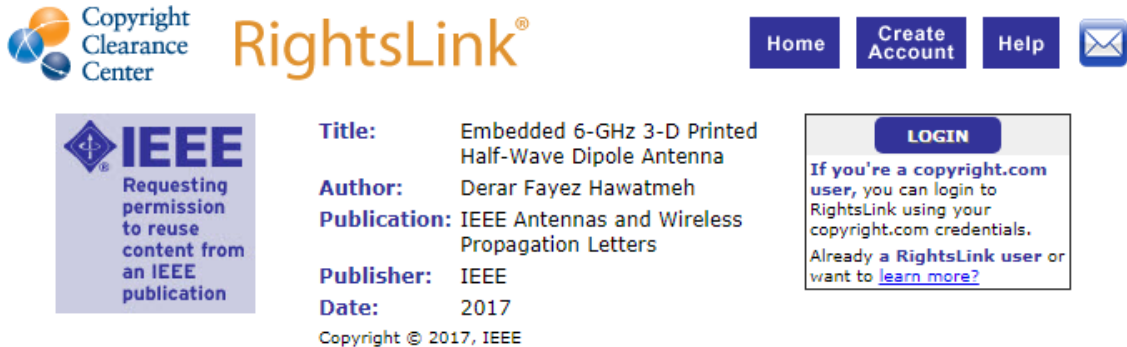
- [78] Jia-Sheng Hong and M. J. Lancaster, "Couplings of microstrip square open-loop resonators for cross-coupled planar microwave filters," in *IEEE Transactions on Microwave Theory and Techniques*, vol. 44, no. 11, pp. 2099-2109, Nov 1996.
- [79] Jia-Sheng Hong and M. J. Lancaster, "Theory and experiment of novel microstrip slow-wave open-loop resonator filters," in *IEEE Transactions on Microwave Theory and Techniques*, vol. 45, no. 12, pp. 2358-2365, Dec 1997.
- [80] Jia-Sheng Hong and M. J. Lancaster, "Cross-coupled microstrip hairpin-resonator filters," in *IEEE Transactions on Microwave Theory and Techniques*, vol. 46, no. 1, pp. 118-122, Jan 1998.
- [81] H. W. Yao, C. Wang and A. K. Zaki, "Quarter wavelength ceramic combline filters," in *IEEE Transactions on Microwave Theory and Techniques*, vol. 44, no. 12, pp. 2673-2679, Dec 1996.
- [82] C. Wang, H. W. Yao, K. A. Zajum and R. Mansour, "Mixed modes cylindrical planar dielectric resonator filters with rectangular enclosure," *Proceedings of 1995 IEEE MTT-S International Microwave Symposium*, Orlando, FL, USA, 1995, pp. 501-504 vol.2.
- [83] P. Blondy, A. R. Brown, D. Cros and G. M. Rebeiz, "Low-loss micromachined filters for millimeter-wave communication systems," in *IEEE Transactions on Microwave Theory and Techniques*, vol. 46, no. 12, pp. 2283-2288, Dec 1998.
- [84] Jia-Sheng Hong, M. J. Lancaster, D. Jedamzik and R. B. Greed, "On the development of superconducting microstrip filters for mobile communications applications," in *IEEE Transactions on Microwave Theory and Techniques*, vol. 47, no. 9, pp. 1656-1663, Sep 1999.
- [85] J. X. Chen, Y. L. Li, W. Qin, Y. J. Yang and Z. H. Bao, "Compact Multi-Layer Bandpass Filter With Wide Stopband Using Selective Feeding Scheme," in *IEEE Transactions on Circuits and Systems II: Express Briefs*, vol. PP, no. 99, pp. 1-1.
- [86] M. Khalil, M. Kamarei, J. Jomaah and H. Ayad, "Compact multi-layer Band-Pass filter in Substrate Integrated Waveguide (SIW) technology," *2016 IEEE Middle East Conference on Antennas and Propagation (MECAP)*, Beirut, 2016, pp. 1-4.
- [87] T. Y. Huang, T. M. Shen, B. J. Chen, H. Y. Chien and R. B. Wu, "Design of miniaturized vertically stacked SIW filters in LTCC," *2009 European Microwave Conference (EuMC)*, Rome, 2009, pp. 413-416.
- [88] T. P. Ketterl et al., "A 2.45 GHz Phased Array Antenna Unit Cell Fabricated Using 3-D Multi-Layer Direct Digital Manufacturing," in *IEEE Transactions on Microwave Theory and Techniques*, vol. 63, no. 12, pp. 4382-4394, Dec. 2015.

- [89] D. Hawatmeh, E. Rojas-Nastrucci and T. Weller, "A multi-material 3D printing approach for conformal microwave antennas," *2016 International Workshop on Antenna Technology (iWAT)*, Cocoa Beach, FL, 2016, pp. 7-10.
- [90] D. Hawatmeh and T. Weller, "Embedded 6 GHz 3D-printed half-wave dipole antenna array," *2017 IEEE 18th Wireless and Microwave Technology Conference (WAMICON)*, Cocoa Beach, FL, 2017, pp. 1-3.
- [91] D. Hawatmeh and T. Waller, "A S/C-band high Q resonator architecture for direct print additive manufacturing," *2017 IEEE 18th Wireless and Microwave Technology Conference (WAMICON)*, Cocoa Beach, FL, 2017, pp. 1-4.
- [92] D. Hawatmeh and T. Weller, "2.4 GHz Band Pass Filter Architecture for Direct Print Additive Manufacturing", accepted for publication in *IEEE MTT-S International Microwave Symposium (IMS2018)*, Philadelphia, PA, USA, June 10-15, 2018.
- [93] Chengying Du, Kaixue Ma, Ting Feng and Shouxian Mou, "A self-packaged bandpass filter with controllable transmission zeros using Substrate Integrated Suspended Lines," *2016 IEEE International Conference on Microwave and Millimeter Wave Technology (ICMMT)*, Beijing, 2016, pp. 317-319.
- [94] F. Parment, A. Ghiotto, T. P. Vuong, L. Carpentier and K. Wu, "Substrate integrated suspended line to air-filled SIW transition for high-performance millimeter-wave multilayer integration," *2017 IEEE MTT-S International Microwave Symposium (IMS)*, Honolulu, HI, 2017, pp. 719-722.
- [95] M. Li and K. Ma, "Design of a low phase-noise oscillator using cavity resonator in substrate integrated suspended line technology," *2017 IEEE Electrical Design of Advanced Packaging and Systems Symposium (EDAPS)*, Haining, 2017, pp. 1-3.

APPENDICES

Appendix A: Copyright Permissions

A.1 Permissions for Chapter 3



The screenshot shows the Copyright Clearance Center RightsLink interface. At the top left is the Copyright Clearance Center logo. To its right is the RightsLink logo. Further right are navigation buttons for Home, Create Account, Help, and an email icon. Below the logo is a blue box with the IEEE logo and the text: "Requesting permission to reuse content from an IEEE publication". To the right of this box, the following information is displayed: Title: Embedded 6-GHz 3-D Printed Half-Wave Dipole Antenna; Author: Derar Fayez Hawatmeh; Publication: IEEE Antennas and Wireless Propagation Letters; Publisher: IEEE; Date: 2017. Below this information is the text "Copyright © 2017, IEEE". To the right of the information is a LOGIN button and a text box that says: "If you're a copyright.com user, you can login to RightsLink using your copyright.com credentials. Already a RightsLink user or want to learn more?".

Thesis / Dissertation Reuse

The IEEE does not require individuals working on a thesis to obtain a formal reuse license, however, you may print out this statement to be used as a permission grant:

Requirements to be followed when using any portion (e.g., figure, graph, table, or textual material) of an IEEE copyrighted paper in a thesis:

- 1) In the case of textual material (e.g., using short quotes or referring to the work within these papers) users must give full credit to the original source (author, paper, publication) followed by the IEEE copyright line © 2011 IEEE.
- 2) In the case of illustrations or tabular material, we require that the copyright line © [Year of original publication] IEEE appear prominently with each reprinted figure and/or table.
- 3) If a substantial portion of the original paper is to be used, and if you are not the senior author, also obtain the senior author's approval.

Requirements to be followed when using an entire IEEE copyrighted paper in a thesis:

- 1) The following IEEE copyright/ credit notice should be placed prominently in the references: © [year of original publication] IEEE. Reprinted, with permission, from [author names, paper title, IEEE publication title, and month/year of publication]
- 2) Only the accepted version of an IEEE copyrighted paper can be used when posting the paper or your thesis on-line.
- 3) In placing the thesis on the author's university website, please display the following message in a prominent place on the website: In reference to IEEE copyrighted material which is used with permission in this thesis, the IEEE does not endorse any of [university/educational entity's name goes here]'s products or services. Internal or personal use of this material is permitted. If interested in reprinting/republishing IEEE copyrighted material for advertising or promotional purposes or for creating new collective works for resale or redistribution, please go to http://www.ieee.org/publications_standards/publications/rights/rights_link.html to learn how to obtain a License from RightsLink.

If applicable, University Microfilms and/or ProQuest Library, or the Archives of Canada may supply single copies of the dissertation.

BACK

CLOSE WINDOW

Copyright © 2018 Copyright Clearance Center, Inc. All Rights Reserved. [Privacy statement](#), [Terms and Conditions](#). Comments? We would like to hear from you. E-mail us at customercare@copyright.com



Title: A multi-material 3D printing approach for conformal microwave antennas

Conference Proceedings: Antenna Technology (iWAT), 2016 International Workshop on

Author: D. Hawatmeh

Publisher: IEEE

Date: Feb. 2016

Copyright © 2016, IEEE

LOGIN

If you're a [copyright.com user](#), you can login to RightsLink using your [copyright.com](#) credentials. Already a [RightsLink user](#) or want to [learn more?](#)

Thesis / Dissertation Reuse

The IEEE does not require individuals working on a thesis to obtain a formal reuse license, however, you may print out this statement to be used as a permission grant:

Requirements to be followed when using any portion (e.g., figure, graph, table, or textual material) of an IEEE copyrighted paper in a thesis:

- 1) In the case of textual material (e.g., using short quotes or referring to the work within these papers) users must give full credit to the original source (author, paper, publication) followed by the IEEE copyright line © 2011 IEEE.
- 2) In the case of illustrations or tabular material, we require that the copyright line © [Year of original publication] IEEE appear prominently with each reprinted figure and/or table.
- 3) If a substantial portion of the original paper is to be used, and if you are not the senior author, also obtain the senior author's approval.

Requirements to be followed when using an entire IEEE copyrighted paper in a thesis:

- 1) The following IEEE copyright/ credit notice should be placed prominently in the references: © [year of original publication] IEEE. Reprinted, with permission, from [author names, paper title, IEEE publication title, and month/year of publication]
- 2) Only the accepted version of an IEEE copyrighted paper can be used when posting the paper or your thesis on-line.
- 3) In placing the thesis on the author's university website, please display the following message in a prominent place on the website: In reference to IEEE copyrighted material which is used with permission in this thesis, the IEEE does not endorse any of [university/educational entity's name goes here]'s products or services. Internal or personal use of this material is permitted. If interested in reprinting/republishing IEEE copyrighted material for advertising or promotional purposes or for creating new collective works for resale or redistribution, please go to http://www.ieee.org/publications_standards/publications/rights/rights_link.html to learn how to obtain a License from RightsLink.

If applicable, University Microfilms and/or ProQuest Library, or the Archives of Canada may supply single copies of the dissertation.

BACK

CLOSE WINDOW



Title: Embedded 6 GHz 3D-printed half-wave dipole antenna array
Conference Proceedings: Wireless and Microwave Technology Conference (WAMICON), 2017 IEEE 18th
Author: Derar Hawatmeh
Publisher: IEEE
Date: April 2017
Copyright © 2017, IEEE

LOGIN
If you're a [copyright.com](#) user, you can login to RightsLink using your [copyright.com](#) credentials. Already a [RightsLink](#) user or want to [learn more?](#)

Thesis / Dissertation Reuse

The IEEE does not require individuals working on a thesis to obtain a formal reuse license, however, you may print out this statement to be used as a permission grant:

Requirements to be followed when using any portion (e.g., figure, graph, table, or textual material) of an IEEE copyrighted paper in a thesis:

- 1) In the case of textual material (e.g., using short quotes or referring to the work within these papers) users must give full credit to the original source (author, paper, publication) followed by the IEEE copyright line © 2011 IEEE.
- 2) In the case of illustrations or tabular material, we require that the copyright line © [Year of original publication] IEEE appear prominently with each reprinted figure and/or table.
- 3) If a substantial portion of the original paper is to be used, and if you are not the senior author, also obtain the senior author's approval.

Requirements to be followed when using an entire IEEE copyrighted paper in a thesis:

- 1) The following IEEE copyright/ credit notice should be placed prominently in the references: © [year of original publication] IEEE. Reprinted, with permission, from [author names, paper title, IEEE publication title, and month/year of publication]
- 2) Only the accepted version of an IEEE copyrighted paper can be used when posting the paper or your thesis on-line.
- 3) In placing the thesis on the author's university website, please display the following message in a prominent place on the website: In reference to IEEE copyrighted material which is used with permission in this thesis, the IEEE does not endorse any of [university/educational entity's name goes here]'s products or services. Internal or personal use of this material is permitted. If interested in reprinting/republishing IEEE copyrighted material for advertising or promotional purposes or for creating new collective works for resale or redistribution, please go to http://www.ieee.org/publications_standards/publications/rights/rights_link.html to learn how to obtain a License from RightsLink.

If applicable, University Microfilms and/or ProQuest Library, or the Archives of Canada may supply single copies of the dissertation.

[BACK](#)[CLOSE WINDOW](#)

A.2 Permissions for Chapter 4



RightsLink®

Home

Create Account

Help



Title: A S/C-band high Q resonator architecture for direct print additive manufacturing
Conference Proceedings: Wireless and Microwave Technology Conference (WAMICON), 2017 IEEE 18th
Author: Derar Hawatmeh
Publisher: IEEE
Date: April 2017
Copyright © 2017, IEEE

LOGIN
If you're a copyright.com user, you can login to RightsLink using your copyright.com credentials. Already a RightsLink user or want to [learn more?](#)

Thesis / Dissertation Reuse

The IEEE does not require individuals working on a thesis to obtain a formal reuse license, however, you may print out this statement to be used as a permission grant:

Requirements to be followed when using any portion (e.g., figure, graph, table, or textual material) of an IEEE copyrighted paper in a thesis:

- 1) In the case of textual material (e.g., using short quotes or referring to the work within these papers) users must give full credit to the original source (author, paper, publication) followed by the IEEE copyright line © 2011 IEEE.
- 2) In the case of illustrations or tabular material, we require that the copyright line © [Year of original publication] IEEE appear prominently with each reprinted figure and/or table.
- 3) If a substantial portion of the original paper is to be used, and if you are not the senior author, also obtain the senior author's approval.

Requirements to be followed when using an entire IEEE copyrighted paper in a thesis:

- 1) The following IEEE copyright/ credit notice should be placed prominently in the references: © [year of original publication] IEEE. Reprinted, with permission, from [author names, paper title, IEEE publication title, and month/year of publication]
- 2) Only the accepted version of an IEEE copyrighted paper can be used when posting the paper or your thesis on-line.
- 3) In placing the thesis on the author's university website, please display the following message in a prominent place on the website: In reference to IEEE copyrighted material which is used with permission in this thesis, the IEEE does not endorse any of [university/educational entity's name goes here]'s products or services. Internal or personal use of this material is permitted. If interested in reprinting/republishing IEEE copyrighted material for advertising or promotional purposes or for creating new collective works for resale or redistribution, please go to http://www.ieee.org/publications_standards/publications/rights/rights_link.html to learn how to obtain a License from RightsLink.

If applicable, University Microfilms and/or ProQuest Library, or the Archives of Canada may supply single copies of the dissertation.

BACK

CLOSE WINDOW

Copyright © 2018 Copyright Clearance Center, Inc. All Rights Reserved. [Privacy statement](#). [Terms and Conditions](#). Comments? We would like to hear from you. E-mail us at customercare@copyright.com



Title: High- Q Tunable Microwave Cavity Resonators and Filters Using SOI-Based RF MEMS Tuners

Author: Xiaoguang Liu

Publication: Microelectromechanical Systems, IEEE/ASME Journal of

Publisher: IEEE

Date: Aug. 2010

Copyright © 2010, IEEE

LOGIN

If you're a [copyright.com](#) user, you can login to RightsLink using your [copyright.com](#) credentials. Already a RightsLink user or want to [learn more?](#)

Thesis / Dissertation Reuse

The IEEE does not require individuals working on a thesis to obtain a formal reuse license, however, you may print out this statement to be used as a permission grant:

Requirements to be followed when using any portion (e.g., figure, graph, table, or textual material) of an IEEE copyrighted paper in a thesis:

- 1) In the case of textual material (e.g., using short quotes or referring to the work within these papers) users must give full credit to the original source (author, paper, publication) followed by the IEEE copyright line © 2011 IEEE.
- 2) In the case of illustrations or tabular material, we require that the copyright line © [Year of original publication] IEEE appear prominently with each reprinted figure and/or table.
- 3) If a substantial portion of the original paper is to be used, and if you are not the senior author, also obtain the senior author's approval.

Requirements to be followed when using an entire IEEE copyrighted paper in a thesis:

- 1) The following IEEE copyright/ credit notice should be placed prominently in the references: © [year of original publication] IEEE. Reprinted, with permission, from [author names, paper title, IEEE publication title, and month/year of publication]
- 2) Only the accepted version of an IEEE copyrighted paper can be used when posting the paper or your thesis on-line.
- 3) In placing the thesis on the author's university website, please display the following message in a prominent place on the website: In reference to IEEE copyrighted material which is used with permission in this thesis, the IEEE does not endorse any of [university/educational entity's name goes here]'s products or services. Internal or personal use of this material is permitted. If interested in reprinting/republishing IEEE copyrighted material for advertising or promotional purposes or for creating new collective works for resale or redistribution, please go to http://www.ieee.org/publications_standards/publications/rights/rights_link.html to learn how to obtain a License from RightsLink.

If applicable, University Microfilms and/or ProQuest Library, or the Archives of Canada may supply single copies of the dissertation.

BACK**CLOSE WINDOW**

Appendix B: nScript Tabletop 3Dn Printer



Figure B.1: nScript Tabletop 3Dn printer.

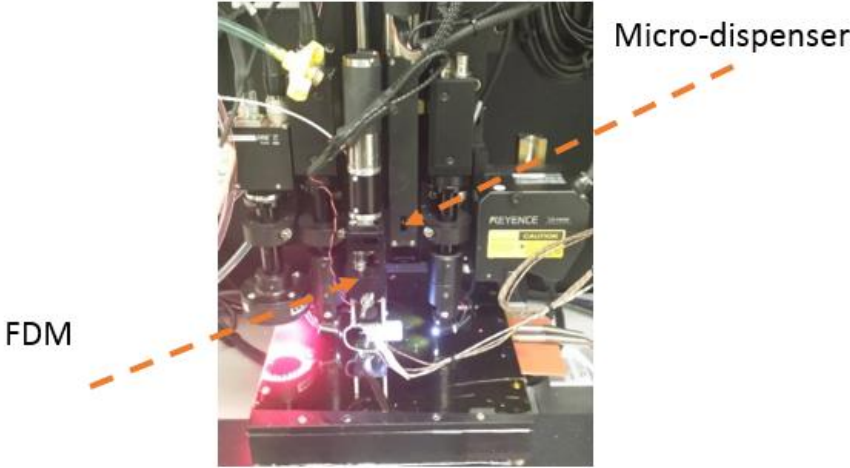


Figure B.2: FDM and micro-dispenser heads.

ABOUT THE AUTHOR

Derar F. Hawatmeh received a B.Sc. degree in communications and electronics engineering from the Jordan University of Science and Technology (JUST), Irbid, Jordan, in 2010. In 2010, he joined the master program of the Electrical Engineering Department, JUST, majoring in Wireless Communications. From 2012 to 2013, he was a researcher with the research and development department, Waseela-Integrated Telecommunication Solutions. He was an Instructor with the Network and Communications Engineering Department, Al Ain University of Science and Technology, Al Ain, United Arab Emirates, from 2013 to 2014. In 2014, he joined the Center for Wireless and Microwave Information Systems, University of South Florida, Tampa, FL, USA, as a Graduate Research Assistant. During his PhD program, Derar joined QORVO, a leading semiconductor company, for two summer internships as systems engineering intern and bulk acoustic filter (BAW) design intern. His current research interests include the analysis and design of real time localization systems (RTLs), and the analysis and the design of planar antennas, 3-D antennas compact, planar, passive, and multi-frequency and ultra-wideband microwave components for wireless applications. He has published and to be published 14 journal and conference papers from his masters and PhD programs.

Hawatmeh was selected as one of the 2015 USF College of Engineering research week poster award honorable mention recipients, selected to the student's paper competition finalist in the international workshop of antenna technology (IWAT) 2016, and received the best student paper award of the IEEE wireless and microwave technology conference (WAMICON) 2017.